MASTER THESIS

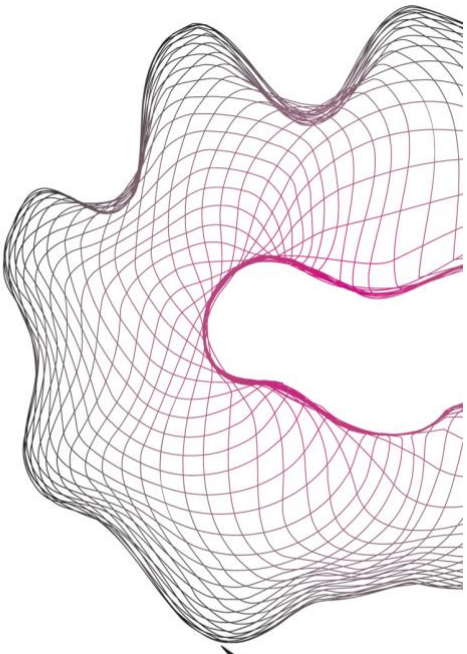

BIOENGINEERED 3D MULTICELLULAR HEPATIC MODEL TO STUDY THE MECHANOBIOLOGICAL INDUCTION AND PROGRESSION OF LIVER TISSUE FIBROTIC STAGES

Marta Sacchi

FACULTY OF ENGINEERING TECHNOLOGY
DEPARTMENT OF BIOMECHANICAL ENGINEERING

EXAMINATION COMMITTEE
Dr. Ir. Jeroen Rouwkema
Dr. Ruchi Bansal
MSc. Fabian Stein

DOCUMENT NUMBER
BE - 793

UNIVERSITY OF TWENTE.

25-05-2021

Acknowledgements

I would like to thank Fabian Stein for his supervision during this thesis and for giving me the possibility to expand my knowledge in such a multidisciplinary project. Thank you for all the support and the time you have dedicated to answer my thousand questions. Thank you for having shaped and improved my scientific skills and thinking. And, mostly, thank you for having taught me that, sometimes, in science – as in life – a big laugh is the best way to approach and overcome even the toughest obstacles.

I would also like to thank prof. Jeroen Rouwkema and prof. Ruchi Bansal for having given me the opportunity to work on such a challenging and stimulating project. Thank you for all the scientific feedbacks and for your professional support during these years.

I would also want to thank Deepti Rana and Ajoy Kandar for their help during GelMA synthesis and rheology. Thank you also Eline Geervliet for having helped me with ELISA and qPCR analysis. Thank you all.

I would also want to thank Dr. Yu Suk Choi and all the amazing people at the Stem Cell Mechanobiology Lab at the University of Western Australia in Perth. Thank you for having given me the opportunity to spend my internship in such an amazing and stimulating environment and thank you for your continuous support.

I would like to express my most sincere gratitude to my family, to my mother and father, for their unconditional support despite the distance. Without you this would have not been possible. Thanks to all my university friends for all the memorable adventures during these years, thanks for being my great second family. Thanks for all the laughs and memorable dinners together. A big thanks also to my old friends, for having supported me throughout all these years. I have never felt lonely. Finally, I would like to thank Mattia for all his immense support since the first time I set a foot in Enschede. This thesis is also yours.

Thank you all.

Abbreviations

ASCs	Adult stem cells
α-SMA	Alpha-smooth muscle actin
AB	Antibody
BFP	Blue fluorescent protein
CCL2	C-C motif ligand 2
CXCL	C-X-C motif chemokine ligand
CD	Cluster of differentiation
Col I	Collagen type I
Col III	Collagen type III
EGM-2	Endothelial Cell Basal Medium 2
ECs	Endothelial cells
EGF	Epidermal growth factor
ECM	Extracellular matrix
FFA	Free fatty acids
GelMA	Gelatin metacrhyloyl
GMO	Genetically modified organism
GAPDH	Glyceraldehyde-3-phosphate
GFP	Green fluorescent protein
HSCs	Hepatic stellate cells
HBV	Hepatitis B virus
HPs	Hepatocytes
HG-DMEM	High glucose, without glutamine Dulbecco's Modified Eagle Medium
NASH	Human non-alcoholic steatohepatitis
HUVEC	Human umbilical vein endothelial cells
IF	Immunofluorescence
iPSCs	Induced pluripotent stem cells
IL-6	Interleukin 6
IL-8	Interleukin 8
KCs	Kupffer cells
LPS	Lipopolysaccharide

LLOC	Liver lobule on-a-chip
LSECs	Liver sinusoidal endothelial cells
MMPs	Matrix metalloproteinases
MSCs	Mesenchymal stem cells
MA	Methacrylic anhydride
MTX	Methotrexate
MFs	Myofibroblasts
NO	Nitric Oxide
NPCs	Non parenchymal cells
NAFLD	Non-alcoholic fatty liver disease
NMR	Nuclear magnetic resonance spectroscopy
PCs	Parenchymal cells
PMA	Phorbol-12-myrisstate-13-acetate
PIs	Photo initiators
PDGFβ	Platelet-derived growth factor subunit β
PDMS	Polydimethylsiloxane
PET	Polyethylene terephthalate
PVC	Polyvinyl chloride
PPHs	Primary human hepatocytes
ELISA	Protein secretion by enzyme-linked immunosorbent assay
qPCR	Quantitative polymerase chain reaction
RFP	Red fluorescent protein
RPMI	Roswell Park Memorial Institute
Ru	Ruthenium
SEM	Scanning Electron Microscopy
SPS	Sodium persulfate
SD	Standard deviation
SEM	Standard error of the mean
SCs	Stellate cells
TGF-β	Transforming growth factor beta
TMSPMA	3-(Trimethoxysilyl) propyl methacrylate

TNF- α	Tumor necrosis factor α
TCR-T	Tumor specific T cell receptors
VEGF	Vascular endothelial growth factor
vWR	Von Willebrand factor
WSS	Wall shear stress

Table of content

1. Abstract

Fibrosis, characterized by an aberrant accumulation of extracellular matrix (ECM) leading to scar tissue and impaired organ function, is a significant health condition impacting millions of people worldwide and accounting for about 45% of total deaths. The constant increase of metabolic disorders and chronic medical conditions (such as diabetes and obesity) in the world aging population will significantly impact on the incidence of fibrotic diseases and subsequently on the number of fibrosis-related deaths. Fibrosis is a common outcome of many chronic diseases, involving different organs, including liver. Currently, there are no therapies available to reverse chronic fibrosis and organ transplantation is the only option available. However, this option is limited due to organ shortage and chronic rejection and it is only possible when diagnosed in a very early stage. The persistence of this unmet clinical need is due to the complexity of the disease process that involves numerous cell types and signaling pathways. Lack of reliable, reproducible, easy-to-handle quantitative *in vitro* models recapitulating the biological mechanisms underpinning tissue fibrosis pathophysiology, partially, hampered the testing and development of clinically relevant anti-fibrotic drugs.
In this context, several combined 3D fibrotic liver tissue models have been developed by integrating physiological-relevant hepatic 3D co-culture models with microfluidic platforms. Surprisingly, the main focus of such models verted to the establishment of a relevant liver tissue models for the study of drug metabolism and for toxicity screening upon pro-fibrotic induction by soluble chemicals. Not much attention has been directed towards the development of complex bioengineered 3D liver models aimed at recapitulating the key mechanobiological aspects underlying tissue fibrosis development and functioning, by providing key *in vivo* ECM mechanical features and hepatic multicellular 3D culture models, independently on exogenous pro-fibrotic chemical factors induction.

In such a context, in this project, we hypothesized that the resemble of key tissue mechanical properties (stiffness, interstitial flow, hydrostatic pressure) over typical pathophysiological ranges of value could promote cell differentiation into pro-fibrotic phenotype *via* the activation of latent pro-fibrogenic growth factors generating a pro-fibrotic cascade of event, thus leading, and perpetuating a fibrotic microenvironment. In order to prove that, a physiological-relevant *in vitro* 3D model to study the effects of the mechanical properties of the matrix on liver tissue fibrosis development and functioning was developed, by *i*) establishing a liver microtissue model in form of a multicellular hepatic spheroid model; *ii)* providing it with a physio-pathological relevant tissue microenvironment mimicking key mechanical and biological feature.

2. Introduction

2.1. Liver function and structure

The liver is one of the biggest, most complex, and versatile organs of the human body playing a fundamental role in many pivotal vital functions and organism homeostasis. Due to its anatomical position, the liver is closely connected with the digestive system, contributing to the synthesis and absorption of nutrients, detoxification of xenobiotic compounds and regulation of the immune response [1, 2]. It is responsible for the intermediary metabolism of lipids, amino acids, proteins and carbohydrates, for the production and processing of hormones and serum protein (*i.e.*, albumin, globulins, prothrombin, fibrinogen), for the storage of vitamins and for the regulation of plasma glucose [2, 3]. It is also responsible for the excretion of bilirubin and conversion of ammonia, a toxic by-product of protein metabolism, into urea, which is subsequently excreted in the urine [2]. The liver is also able to regenerate itself after chemical injury and partial hepatectomy and can restore its original mass, cellular structure and function [4].

The liver receives a dual bloody supply system from the portal veins and the hepatic arteries. The portal vein carries partially deoxygenated and nutrient-rich blood from the surrounding organs (small intestine, stomach, pancreas) and it is responsible of about 75% of the total blood supply in the liver. The hepatic artery, instead, supplies oxygenated blood from the heart and it is responsible of about 25% of liver's total blood supply [5]. Together with the bile duct, the branches of the portal vein and hepatic artery form the lobules, the functional units of liver [3]. The Liver is constituted of approximately 100,000 hexagonal- shape lobules, each one consisting of a central vein surrounded by six portal veins at each of the six corners. Each portal vein is combined with a hepatic artery and a bile duct, forming a sub-unit called portal triad. Additionally, a series of capillaries-like veins, called sinusoids, run between lobule cords to meet in the central vein [6, 7].
The liver lobule is composed of different cell types (**Table 1**) that can be classified as parenchymal cells (PCs), hepatocytes, that are organized into cord-like structures by non-parenchymal cells (NPCs) (liver endothelial cells, hepatic stellate cells and Kupffer cells) [8].

Hepatocytes (HPs) are the biggest and most abundant cells in the liver lobule (60-70% of cell ratio and 80% of the liver mass) [8]. They can be considered as the building blocks this organ. These cells are polygonal, could be binucleated, with a diameter of 20-30 µm [9]. Hepatocytes are functionally and structurally polarized, characterized by three membrane functional domains: i) basal (or sinusoidal) domain, presenting short microvilli, involved in the blood exchange with the sinusoidal blood; ii) lateral domain, which forms junctional complexes between adjacent hepatocytes; and iii) apical (or canalicular) domain [8]. Physiologically, these apicobasal polarization results in a complex of spatially adjacent hepatocytes, closely arranged in cords to form liver plates that allows substances to enter from the blood for excretion with bile. Hepatocytes are cells characterized by a high metabolism, responsible for the major liver functions including synthesis, metabolism and detoxification (e.g., urea, albumin, glutamine, bile acid, cholesterol and lipid biosynthesis) [3].

The non-parenchymal cells, composing the remaining 30 - 40 % of the cell population, play a key role in mediating the tissue response to metabolic and toxic stimuli, as well as in supporting hepatocytes functions and tissue architecture [9]. The hepatocytes – NPCs interplay, mainly mediated by a mixture of cytokines and growth factors, is crucial for triggering immune responses, regeneration and tissue homeostasis [8].

Liver sinusoidal endothelial cells (LSEC) are the most abundant NPCs in the liver and account for the 16% of the total cell proportion [9]. With a diameter of 6.5-11 μm, they are highly specialized endothelial cells (ECs) without basement membrane that lay next to each other, creating a barrier with intracellular fenestration pores of 150-175 nm of diameter. This particular organization regulates the transfer of soluble molecules between the blood and the space of Dissie, a cavity between blood and the underlying hepatocytes [10]. Furthermore, LSEC play also a key role in the local immune response: they could trigger inflammatory pathways by expressing different adhesion molecules, recruiting and providing adhesion to immune cells [11]. Furthermore, LSEC are responsible to shear stress and release vasodilator agents, which modulate endothelial regulators, such as nitric oxide, a key modulator of the vascular tone [12].

Hepatic stellate cells (HSCs) represent 8% of the total hepatic cell proportion. Located in the space of Dissie, HSCs are fibroblast-like cells with a diameter of 10-11 μm [9]. Under healthy physiological conditions, HSCs show quiescent-like phenotype and are mainly responsible for the storage of vitamin A and lipid and the control of ECM turnover [13, 14]. Their location in the space of Dissie, surrounding sinusoids, allows them to act as pericytes, controlling sinusoid diameter and blood flow. Furthermore, they also function as an antigen-presenting cell, responding and influencing immune cells. Upon chronic inflammation or regeneration processes, HSCs transdifferentiate into myofibroblast-phenotype, identified by alpha-smooth muscle actin (α-SMA) marker expression, acting as fibrogenic, proliferating cells and secreting cytokines, chemokines and ECM components, such as collagen I and III [15]. They are considered as pathological key players during chronic liver injuries, as they deposit new ECM, increasing liver stiffness. In addition to that, HSCs are also responsible for matrix metalloproteinases (MMPs) and their inhibitors production, emphasizing the ability to remodel their microenvironment dynamically [16]. Upon inflammation resolution, HSCs undergo apoptosis and senescence in order to re-establish the healthy physiological condition [17].

Kupffer cells (KCs) are resident liver macrophages, accounting for approximately 15% of the entire liver cell population and with a diameter of 10-13 μm [9]. They are mainly localized in the lumen of hepatic sinusoids, anchored to the surface of LSEC, directly exposed to the blood flow. They play a crucial role in maintaining the homeostasis of the liver environment, removing genotoxic compounds from the portal vein, maintaining immunological tolerance and secreting anti-inflammatory factors [18]. Upon inflammatory conditions, KCs become activated, secreting pro-inflammatory chemokines, cytokines and proteolytic enzymes. In particular, tumor necrosis factor α (TNF- α) and interleukin 6 (IL-6) secretion, activated in response to inflammation, can both contribute to regeneration or apoptosis (depending on the activity of other signal transduction pathways), inducing liver infiltration of other immune cells, such as T cells, neutrophil and natural killer cells or ECM deposition from other liver cell types [19, 20].

Table 1. *Main liver cell types, ratio, and functions. Adapted from [8].*

Cell	Type	Diameter (μm)	Proportion (number)	Features
Parenchymal	-	-	-	-
Hepatocytes	Epithelial	20-30	60%-65%	Large in size, abundant in glycogen, mostly double nuclei
Non-parenchymal	-	-	-	-
Kupffer cells	Macrophages	10-13	15%	Irregularly shaped, mobile cells, secretion of mediators
Liver sinusoids endothelial cells	Epithelial	6.5-11	16%	SE-1, CD31, fenestration, none basement membrane
Hepatic stellate cells	Fibroblasts	10.7-11.5	8%	Vitamin-storing, distinct basement membrane

2.2. Liver fibrosis

In general terms fibrosis is a wound healing process triggered by chronic tissue injury followed by chronic inflammation and ECM deposition, ultimately resulting in organ failure [21] (**Figure 1**). Chronic epithelial cells injury, upon pro-inflammatory factor release, instigates the recruitment and activation of immune cells (mostly macrophages) in the injured tissue, which, in turn, release pro-fibrotic factors, such as cytokines, chemokines and growth factors [6, 21, 22]. These cascades of biochemical stimuli cause the trans-differentiation of quiescent fibroblasts into activated myofibroblasts (MFs), which, in turn, secrete a vast amount of ECM components, mainly collagens (especially type I and III) resulting in tissue scarring and fibrosis [23]. Among all, the main growth factor causing fibroblasts trans-differentiation is the transforming growth factor beta (TGF-β). This accumulation of excessive ECM replaces the hepatocytes, causing the loss of liver regenerative capacity [24]. However, tissue fibrosis is a complex and multifactorial disease, that evolves from a concerted interaction between different cell types with disparate tissue microenvironmental signals [25-27]. As such, while tremendous research has been focused on biochemical cues underlying MFs transdifferentiation and functioning, the investigation over the importance of the multicellular crosstalk (with particular regard to immune and endothelial cells), and, most importantly, of other fibrogenic factors such as hypoxia, matrix stiffness, mechanical tension/shear stress, vascular and interstitial flow has not been deeply investigated yet [28].

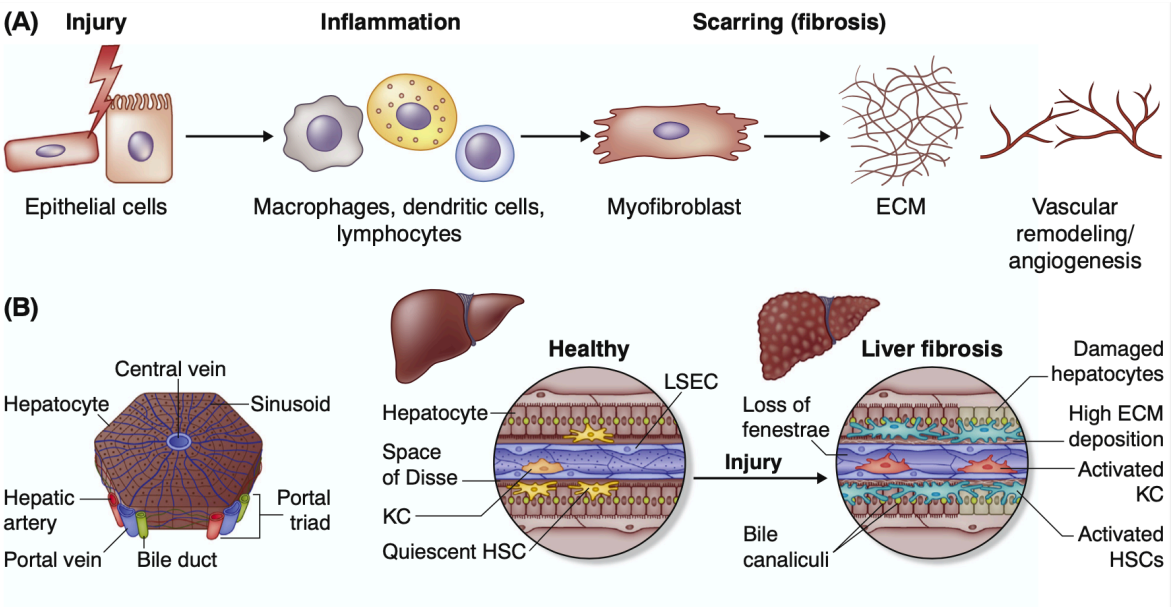

Figure 1. (A) *Schematic representation of fibrosis pathogenetic cascade of events. Epithelial cell injury triggers inflammation and immune cells infiltration, which, in turn, secrete specific soluble factors (cytokines, growth factors) leading to fibroblasts activation and transdifferentiation into myofibroblasts. Subsequently, myofibroblasts secreted ECM components, leading to matrix remodeling and vascular remodeling and angiogenesis.* ***(B)*** *Schematic diagram of liver lobule and its structural changes during tissue fibrosis. Adapted from [29].*

2.2.1. **Biomechanical induction**

Mechanical stimuli from cellular microenvironment play a key role in affecting cell behavior and differentiation similarly to chemical signals and are likely to be equally important in the generation and progression of tissue fibrosis [30]. These forces in tissue derive from a multifactorial interplay of causes, such as: *i*) cell-generated tension; ii) increase in hydrostatic and osmotic pressure; iii) alteration in fluid flow. Collectively, these phenomena regulate the phenotype and proliferation of MFs and other cells in damaged tissues, the activation of growth factors as well as and the structure and mechanics of the ECM, promoting tissue fibrosis [21, 31].

In this context, it is important to note that changes in the mechanical properties of the tissues can cause fibrosis, as well as result from it. In the same way as a profibrogenic growth factor (i.e., TGF-β) both stimulates MFs activation and is then produced by the same, perpetuating fibrosis, MFs can be activated in response to mechanical stimuli and then perpetuate fibrosis by altering the mechanical environment [32]. Concurrent with this, mechanical and chemical signals are often directly and indirectly interdependent in a free-forward loop: the MFs environment alteration, causes the reorganization of environment itself, which, in turn, affects cellular behavior in response to profibrogenic biochemical and mechanical stimuli [33]. Notably, increased TGF-β level results in increased α-SMA, which interacts with cellular myosin to contract and produce increased tension on the surrounding matrix, thereby perpetuating fibrosis [34, 35].

In this context, the matrix plays a fundamental role in the mechanobiological mechanisms underlying injured and fibrotic tissues. Increased deposition of the fibrillar collagens (especially I and III) is a typical hallmark of tissue fibrosis and it is responsible for increasing stiffness to tissues [36, 37]. Given their dense interconnections and rigid and rod-like shape, under certain forces, they can influence cell migration, angiogenesis and exposure of cells to fluid flow, and can permit long-distance transmission of forces [38, 39]. Besides that, it has been proven that the mechanical properties of the injured liver

change significantly early after injury - before significant matrix deposition occur – as result of collagen and elastin cross-linking, leading to a significant increase in tissue elastic modulus [36].
Furthermore, altered fluid flow, including vascular flow and interstitial fluid flow, results in changes in growth factor release, collagen alignment, and MFs differentiation, and may be both the cause and the result of tissue remodeling and fibrosis [40]. Specifically, alterations in vessel geometry, flow rate, and fluid viscosity contribute to changes in shear-stress, regulating the release by endothelial cells of growth factors, vasodilators, and others, leading to long-term changes in gene and protein expression [41]. These fluid flow alterations may also result in pathologic angiogenesis. Angiogenesis and fibrosis often progress in parallel and may positively regulate each other [42]. Extensive research has shown that stiffness regulates the dynamics of tube formation and protostomes orientation [43, 44] and more specifically the transcriptional pathways that control angiogenesis [45].

2.3. Liver models for disease modeling and drug development

Owing to the disease complexity, development of therapies has been challenging contributing to the lack of anti-fibrotic therapies for clinical application. Further, therapies proven to be potentially effective in animal fibrosis models were failed in the clinical trials suggesting disparity between animal models and human. This led to the development of human disease mimic *in vitro* models for recapitulating multi-phenomena tissue fibrosis. These platforms not only proved to be versatile tools for disease modeling but also promising aids in drug discovery and testing of new therapeutic targets in clinically relevant disease models.

However, given the structural and physiological complexity of the liver lobule, modeling liver tissue fibrosis remains challenging, and currently there is not an *in vitro* model of the liver lobule that can exhaustively recapitulate the full organ [6]. Despite this, there exist a vast range of design possibilities, varying from simple and scalable platforms for understanding the fundamentals of disease mechanisms to more complex, physiological-like platforms, harder to replicate and control (**Figure 2**) [29]. The incorporation of complexity, while on one side would increase the physiological relevance of the model (e.g., by incorporating immune cells or a vascular network), on the other side would require a more in-depth characterization of the system together with a more difficult control over the multiple variables that come into play. In such context, it is crucial to clearly define the specific research question and application of the desired model and then to base on that the minimum level of complexity required for that specific purpose.

2.3.1. **2D models**

2D *in vitro* models of liver fibrosis are widely used as simple and reliable platforms for understanding the fundamental underlying disease mechanism and for high-throughput screening of pro- and antifibrotic compounds. Primary fibroblasts upon TGF-β treatment or tunable stiffness surfaces, have been observed to transdifferentiate into a highly proliferative, contractile and ECM-producing MFs [33, 46, 47]. Similarly, simple co-culture monolayers have demonstrated the fundamental juxtracrine and paracrine signaling underpinning cellular phenotype differentiation [48]. However, numerous comparisons of gene expression profiles have demonstrated that 2D culture- activated HSCs do not recapitulate the in vivo activated HSCs [33].

Therefore, although these platforms provide several advantages, such as ease of handling, multiplexing, high reproducibility, single-cell profiling under different culture condition, enabling the identification of several fibrotic cellular markers, they lack the complexity of the 3D physio-pathological tissue environment, and, above all, the cell-ECM interaction and the tissue biomechanics, leading to physiological irrelevant cellular behavior.

2.3.2. **3D models**

Similar to *in vivo* conditions, 3D models enable cell-cell and cell-matrix interaction, cellular migration, chemiotaxis, traction, and integrin adhesions, in all three planes, and replicate soluble growth factor gradient and supporting cellular differentiation and maturation. The simplest 3D models are based on the cellular self-assembly and can be mainly classified into spheroids or organoids. Spheroids represent the lowest level of complexity and are generally made of adult tissue cells or stem cell population [49]. Organoids consist of organ-specific cell types developed from stem cells or organ progenitor cells that generally tend to follow the physiological tissue development and organization found *in vivo* [50, 51]. These cellular aggregates therefore are able to recapitulate numerous hepatic biological phenomena, including spatial cellular organization, cell – matrix interaction, and liver tissue-specific physiological functions by integrating in a single platform key hepatic parenchymal and non-parenchymal cells [52]. Altogether, these aspects proved to provide reliable platform for modelling patho-physiological hepatic cellular response to pro-fibrotic compounds, drugs, personalized medicine and gene therapy. However, their actual application is limited as they lack mechanical cues as well as perfused vasculature, and their intrinsic heterogeneity and size variation limit their adaptability for high throughput screenings.

2.3.3. **Bioengineered 3D models**

A more engineering-driven approach to create tissue complexity is by using physiologically relevant biomaterial scaffolds (synthetic or biological) and bio-fabrication techniques (3D bioprinting, bioreactors or microfluidics platforms). These techniques, alone or in combination, can be exploited to develop constructs that, in combination with 3D cell cultures, can better resemble *in vitro* the functional and mechanical properties of physiological tissues, by providing structural integrity as well as tissue-specific microenvironment. The use of microfluidic devices, especially, offers great potential in recapitulating the *in vivo* liver dynamic microenvironment including hydrodynamic and mechanical cues (e.g., (interstitial) fluid flow, shear stress, mechanical strain, hydrostatic pressures), biochemical cues (e.g., concentrations and gradients of soluble factors), oxygen and nutrient supply and removal of metabolic waste, and parallelization and multiplexing with other 3D systems, which can potentially allow high-throughputs [53, 54].

2.3.3.1. Vascularized models

Along with that, the formation of an organized and endothelialized vascular network within a bioengineered model is crucial for providing a physiological environment and selective barrier controlling the molecular transport between the vessels and the surrounding tissues, as well as for enhancing cell and tissue maturation and organization inside the system.

Blood vessels allow the efficient transport of oxygen, nutrients, and signaling factors to cells, as well as cellular crosstalk between the vascular network and other cells occurring during development and

wound healing [55]. Tissue-specific endothelium is often unique for each organ and directs angiocrine repair and maintenance functions.
However, the integration of such vascular network in an *in vitro* model introduces a further considerable level of complexity and several limitations remain to be solved, such as the vasculature-cell maturation and the limited perfusability of such networks.

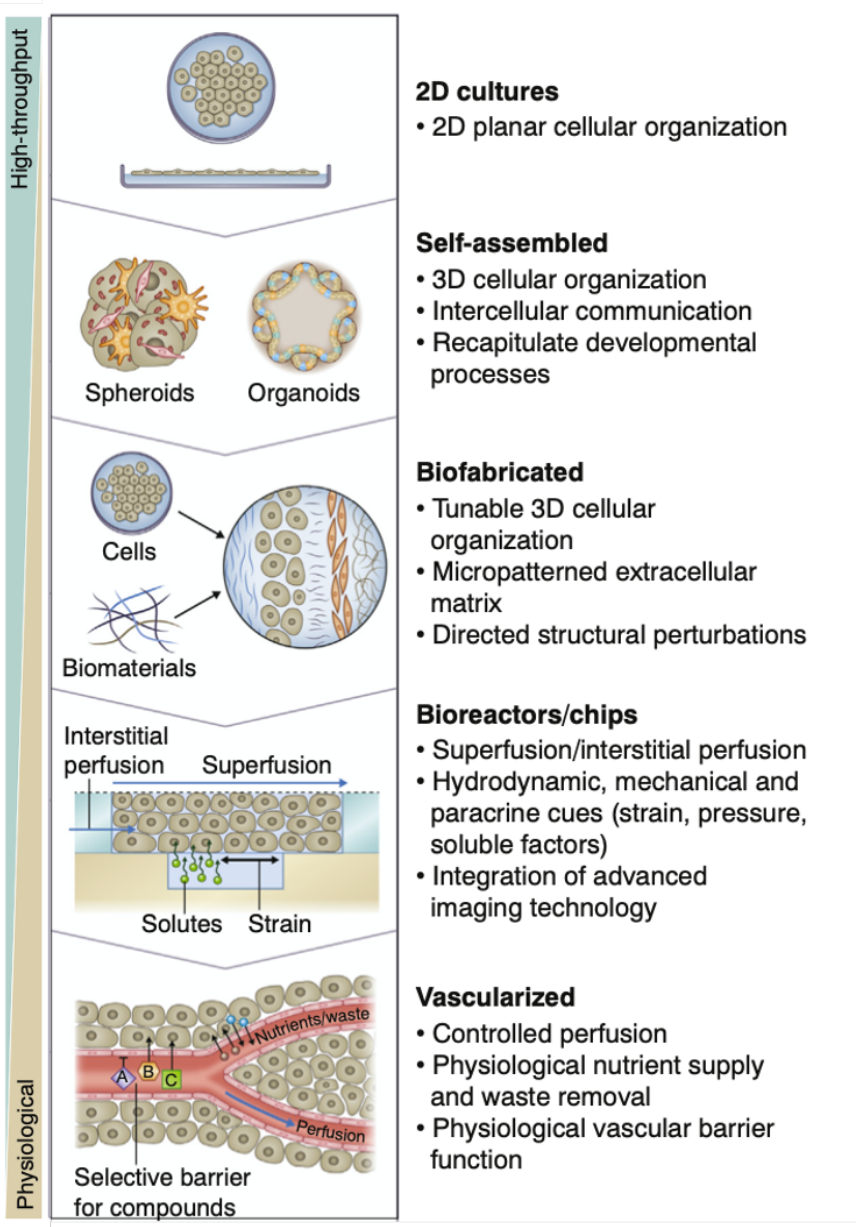

Figure 2. *General classification of conventional in vitro tissue models for recapitulating tissue diseases pathogenesis and development, with regard to physiological complexity and high-throughput screening. Adapted from [29].*

2.4. Modelling of 3D engineered liver lobule fibrosis: state-of-the-art

A combined synergetic strategy aimed at integrating multicellular 3D model and (vascularized) engineered tissue microenvironment might provide highly physiological-relevant models, overcoming the project limitation that comes with these single techniques.

In this context, several combined 3D fibrotic liver tissue models have been developed by integrating physiological-relevant hepatic 3D co-culture models with microfluidic platforms (**Table 2, Figure 3**). Surprisingly, the main focus of such models verted to the establishment of a relevant liver tissue models for the study of drug metabolism and for toxicity screening upon pro-fibrotic induction by soluble chemicals. To our best knowledge, not much attention has been directed towards the development of complex bioengineered 3D liver models aimed at recapitulating the key mechanobiological aspects underlying tissue fibrosis development and functioning, by providing key *in vivo* ECM mechanical features and hepatic multicellular 3D culture models, independent on exogenous pro-fibrotic chemical factors induction.

***Table 2**. Relevant models of 3D in vitro engineered liver fibrosis. Primary human hepatocytes (PPHs), human umbilical vein endothelial cells (HUVEC), stellate cells (SCs), polyethylene terephthalate (PET), human non-alcoholic steatohepatitis (NASH), non-alcoholic fatty liver disease (NAFLD), lipopolysaccharide (LPS), epidermal growth factor (EGF), free fatty acids (FFA), hepatitis B virus (HBV).*

Design of microphysiological device	Purpose	Pro-fibrotic induction (and treatment)	Ref
Perusable gelatin hydrogel embedding co-culture mouse HCs, ECs, SCs spheroids	Modelling inflammatory early and late NASH fibrosis stages and antifibrotic drug screening	• Palmitic acid and TGF-β treatment for 6 days • Ezetimibe treatment for disease resolution	[56]
Sandwich-like chip, divided into a parenchymal channel (PHHs) and NP channel (LSECs, KFs, HSCs), separated by a porous ECM collagen I layer	Modelling liver injury and steatosis development and progression	• Methotrexate (MTX) daily treatment for 7 days	[57]
Sandwich-like chip, divided into a hepatic chamber (PHHs) and a vascular channel (LSECs, KCs, HSCs), separated by a porous PET membrane	Modelling the inflammation response, as well as hepatotoxicity and liver damage	• LPS, EGF and TGF-β daily treatment for 14 days	[58]
Array of interconnected honeycumb structures containing co-culture hepatic spheroids (PHHs, KCs, HSCs, HUVEC) and microvasculature	Modelling of NAFLD-induced hepatic fibrosis development, progression and potential resolution	• TGF-β or FFA supplemented medium for 14 days • Pirfenidone treatment for 7 days to study the resolution	[59, 60]
GelMA hydrogels static platforms containing co-	Modelling of NAFLD-induced	• TGF-β or FFA supplemented medium for 14 days	[61]

culture hepatic spheroids (PHHs, KCs, HSCs, HUVEC) and microvasculature	hepatic fibrosis development, progression and potential resolution	• Spontaneous cellular disease induction and resolution	
Hepatic tumor cells (HepG2) and monocytes in central collagen I hydrogel channel and T cells delivered in microfluidic channel	Modelling of hepatocytes chemotactic T cell migration induction and monocytes suppression activity	• HepG2 expressing both *HBV envelope protein* and GFP and T cells expressing tumor specific T cell receptors (TCR-T)	[62, 63]

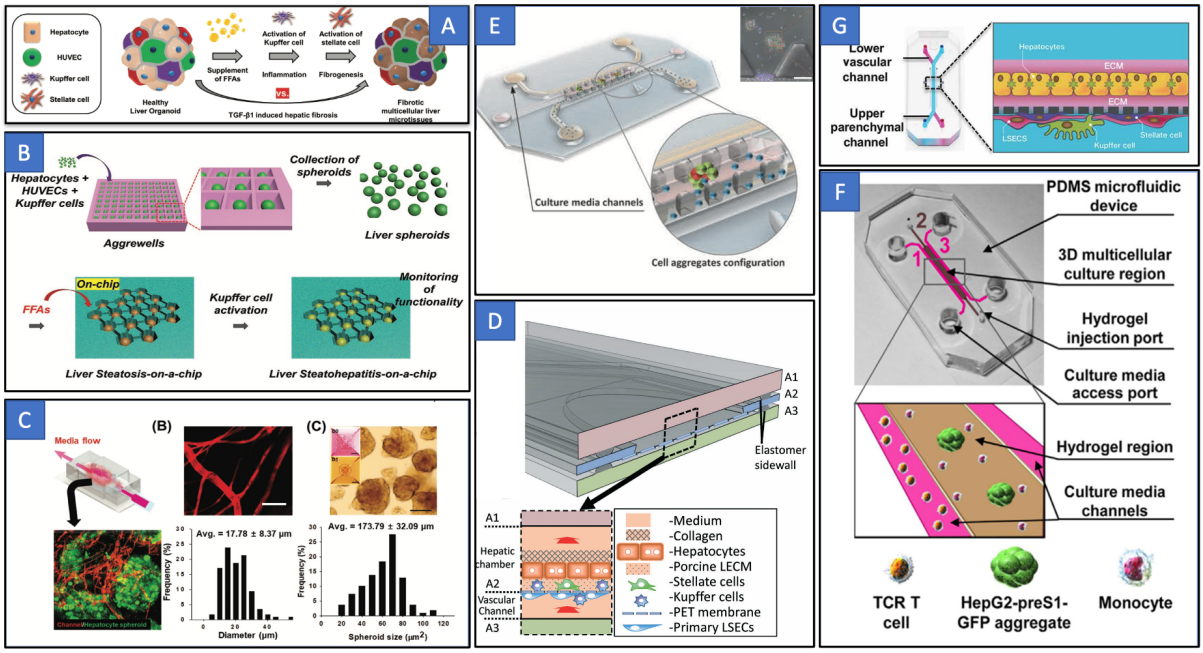

Figure 3. *Relevant models of 3D in vitro engineered liver fibrosis.* ***(A)*** *In this study, an in vitro human liver model of NAFLD is establish by coculturing the four key parenchymal and non-parenchymal cells in a liver organoid. The NAFLD driven fibrotic condition were induced by i) TGF-β treatment or ii) FFA supplemented medium treatment and the two pro-fibrotic cascades of event were compared in terms of disease progression and resolution, establishing a physiological relevant 3D fibrosis in vitro model for potential drug screening [61].* ***(B)*** *By integrating the previous liver organoid model into an array of interconnected honeycomb structures they established a NAFLD-on-a-chip platform and further explored how a fibrotic state induced by the natural progression of NAFLD given by intracellular interaction and FFA medium supplementation differs from the TGF-β -supplemented artificial fibrosis, providing a promising platform for high throughput screening of pro fibrotic compounds [59, 60].* ***(C)*** *A 3D perfusable liver system was established by extruding a perfusable 3D vascular network in a gelatin hydrogel with physiologically relevant stiffness (650 Pa) and co-culturing liver mouse spheroids. Progressive NAFLD stages were modelled by supplementing the culture medium with soluble pro-fibrotic factors [56].* ***(D)*** *A sandwich-like glass microfluidic device was developed by assembling a three layers device with parenchymal and non-parenchymal cells, creating a vasculature channel separated from the hepatic chamber by a porous membrane that at the same time allows the communication between the two. The vascular channel is lined with endothelial cells, recapitulating their immunological functions, including activation, increasing permeability and immune cell binding and extravasation in the hepatic chamber. The hepatic inflammatory response was studied upon medium supplementation with pro-fibrotic molecular drivers [58].* ***(E, F)*** *a microfluidic model was developed by encapsulating in a central hydrogel channel liver tumor spheroid expressing an HBV envelope together with monocytes and loading in an adjacent communicating medium channel tumor specific TCR-engineered*

T cells. The ability of TCR-engineered T cells to transmigrate toward physical and metabolical barriers driven by hepatic tumor – monocytes chemotactic action was investigated and characterized in this platform [62, 63]. ***(G)*** *in this study, an already established [64] dual layer device divided into a perfused upper parenchymal channel containing a monolayer of hepatocytes embedded in bulk hydrogel and separated by porous membrane from a perused vascular channel was validated as a potential in vitro platform for hepatic disease modelling and drug screening. Early and late NASH fibrosis stages were induced upon pro-fibrotic soluble factor treatment and hepatic recovery studied after anti-fibrotic drug treatment [57].*

2.5. General aims and specific objectives

The aim of this thesis project is to establish a physiological-relevant *in vitro* 3D model to study the effects of the mechanical properties of the matrix on liver tissue fibrosis development and functioning, by: *i*) establishing a liver microtissue model in form of a multicellular hepatic spheroid model; ii) providing it with a physio-pathological relevant tissue microenvironment mimicking key mechanical and biological feature.

We hypothesize that the resemble of key tissue mechanical properties (stiffness, interstitial flow, hydrostatic pressure) over typical pathophysiological ranges of value might promote cell differentiation into pro-fibrotic phenotype *via* the activation of latent pro-fibrogenic growth factors generating a pro-fibrotic cascade of event, thus leading and perpetuating a fibrotic microenvironment. The specific objectives of this project are:

- To integrate key parenchymal and non-parenchymal hepatic cells into a multicellular hepatic spheroids 3D model and characterize it:
    - at the microscopical level (growth, morphology, viability, cell distribution);
    - at the molecular level (gene and protein expression).
- To investigate and characterize GelMA hydrogels as platforms suitable for promoting and sustaining 3D pro-fibrotic mechanosensitive cellular behavior over ranges of stiffness that resemble the typical pathophysiological values, via:
    - mechanical characterization (rheological measurements, elastic moduli);
    - structural and chemical characterization (relative pore sizes, actual degree of methacrylation);
    - Biological/biomimetical characterization and pro-fibrotic assessment (bulk hydrogels ECM-cellular interaction, gene and protein expression)
- To develop and optimize a microfluidic platform capable of hosting a multiplex of different stiffness cell-laden hydrogels in a more biomimetic and dynamic environment, via:
    - design requirement characterization (biomimicry, hydrogel confinement, supernatant collection);
    - interstitial fluid flow and fluid pressure promotion and characterization (computational simulation, experimental setup establishment);
    - Vascular endothelium formation and characterization (channel endothelialization, microvascular network formation).

2.6. Overview and experimental approach

Therefore, the project initially proceeded in three independent and successive steps: 1) The development of a multicellular hepatic spheroid model, 2) the investigation and characterization of a bulk hydrogel resembling the *in vivo* ranges of stiffness, 3) the development of a microfluidic platform, providing hydrogel confinement, interstitial fluid flow and vascularization in a controlled way.

Subsequently to point 1) and 2) and in parallel with point 3), the characterized spheroid model and hydrogel platforms were integrated in a 3D *in vitro* model of tissue fibrosis was developed by integrating the characterized spheroids with the hydrogel platforms in the presence of immune cells. Functional fibrotic read-out analyses (metabolic, genomic, immunohistochemical) were carried out to assess the pro-fibrogenic induction (**Figure 4**).

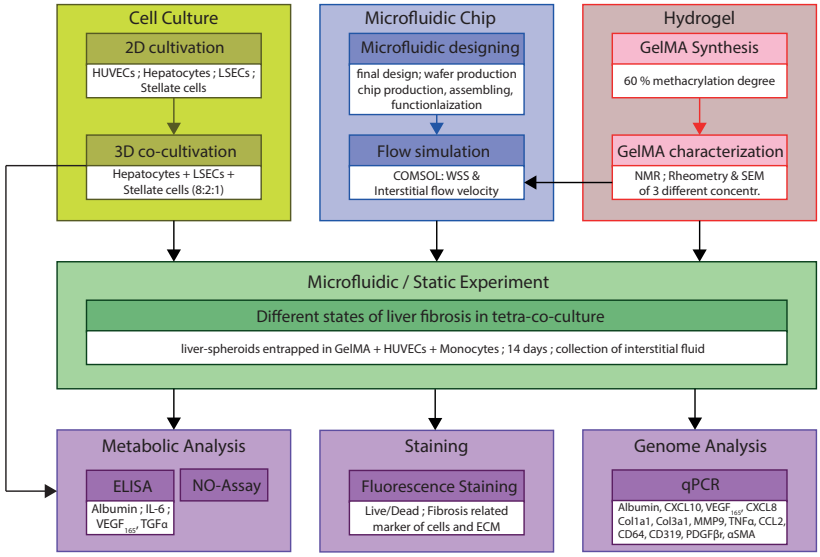

***Figure 4**. Schematic representation of the experimental workflow.*

2.6.1. **Hepatic cell culture**

In order to establish a relevant *in vitro* hepatic 3D model, immortalized parenchymal and non-parenchymal hepatic cell lines were incorporated together in a spheroid model. In this multicellular platform the parenchymal cancer hepatic cell line (HepG2) was integrated with the non-parenchymal hepatic stellate cell line (LX2) and endothelial cell (HUVEC) in a physiological-like ratio: 8:2:1 (HepG2:HUVEC:LX2) [8]. The resulting spheroids were co-culture for 7 days in a rounded bottom microwell array platform and monitored and characterized in term of growth, viability, cell distribution, protein secretion and expression throughout the entire period of culture in order to identify the best culture time point for cell harvesting and hydrogel integration.

2.6.2. **Hydrogel choice and characterization**

In order to establish an *in vitro* model that can effectively recapitulate the native hepatic *in vivo* 3D tissue architecture as well as chemical and structural composition, gelatin metacrhyloyl (GelMA) hydrogel was exploited. GelMA scaffold has been proven high biocompatibility, cell binding and high level of albumin and urea production when hepatocytes are embedded [65, 66]. Furthermore, it provides great mechanical tunability over physiological-like ranges of stiffness, pore size and porosity [67], providing an excellent microenvironment for cells mimicking the native ECM.
GelMA was therefore synthesized at the theoretical methacrylation degree of 60% in order to obtained hydrogel with stiffness values and pore size ranging in the liver native values [67-69]. By varying GelMA ratios (w/v %), different GelMA hydrogel were characterized in term of native pathophysiological stiffness values and the most significant were selected and further characterized in order to assess the actual pore size and degree of methacrylation.

2.6.3. **3D static *in vitro* model**

Subsequent to hepatic spheroids and GelMA hydrogels characterization, these were integrated in a 3D static *in vitro* platform. Together with the hepatic spheroids, single HUVEC and monocytic THP1 cell lines were integrated in the physiological-like total ratio of 8:2:2:1 (HepG2: HUVEC: THP1: LX2) [8] in linear stiffness GelMA hydrogels (**Figure 5**). The resulting 3D *in vitro* platforms were kept into static culture for about 14 days and characterized at the microscopic level in terms of cell morphology, growth and viability; and at the molecular level in terms of relative pro-fibrotic gene expression by quantitative polymerase chain reaction (qPCR), protein secretion by enzyme-linked immunosorbent assay (ELISA) and protein expression by immunofluorescence (IF) staining.

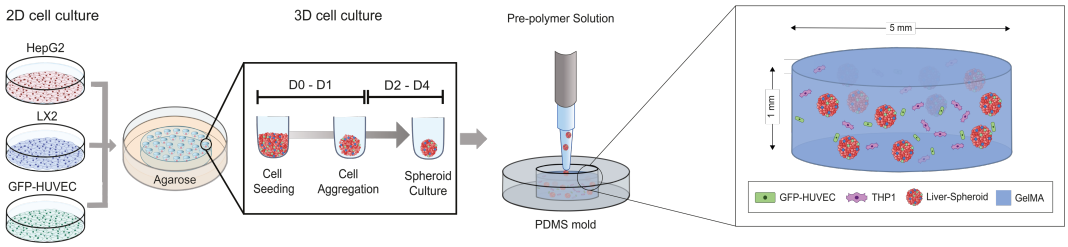

***Figure 5**. 3D static liver in vitro model workflow: from co-culture spheroids aggregation and culture to linear stiffness hydrogels integration together with single endothelial and immune cells.*

2.6.4. **Microfluidic chip**

The liver lobule on-a-chip (LLOC) platforms were designed to host and perfuse the above-mentioned hepatic 3D *in vitro* systems in a more biomimetic and *in vivo* like dynamic environment (**Figure 6**). To accomplish that, a hexagonal-shape microfluidic platform was designed in order to provide simultaneous perfusion of three separated hydrogel pockets, resembling three different physio pathological stages of tissue fibrosis in one single platform. The LLOC consists of three main types of communicating compartments: i) the medium channels, ii) the hydrogel chambers and iii) the supernatant channels. The medium channels were designed to provide physio-pathological relevant wall shear stress and interstitial fluid flow velocities [70, 71] to the three separated hydrogel pockets. The three hydrogel chambers are characterized by a small hydrogel inlet corridor and are delimited by 3D triangular shape micropillars that create small fenestrations between the hydrogel and the other two compartments, allowing interstitial fluid passage from the inlet medium channels to the supernatant compartment. The latter branches over two adjacent sides the hydrogel chamber and is characterized by two outlet reservoirs on both ends for supernatant collection (**Figure 7**).
By applying a difference in the flow rates between the inlet and the three outlets in the medium channels, an interstitial fluid flow running from the medium outlet through the hydrogel pockets is mechanically induced, resulting in fluid accumulation at the supernatant chamber.
Further, the connection of the embedded spheroids with the side blood vessels can be realized through a microvasculature network formed along the supernatant chamber upon channel endothelialization as previously proven [72]. Ideally, the endothelial cells present in the hepatic spheroids and GelMA and the endothelial layer from the side supernatant chambers will anastomose (connect), resulting in a vascularized microfluidic platform. During perfusion, would be therefore possible to further characterize the platform to assess different aspects of this process, including microscopical

observation and protein expression, gene expression and soluble factor secretion in the supernatant channel.

Lastly, previously activated monocytes can be seeded on the endothelialized supernatant chambers and the potential interaction with the fibrotic microenvironments can be potentially studied and characterized, in terms of soluble factor secretion, transdifferentiation, migration and extravasation.

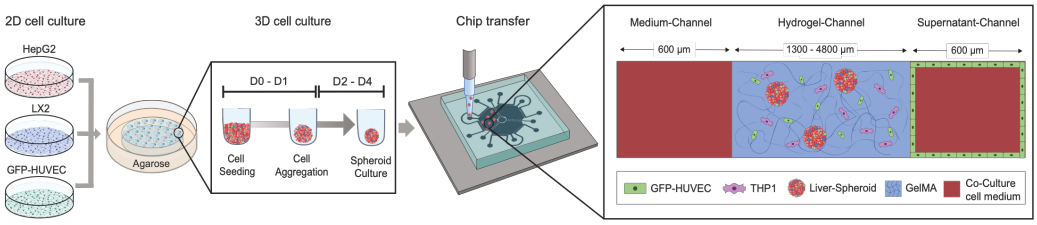

Figure 6. *Microfluidic chip workflow: from co-culture spheroids aggregation and culture to linear stiffness hydrogels integration together with single endothelial and immune cells in LLOC hydrogel chamber and channel endothelialization.*

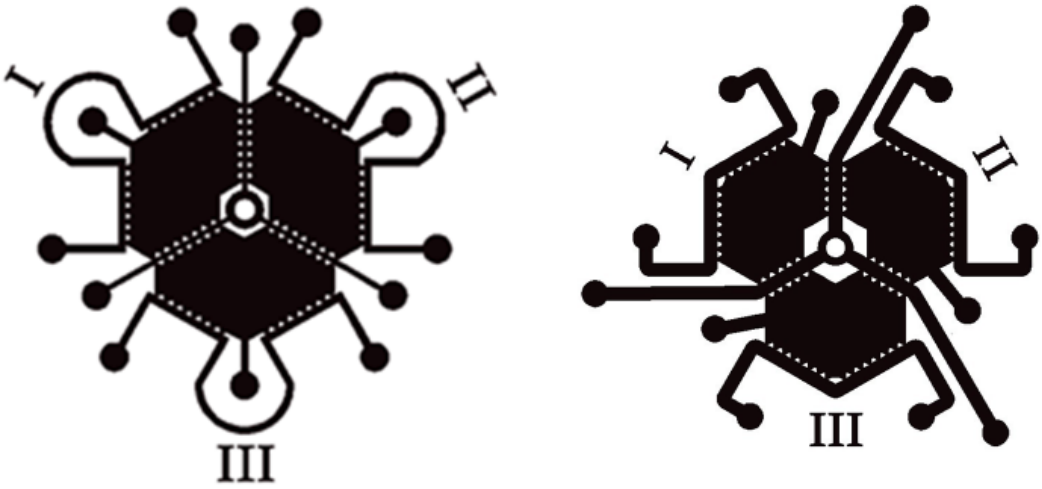

Figure 7. LLOC first and second design and *features. The LLOC consists of three main types of communicating compartments: i) the medium channels, ii) the hydrogel chambers and iii) the supernatant channels. The three hydrogel chambers are characterized by a small hydrogel inlet corridor and are delimited by 3D triangular shape micropillars that create small fenestrations between the hydrogel and the other two compartments, allowing interstitial fluid passage from the inlet medium channels to the supernatant compartment. The latter branches over two adjacent sides the hydrogel chamber and is characterized by two outlet reservoirs on both ends for supernatant collection.*

3. Matherial and methods

3.1. GelMA preparation and Characterization

3.1.1. **Synthesis**

Gelatin methacryloyl (GelMA) was synthesized as described previously with a degree of methacrylation (or methacryloyl distribution) of about 60% [73]. In brief, gelatin was dissolved at a concentration of 10% (w/v) in DBPS at 60° and stirred until entirely dissolved. Methacrylic anhydride (MA) was then added dropwise to the gelatin solution at a rate of 0.5mL/min at 50°C and allowed to react for 1 hour under continuous stirring. After a 5x volume dilution with additional pre-warm DPBS at 40°C to stop the reaction, the resulting GelMA solution was dialyzed against distilled water with a 12-14 kDa dialysis tubing at 40°C for 1 week to remove salts and methacrylic acid. The GelMA solution was then lyophilized and stored at -20°C until further use.

3.1.2. **NMR analysis**

The degree of methacryloyl functionalization was quantified by using ^{1}H NMR according to a previously descried method [73]. GelMA macromers were dissolved in deuterium oxide (D_2O) at a concentration of 10mg/mL and ^{1}H NMR spectra were analyzed by using an NMR spectrometer (JEOL Co. Ltd., Tokyo, Japan) at a frequency of 400MHz. The obtained spectra data was analyzed using MestReNova software. The areas of the peaks were integrated after baseline correction. The degree of methacryloylation (DM) was calculated as the percentage of ε-amino groups of gelatin modified with methacryloyl groups as follows [74]:

$$DM\ (\%) = \left(1 - \frac{A(Lysinemethyleneof GelMA)}{A(Lysinemethyleneofunmodifiedgelatin)}\right) x100$$

3.1.3. **GelMA hydrogel Preparation**

Lyophilized GelMA pre-polymers were fully dissolved at different working concentrations (w/v) in DPBS at 60°C. Photo initiators (PIs) Ruthenium and Sodium Persulfate (Ru and SPS) were added to the different macromer solutions at a 1mM/10mM (Ru/SPS) final concentration, and the working solution was crosslinked in open air using visible light (JOBMATE, 20W LED).

3.1.4. **Rheology**

The viscoelastic properties of GelMA gels were studied using parallel plate geometry (PP8, 8mm) on a stress-controlled rheometer (Physica MCR301, Anton Paar). The parallel plate and bottom rheometer plate were blasted with suitable sandpaper to prevent slipping. GelMA hydrogel samples were prepared as described above. Post crosslinking, each hydrogel pallets (8mm diameter and 1mm thick) was placed onto the rheometer plate at ambient room temperature (20 °C) and the parallel plate was lowered to the desired gap height of 1 mm. A homemade 3D printed solvent trap was used to present evaporation during the rheological measurement. The frequency sweep measurements at a constant strain 0.1% were carried out to examine viscoelastic properties of hydrogels. The amplitude sweep measurements at a constant 1Hz frequency (f) were performed out over the range of 0.1% till 1000%

strain (γ) to examine viscoelastic properties of hydrogels. The storage (G') and loss modulus (G'') were determined as the frequency (f) and strain (%) changes.

3.1.5. Scanning electron microscopy (SEM)

For scanning electron microscopy (SEM), GelMA hydrogels with different concentration (5%, 9%, 12% (w/v)) were prepared as described above. Briefly, 1mL of pre-polymer solution was added into a 24 well plate followed by 4 minutes of bright field crosslinking, obtaining a hydrogel slab of about 15 mm diameter and 8 mm thickness. The hydrogels were fixed in 2.5% glutaraldehyde for 24 at 4°C. After a DBPS washing step, the hydrogels were flash freezed in liquid nitrogen and lyophilized till completely dried. The lyophilized hydrogels discs were then shock freezed into liquid nitrogen and broken to observe the cross-section, gold-sputtered (Sputter Coater 108 Auto, Cressington Scientific Instrument) and imaged using SEM (JSM-IT100, JEOL). Three different representative regions of the same hydrogel sample were imaged, and pore sizes were measured within each group using ImageJ software, by calculating the average between the maximum and minimum diameter per pore.

3.2. Agarose preparation and microwell fabrication

UltraPure agarose powder (Invitrogen, 16500100) dissolved at a concentration of 4% (w/v) in distilled water (dH_2O) was melted and poured on the top of a negative polydimethylsiloxane (PDMS) customized mold composed of 1500 cylindrical microwells of 200 µm diameter and 200 µm depth. Once fully covered with the agarose solution the plate was centrifuged at 2500 rpm for 3 min at 20°C and incubated for 1 hour at 4°C in order to obtain a complete gelation of the agarose solution. The casted agarose mold was then removed from the negative PDMS mold with a spatula and stored at 4°C in DPBS in a 12-well suspension culture plate until further use (**Figure 8**).

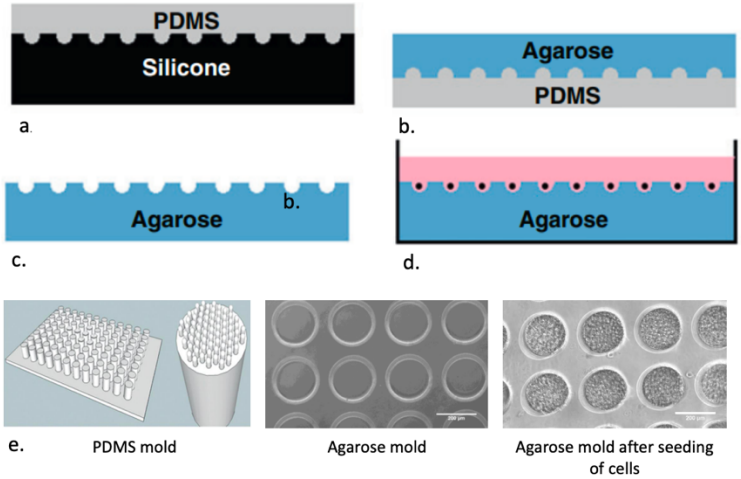

Figure 8. *Schematic descriptions of agarose microwell platform for spheroids formation: production of the PDMS master mold (a), pouring of the PDMS mold with agarose (b), removal of the casted agarose mold (c) and cell seeding (d). Overview of the resulting PDMS mold and agarose mold before and after cell seeding (e). Adapted from [49, 75].*

3.3. Cell culture

HepG2 and LX2 cells were cultured in high glucose, without glutamine Dulbecco's Modified Eagle Medium (HG-DMEM) (Gibco, 11960044) supplemented with 10% fetal bovine serum (FBS) (Sigma, F7524), 2 mM L-alanyl-L-glutamine (Gibco GlutaMAX™, 35050061) and 1x Pen/Strep (Gibco, 15140-

038). HUVECs were cultured in Endothelial Cell Basal Medium 2 (PromoCell, C-22211), supplemented with Endothelial Cell Growth Medium 2 (EGM-2) SupplementMix (PromoCell, C-39216) and 1% (w/v) of 1x Pen/Strep. THP-1 cells were cultured in suspension in Roswell Park Memorial Institute (RPMI) 1640 Medium (Gibco, 21870076) supplemented with 10% FBS, 1mM L-alanyl-L-glutamine and 1% (w/v) of 1x Pen/Strep. HepG2, LX2, HUVECs and THP-1 were used till passage 15, 30, 7 and 25 respectively.

3.3.1. **THP-1 activation**

Human THP-1 cells were seeded at a density of 10^5 cells/mL in a cell-culture well plate and treated with 50 ng/mL of phorbol-12-myrisstate-13-acetate (PMA) (Cayman Chemicals) in RPMI media for 16-20 h. Subsequently, cells were washed with PBS 1x and gently recovered with a cell scraper.

3.4. Hepatic co-culture spheroids

3.4.1. **Hepatic co-culture spheroids formation**

A total of 0.4 x 10^6 cells comprising of HepG2, HUVECs and LX2 at 8:2:1 ratio was diluted in 200 µL of HG-DMEM: EGM-2 medium in a 1:1 or 9:2 ratio and seeded in each mold. Right after seeding, molds were incubated at 37°C under 5% CO_2 for 30 min in order to induce cell precipitation in the microwells under gravitational force, resulting in homogeneous size spheroids of approximately 267 cells each. After that, 1.8 mL of DMEM + EGM -2 medium was added to each mold. Spheroids were cultured at 37°C under 5 % CO_2. Every day, half of the total medium was changed, and spheroids compaction was analyzed. Spheroid's harvesting was performed by gently pipetting up and down the medium in the mold, following by 2-3 extra washing steps in DPBS till the complete removal of spheroids from the well. The spheroids suspension collected was then centrifuge (300 g, 3 min), supernatant decanted and the spheroids' pellet resuspended in the desired volume of fresh medium or GelMA hydrogel.

3.4.2. **3D spheroid culture morphological analysis**

Spheroid's organization and morphological progression were evaluated with bright field microscopy every day during 7 days of cultivation using an EVOS FL Imaging System (ThermoFisher Scientific, AMF4300) and analyzed with a custom MATLAB graphical user interface for quantitative automated data analysis (MeVa, Vascularization Lab 2018). Briefly, bright field pictures of 3x4 microwells array containing spheroids were saved in Tagged Image File Format (TIFF) and uploaded to the MeVa.exe program. After semi-automatic adjustments of key pictures parameters (image sensitivity and debris removal), quantitative information over spheroid's area, perimeter, centroids, and maximum and minimum length were extracted. Diameters were obtained from the calculated areas by approximating each spheroid to a perfect circle.

3.4.3. **Hepatic spheroid Live/dead viability assay**

Spheroid's cell viability was daily determined by incubating the samples with the Cellstain Double Staining kit (Sigma-Aldrich, 04511-1KT-F). In detail, a solution of 2 µL of Calcein-AM and 1 µL of Propidium Iodide (PI) in 1mL of fresh medium was added to a spheroid previously harvested from the mold and incubated at 37°C and 5% CO_2 for 15 min. Spheroid's viability was evaluated using an EVOS

FL Imaging System (ThermoFisher Scientific, AMF4300). The number of dead cells were manually counted in ImageJ using the Cell Counter Plugin.

3.4.4. **GFP-HUVEC distribution in hepatic co-culture spheroids**

GFP-HUVEC distribution over time inside the tri-culture spheroids was daily evaluated using an EVOS FL Imaging System with a GFP Light Cube (482/25 nm excitation, 524/24 nm emission) overlayed to the transmitted-light channel. The HUVEC region's area were analyzed in ImageJ and the average diameter calculated as previously described in the spheroid's compaction section.

3.5. Static condition

A total of 2500 cells, comprising of tri-culture hepatic spheroids, single GFP-HUVEC and Blue CMAC stained PMA-activated THP-1 cells were mixed with 25 µL of the three GelMA prepolymer concentrations (5%, 9%, 12% (w/v)) together with PIs and photo-crosslinked for 4 min in 5 mm diameter x 1 mm height PDMS molds. Right after complete gelation, the cell-laden GelMA hydrogels were seeded in 24-well flat-bottom ultra-low attachment plates (Costar, Corning, 3473) and daily supplemented with the tri-culture medium (HG-DMEM: EGM-2: RPMI, 1:1:1 ratio) for 14 days. Cell's growth and behavior were analyzed daily with the EVOS microscope. GFP Light Cube pictures representing GFP-HUVEC signal distribution over time were analyzed on ImageJ. Briefly, the analyzed pictures were each divided into three different regions of known area and HUVEC density were calculated by using the Cell Counter Plugin.

3.5.1. **Static condition Live/dead viability assay**

Cell viability was determined after 14 days of culture with the above-described kit. Briefly, a solution of 2 µL of Calcein -AM and 1 µL of Propidium Iodide in 1mL of fresh medium was added to the sample and incubated at 37°C and 5% CO_2 for 30 min. Samples' viability was qualitatively evaluated using an EVOS FL Imaging System (Thermo Fisher Scientific, AMF4300).

3.6. Fluorescently labelling of cells

3.6.1. **Immunofluorescence staining**

Two-dimensional cell cultures and spheroid cultures were both firstly seeded on cell culture plates and incubated with their specific growth medium in order to promote cell-substrate adhesion. Cell culture samples were fixed with 4% (w/v) formaldehyde (Sigma-Aldrich, F8775-25mL) at room temperature for 10 min in case of 2D culture or 30 min for 3D culture, permeabilized with 0.1% (w/v) Triton-X 100 (Sigma-Aldrich, 900-93-1) for 10 min or 30 min, and incubated for further 45 min or 1 hour at room temperature in 1% (w/v) FBS, in order to block any non-specific antibody binding. Next, 2D cell cultures were incubated overnight at 4°C with 1:200 primary antibodies in DPBS, while 3D cell cultures were incubated for 48 hours with 1:100 primary antibodies (**Table 3**). Primary staining was followed by 2 hours of incubation at room temperature with 1:2000 or 1:1000 of the corresponding secondary antibodies for 2D and 1:200 for 3D culture (**Table 4**) and 1:50 of Alexa-Fluor™ 647 phalloidin (Thermo Fisher Scientific Inc, A22287) in DPBS and then washed. Cell cultures were therefore incubated for 5 min at room temperature in 1:2000 Hoechst 33342 (Thermo Fisher Scientific Inc,

H1399) and finally stored in DPBS at 4°C. Three washing steps with ice-cold DPBS were performed between each step.

Table 3. *Primary antibodies used for immunofluorescent staining.*

Name	Product	Source
CD31	Rabbit anti CD31	Abcam (ab32457)
Alpha-SMA	Mouse anti alpha Smooth Muscle Actin	Sigma Aldrich (A2547)
Albumin	Rabbit anti albumin	Abcam (ab207327)
Collagen I	Mouse anti collagen I	Thermo Fisher (MA 1-25771)
Collagen III	Rabbit anti collagen III	Abcam (ab154993)

Table 4. *Secondary antibodies used for immunofluorescent staining.*

Product	Source
Alexa Fluor™ 488 goat anti-rabbit	Thermo Fisher (A11034)
Alexa Fluor™ 488 goat anti-mouse	Thermo Fisher (A32723)
Alexa Fluor™555 goat anti-mouse	Thermo Fisher (A21424)
Alexa Fluor™ 594 goat-anti mouse	Thermo Fisher (A11032)
Alexa Fluor™ 647 goat-anti rabbit	Thermo Fisher (A21244)

3.6.2. **CellTracker™ Labelling**

Previously cultivated cells were labelled with CellTracker™ vital dyes (Red-fluorescent CMTPX, Blue CMAC; Molecular Probes) according to manufacturer's protocol. Briefly, harvested cells were centrifuged and resuspended in a solution of 1 µL of CellTracker™ dye in 1mL of fresh medium every million cells and incubated for 45 min at 37°C. Next, the CellTracker™ working solution was removed upon centrifugation and cells resuspended in fresh medium and further cultured.

3.6.3. **Q-tracker™ cell labelling**

Previously cultivated cells were labelled with QTracker™ Cell Labelling Kit (QTracker™ 585 Cell Labelling Kit, QTracker™ 705 Cell Labelling Kit; Invitrogen) according to manufacturer's protocol. Briefly, harvested cells were centrifuged and resuspended in a 10 µM labelling solution, consisting of 1µL Qdot nanocrystals and 1µL β-Amino acid oligomers in 400 µL of fresh medium every million cells and incubated for 45 min at 37°C. Next, the QTracker™ labelling solution was removed upon centrifugation and cells resuspended in fresh medium and further cultured.

3.6.4. **Confocal microscopy**

All samples were imaged using an A1 confocal laser microscope system (Nikon, Japan) using NiS Elements Advanced software (Nikon) through a 20x or 10x air objective, in conjunction with four excitation lasers: 405 nm (Hoechst), 488 nm (Alexa-Fluor 488), 561 nm (Alexa-Fluor 555, Alexa-Fluor

594) and 647 nm (Alexa-Fluor 647). For 3D samples, Z-stacks (120 µm stack, 4 µm steps) were acquired with the Nikon A1 Piezo Z Drive or Ti ZDrive (in case of Z-projections above 100 µm). The coordinates of interest were determined manually using DAPI fluorescence artefact along the sample. Confocal stack images were viewed and sorted using NIS-Element Viewer package (Nikon).

3.7. FACS Cytometry

3.7.1. Spheroid dissociation

Dissociation to single cells was daily performed throughout 6 days of culture. Spheroids were harvested from the agarose molds as previously described and resuspended in 1mL of 1x TrypLE (Gibco, A1217001) in 15 mL falcon tubes upon centrifugation (300 g, 3 min). Afterwards, the tubes were incubated in a water bath at 37°C for 10-15min. To facilitate the process, cells were dissociated by gently pipetting up and down and complete cell detachment was verified by inspecting the tubes under the microscope. Next, 2mL of fresh medium was added in order to inactivate TrypLE solution. Samples were centrifuged (300 g, 3 min), resuspended in PEB Sort Buffer (Ca^{2+} and Mg^{2+} - free PBS, 0.1% BSA and 2mM EDTA) and transferred in FACS tubes.

3.7.2. FACS analysis

Dissociated samples were immediately analyzed with a MACSQuant VYB Flow Cytometer (Miltenyi Biotech) for determining the percentage of stained cells. As a negative control, HepG2, HUVECs and LX2 unstained cell samples were used in order to gait the cell type population (cell size, surface roughness), setting a threshold in order to eliminate debris and doublets. Unstained samples were also used as negative (blank) control for assessing single stained cell population positivity for each laser and to adjust intensity before proceeding with the analysis of the dissociated hepatic spheroids.

3.8. Microfluidic chip production and characterization

3.8.1. Chip/photomask design

Microfluidic setups were designed as described in the *Overview and experimental approach* section using Clewin5 software (WieWeb Software, The Netherlands).
Finalized design files were used to produce in-house the chrome oxide coated quartz glass photomask.

3.8.2. Silicon wafer production

To fabricate the microfluidic design with the desired height of 260 µm it was made use of SU8 photolithography to create a negative mold for the PDMS soft lithography. Therefore, the epoxy-based negative photoresist SU8-100 and silicon P-Type <100> OSP wafer were used for the following steps (**Table 5**):

Table 5. *Silicon wafer production protocol steps.*

Action	Interval and Time

Spin coating of SU-8	rpm 1 = 500 -30 sec rpm 2 = 1500 -30 sec
Soft bake	25°C 50°C – 10 min 65°C – 30 min 95°C – 300 min 25°C
UV Exposure through photomask	Proximity mode: separation 260 µm, proximity 30 µm Exposure: constant time interval – 5 cycles of 20 sec exposure followed by 5 sec delay
Post exposure bake	25°C 50°C – 10 min 65°C – 10 min 75°C – 50 min 25°C (5°C/min)
Develop with RER600	20 cycles of 20 sec spin coating with RER600
	Rinse with RER600
	Rinse with IPA
	Spin dry
	Check results under yellow light microscope and repeat washing steps if necessary

3.8.3. **COMSOL simulations**

The before designed microfluidic design was tested simulating a laminar fluid flow in the fluid channels and transmural fluid flow in the hydrogel compartments using COMSOL Multiphysics (v5.5.0.292, www.comsol.com). To determine a reasonable inlet flow parameter using syringe pumps allowing control about fluid wall shear stress (WSS) and transmural flow velocity, materials properties of the cell culture medium and the different used GelMA concentrations were set based on literature values (**Table 6**). The cell culture medium media was considered as Newtonian.

Table 6. *Input parameters for microfluidic COMSOL simulations.*

Fluid parameters	**Density**	**998.2 kg*m^{-3}**
	Dynamic Viscosity	9,4E-4 Kg*m^{-1}*s^{-1} [76]
	Compressibility	Incompressible flow

Matrix Properties	Porosity	0,01
	Permeability (5 % GelMA)	1E-13 m^2
	Permeability (9 % GelMA)	2E-14 m^2
	Permeability (12 % GelMA)	4E-14 m^2 [77]
Environmental conditions	Temperature	310.15 K
	Inflow rate (final)	0,4 µm*min^{-1}
	Type of fluid flow	Brinkman Equation
	Boundary condition (outlet)	0 Pa
	Boundary condition (wall)	No slip
Study Conditions		
Meshing	Type of mesh element	Physics controlled mesh
	Element size	Extra fine

3.8.4. **Chip fabrication**

The resulting master (SU-8) mold surface was passivated through Trichloro (1H, 1H, 2H, 2H-perfluorooctyl) silane (Sigma-Aldrich, 448931) treatment in the vapor phase for 20 min at room temperature after plasma activation (50W power, 40s generation time, 50 kHz generation frequency, 5.00e-1 torr process pressure; Cute, Femto Science, South Korea), in order to facilitate the positive mold removal. A mixture of PDMS pre-polymer and curing agent (Sylgard™ 184 silicon elastomer kit, Dow Corning) was prepared at a weight ratio of 10:1, thoroughly degassed for 30-40 min in a vacuum chamber, poured on the mold and once more degassed, before being incubated in an oven at 60°C for at least 4 hours. Subsequently, the positive cured PDMS layer was cut and extracted from the mold and reservoirs were created by puncturing the chip with a 1.5 mm diameter biopsy puncher. The PDMS was then cleaned with 70% ethanol and dried using pressured air.
Microscopy glass slides (1 mm thick) were coated with a 80 µm thick 10:1 wt% PDMS layer by means of a spin-coater (SPS Spin 150, SPS-Europe) using the following protocol: 30 s at 500 rpm and 40 s at 3000 rpm and subsequently cured in the oven as described above. Next, both the PDMS-coated glass slides and the PDMS microfluidic chips were activated using the above-mentioned plasma treatment, before assembly.

3.8.5. **Chip GelMA filling and pump connection**

Immediately after the bonding, the resulting microfluidic devices were functionalized with a solution of 3-(Trimethoxysilyl) propyl methacrylate (TMSPMA) diluted in acetic acid and 70% ethanol at the 3: 50: 950 (v/v/v) ratio, respectively, in order to enhance hydrogel attachment to chip's inner surfaces through the introduction of terminal acrylate functional groups [78]. Briefly, the TMSPMA solution was injected into the microfluidic channels and incubated for 3 hours at room temperature. After incubation, microfluidic channels were thoroughly rinsed with 70% ethanol, emptied using pressured air and allowed to dry overnight in the oven at 60°C.
After TMSPMA functionalization, 10 µL of each of the three GelMA prepolymer concentrations mixed with PIs were injected in their respective chip hydrogel pockets and photopolymerized for 4 min under visible light. Right after gelation, the GelMA hydrogels were kept hydrated by manually injecting sterile PBS or fresh medium in the medium and supernatant channels and blocking the outlets by inserting

200 µL filter pipette tips. Chip's inlet was connected via a polyvinyl chloride (PVC) cable to a syringe pump (PHD Ultra, Harvard Apparatus; NE-1600 Six Channel Programmable Syringe Pump, NewEra Inc) and sterile PBS or fresh medium were infused at rates in the order of µL/min. Medium channels outlets were blocked by inserting cured-PDMS filled pipettes tips, while 200 µL filter tips were inserted in the supernatant channels outlets for medium supernatant collection. The microfluidic runs were conducted at 37°C, syringes re-loaded with fresh PBS or medium every 24 h and supernatant collected.

3.8.6. **Chip endothelialisation**

After GelMA loading in the hydrogel pocket of the microfluidic system, the supernatant channels were coated 30 min at 37°C with of 1.0 mg/mL mouse purified laminin (Sigma-Aldrich, CC095-M) in 1x PBS. The microfluidic device was endothelialised by adding 10 µL of 10 x 10^6 cells/mL GFP-HUVEC suspension in EGM-2 medium and incubated for 30 minutes at 37°C. Right after, the same process was repeated and the chip incubated upside down for further 30 min in order to allow cells attachment on both side of the channel. The endothelialised chip was kept in culture for 24 h to ensure the formation of a confluent monolayer, during which the EGM-2 culture medium was passively diffused along the channel through the formation of a gravity-driven flow by inserting medium filled pipette tips in the supernatant channels' outlets.

3.8.7. **PMA-activated THP-1 cells incorporation**

After 24 h of GFP-HUVEC incorporation in the microfluidic device, PMA-activated THP-1 cells were seeded in the same supernatant channels. Briefly, 10 µL of 10 x 10^6 cells/mL CMAC-labelled THP-1 suspension in RPMI medium was pipetted on both sides of the supernatant channels, as previously described for GFP-HUVEC. The co-culture system obtained was kept in static culture for over one week, during which the co-culture medium (HG-DMEM: EGM-2: RPMI, 1:1:1 ratio) was changed daily.

3.8.8. **Chip fibrin filling and cell encapsulation**

The mixture of cells was prepared by suspending GFP-HUVECs (6,665*10^6 cells/mL) and mesenchymal stem cells (MSCs) (6,665*10^6 cells/mL) in a fibrinogen solution of 20 mg/mL (Milipore, 341573-GM) in a ratio of 5:1 (v/v). Afterwards, the cell-fibrinogen solution was mixed with 30 U/mL Thrombin (Sigma-Aldrich, T7513-100UN) in a ratio of 9:1 resulting in a 3 mg/mL Fibrin solution of 10*106 cells/mL with 3 U/mL Thrombin. This solution was mixed and quickly injected into the hydrogel chambers. The gel polymerized for 10 min at 37°C for before medium was injected into the microfluidic chip.

3.9. Molecular analysis

3.9.1. **Quantitative real-time PCR**

GelMA hydrogel samples, after two PBS washing steps, were resuspended in a 15mL tube in 500 µL of 3mg/mL collagenase (Collagenase from *clostridium histolyticum*, Sigma-Aldrich, C9407) and incubated for 60-90 min at 37°C, while manually vortexed every 15-30 min until entirely dissolved. After complete degradationof the GelMA hydrogel, the cell suspensions were centrifuged for 5 min at 300g, and the obtained supernatants discarded. Cells were then lysed using 250 µL/sample of RNA lysis buffer supplemented with mercaptoethanol (10 µL/mL lysis buffer) and the final filtrate were stored at –80°C till further use. The RNA was isolated using standard protocols provided by the manufacturers

(GeneMatrix Universal RNA Purification Kit, EURx). Purity and RNA concentration of each sample were measured using NanoDrop (Nanodrop ND-1000, Wilmington, DE, USA) with a sample size of 2 µL. Complementary DNA (cDNA) synthesis was performed using standard protocols provided by the manufacturer (Bio-Rad Laboratories B.V., Hercules, CA, USA). The qPCR was performed by firstly diluting the cDNA samples to a final concentration of 10 ng/mL using RNAse free water. For each gene measured, a primer master mix was prepared by adding 0.05 µL respectively of the forward and reverse primer (50µM), 4 µL SYBR Sensimix (Bioline Reagents, London, UK) and 1.9 µL RNAse-free water, adding up to a final volume of 6 µL for each well. Subsequently, 2 µL/well cDNA solution were added to the master mix solution, the well was sealed and centrifuge for 1 min at 3000 rpm. The qPCR analysis was performed following a conform standard protocol (C1000 thermal cycler Bio-Rad, CFX 384 RT system). The housekeeping gene Glyceraldehyde-3-phosphate (GAPDH) was used for data normalization and for determination of relative gene expression values. The fold induction values were calculated from the Cq values using the $2^{-\Delta\Delta Ct}$ methods.

3.9.2. Solid phase Sandwich enzyme-linked Immunosorbent assay (ELISA)

Secreted albumin, $VEGF_{165}$, TNF-α and IL-6 were quantified by diluting (**Table 7**) and analyzing the collected culture supernatant using the respective DuoSet® ELISA kits (R&D systems, Minneapolis, USA) as per manufacturer's instructions. The optical density was measured at 450 nm using VIKTOR™ plate reader (Perkin Elmer) and concentrations of the secreted albumin, $VEGF_{165}$, TNF-α and IL-6 were calculated using the respective standard curves.

Table 7. *DuoSet ELISA kits adopted during protein secretion analysis.*

Name	Product	Dilution factor	Catalog Nr.
Albumin	Human Serum Albumin	1:5	DY1455
$VEGF_{165}$	Human $VEGF_{165}$	1:5	DY293B-05
TNF-α	Human TNF-α	1:2	DY210-05
IL-6	Human IL-6	1:2	DY206-05

3.9.3. Nitric Oxide releasing assay

In order to determine the nitric oxide concentration, a Griess medium was prepared by dissolving 1% (w/v) sulfanilamide (Sigma-Aldrich, 63-74-1), 0.1% (w/v) N-(1-Naphthyl)ethylenediamine dihydrochloride (Sigma-Aldrich, N9125) and 2.5% (v/v) of phosphoric acid in milliQ water. After 5-10 min of stirring, 100 µL of the obtained Griess medium was added to 100 µL of collected supernatant cell medium and the respective absorbance at 450 nm was measured with a microplate reader (VIKTOR™, Perkin Elmer). The relative absorbance of each samples was obtained by normalizing each value with the cell culture medium's absorbance values measured at the same timepoint.

3.10. Statistics

All graphs were made using GraphPad Prism Vol.9 (GraphPd Software Inc. 9, San Diego, CA). All values are expressed as a mean ± standard error of the mean (SEM) or standard deviation (SD). Statistical

significance of the results was performed by a one-way or two-way ANOVA test for comparison of two or more conditions, respectively. Differences were considered significant for a p-value of *$p<0.05$, **$p<0.01$, ***$p<0.001$, ****$p<0.0001$ respectively.

4. Results

4.1. GelMA hydrogels stiffness characterization

After combining GelMA prepolymer with a photoinitiator, such as SPS and Rhu, GelMA solutions can be polymerized to produce hydrogels via visible light exposure. The degree of polymerization, which determines matrix stiffness, can be generally manipulated by controlling light exposure time, energy level, GelMA concentration, methacrylation level of gelatin structures, and photo-initiator concentration.

In this research, only the GelMA concentrations (w/v) were manipulated in order to explore the hydrogel's potential mechanical tunability and individualize the conditions for obtaining a physiological-relevant range of linear stiffness values.

In detail, in order to obtain a quantitative characterization of such features, different GelMA hydrogels were prepared with increasing concentration in the range 2.5-15% (w/v) and the respective mechanical behaviors were analyzed through rheological measurements (**Figure 9**).

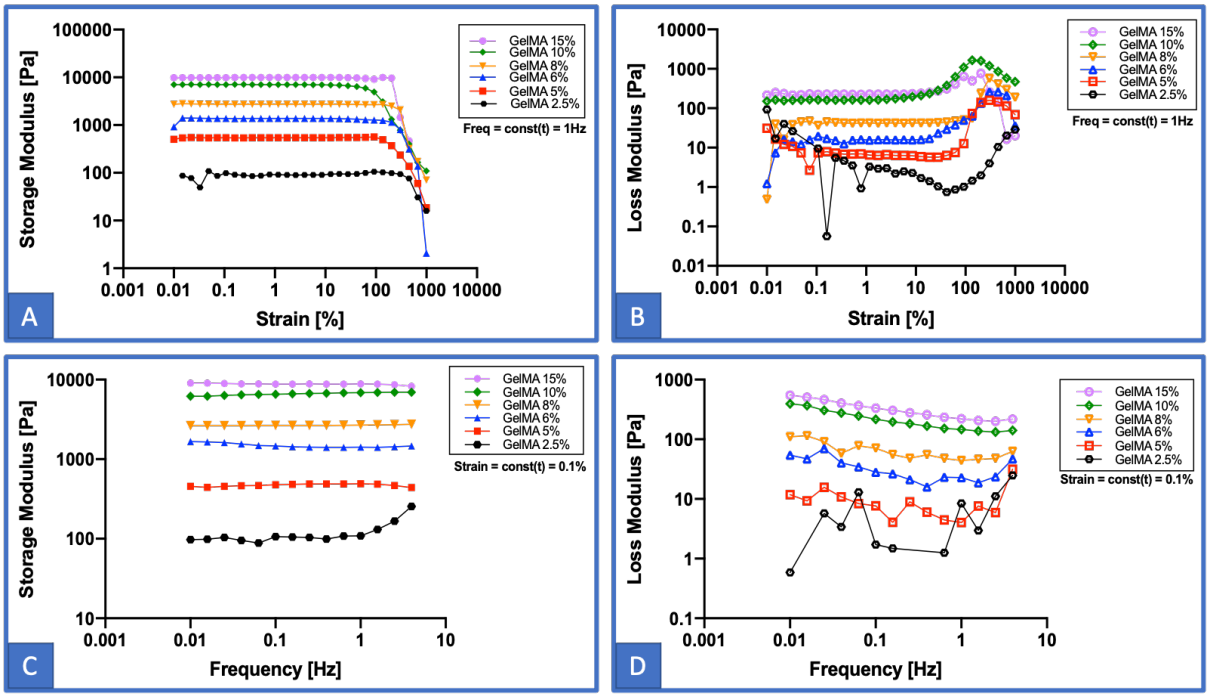

Figure 9. *Rheological characterization of crosslinked 2.5%, 5%, 6%, 8%, 10%, 15% (w/v) GelMA hydrogels. Storage and loss moduli measurements were performed at constant frequency of 1 Hz over the range of 0.1-1000% strain (amplitude sweep measurements) (A), (B), and at constant strain of 0.1% over the range of 0.1-1Hz frequency (frequency sweep measurements) (C), (D).*

From the storage moduli measurements, the linear region values, corresponding to the elastic behavior of the material, were defined, for each GelMA concentration hydrogels the average value was calculated, and the interpolation curve was plotted allowing to study the stiffness values trends as a function of GelMA concentration (**Figure 10**). The graph shows that GelMA hydrogel stiffness increases with a nonlinear trend as the hydrogel concentration increases, from a minimum of 0.090 kPa at 2.5% (w/v), reaching a relative maximum of 10 kPa at 15% (w/v) and featuring a plateau-like behavior, presumably attributable to saturation kinetics in the crosslinking reactions.

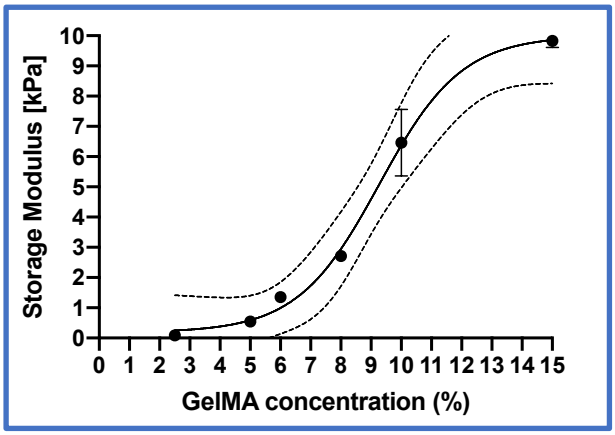

Figure 10. *Storage moduli interpolation curve with 95% confidence bands. Data are the mean value ± SD of three replications (n=3) per GelMA condition in the linear region of the storage modulus measured at constant frequency of 1Hz. Note: when non-visible in the graph, error bars are to be considered smaller than the point itself.*

Furthermore, from the loss moduli measurements (**Figure 9B, D**), the viscoelastic behavior of the different GelMA hydrogel concentrations can be analyzed. From this data a higher viscoelastic behavior under shear stress deformations inversely proportional to GelMA hydrogels concentrations was observed.

4.1.1. **Physiological - relevant GelMA hydrogel selection**

Extensive literature research suggests the comparability between *in vivo* magnetic resonance elastography (MRE) measurements and *ex vivo* rheology results [79, 80]. Under this hypothesis, the obtained GelMA hydrogels storage moduli were compared with data from two different publicly available studies in which liver shear stiffness values of 12 healthy volunteers and 12 patients with chronic liver disease and varying degrees of liver fibrosis were measured through MRE and proved with biopsy results (**Table 8, Figure 11**) [68, 81].

Considering this comparison, three different pathophysiological range of stiffness were identified (G'_{normal} ~ 1-2 kPa, $G'_{stage\ 3}$ ~ 4-6 kPa, $G'_{stage\ 4}$ > 6 kPa) (**Table 9**) and the corresponding GelMA hydrogel concentration, 5%, 9% and 15% (w/v) were selected from the storage moduli's interpolation curve (**Figure 10**).

Table 8. *Typical pathophysiological ranges of liver stiffness measured through magnetic resonance elastography (MRE). Adapted from [79, 80].*

Fibrotic stage	Description	Storage modulus
Normal	Healthy liver	1.2-2.3 kPa
Stage 0	Pre-fibrotic	2.3-2.7kPa
Stage 1	Portal fibrosis	2.7-4.0 kPa
Stage 2	Periportal fibrosis	3.0-4.5 kPa
Stage 3	Septal fibrosis	4.0-6.00 kPa
Stage 4	Cirrhosis	10.0-20-0 kPa

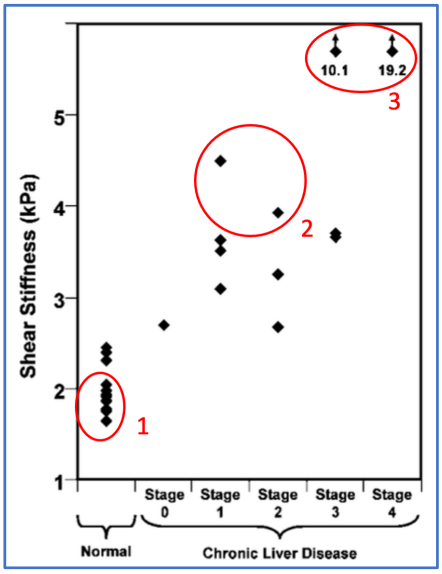

Figure 11. *Graph of distribution of liver shear stiffness in 12 healthy volunteers and 12 patients with chronic liver disease and varying degrees of liver fibrosis proved with biopsy results. Normal: healthy liver, stage 0: pre-fibrotic, stage 1: portal fibrosis, stage 2: periportal fibrosis, stage 3: septal fibrosis, stage 4: cirrhosis. Adapted from [80].*

After the theoretical GelMA hydrogel concentration selection, 12% (w/v) GelMA (G' ~ 9 kPa) was preferred instead of 15% (w/v) as the latter resulted extremely viscous and hard to handle during laboratory experiments.
Therefore, 5%, 9% and 12% (w/v) GelMA hydrogels were the final physiological-relevant concentration selected for mimicking tissue liver fibrosis development.

Table 9. *Measured and interpolated (9%, 12% (w/v) GelMA) storage modulus values as a function of GelMA concentration and their corresponding fibrotic state.*

GelMA %	Storage Modulus	Liver State
2.5	0.09 kPa	-
5	0.6 kPa	Healthy
6	1.4 kPa	Healthy
8	2.7 kPa	Stage 0/1
9	*4.1 kPa*	*Stage 2*
10	7.0 kPa	Stage 3
12	*9.0 kPa*	*Stage 3/4*
15	10.0 kPa	Stage 4

4.1.2. **GelMA hydrogel characterization**

After having identified the three pathophysiological relevant GelMA hydrogel concentrations, the obtained GelMA hydrogels were characterized in terms of relative internal morphology and pore size. Furthermore, the methacrylation degree of the GelMA pre-polymer macromers were analyzed in order to have a complete overview of the hydrogel's features.

4.1.2.1. *GelMA hydrogels Internal morphology and pore size*

The internal morphology of the 5%, 9% and 12% (w/v) GelMA hydrogels was observed by Scanning Electron Microscopy (SEM). From the images obtained (**Figure 12**) GelMA hydrogels revealed a similar, porous internal structure. From the graph reported in **Figure 13** it can be observed that the mean value of pore size decreases with hydrogel concentrations, ranging from a mean value of ~ 42 µm for 5% GelMA, to ~ 12 µm for 9% GelMA ~ 9 µm for 12% GelMA.

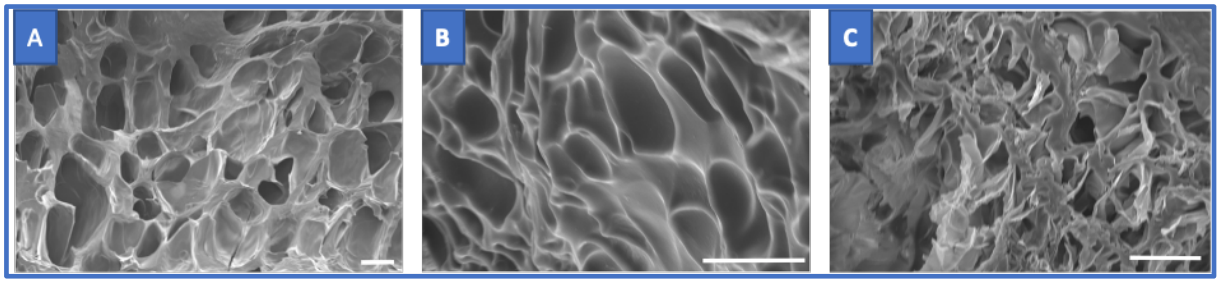

Figure 12. *SEM images of the cross-section of 5% (A), 9% (B), 12% (C) GelMA hydrogel. Scale bars: 20 µm, magnification: 250x (A), 900x (B), 650x (C).*

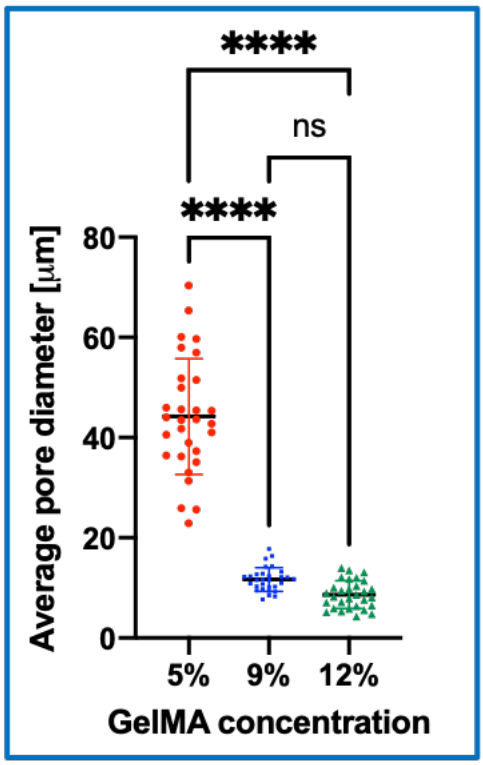

Figure 13. *SEM average pore diameter for 5%, 9%, 12% (w/v) GelMA hydrogels calculated as the average between the minimum and maximum diameter per pore. Data are the mean value ± SD of two independent replications. ****p<0.001, ordinary one-way ANOVA.*

4.1.2.2. *GelMA Methacrylation degree assessment*

The chemical spectrum of GelMA (**Figure 14**) was compared with the spectrum of unmodified gelatin (**Figure S1**). Compared with the gelatin spectrum, GelMA is characterized by new functional groups, marked as blue "A", green "B" and red "C" in **Figure 14**. The peaks at the chemical shifts (f1) of ~ 5.3 and 5.6 ppm were assigned to the acrylic protons (2H) of the grafted methacryloyl group, while a second peak at f1 ~1.9 ppm was attributed to the methyl group (3H) of the grafted methacryloyl group.

Meanwhile, there was a decrease of intensity at ~ 2.9 ppm, which was assigned to the lysine methylene (2H). As lysine is the reaction site, this trend could be used to quantify the DM, which theoretically [73] should be ~ 60%.

From the calculation between these two spectra the actual DM obtained is ~ 37.29%. However, it should be taken into consideration that the herewith gelatin and GelMA spectra were measured in two separated experimental sessions, with slightly different protocols (*i.e.,* different dissolution time), potentially leading to inaccurate DM estimation.

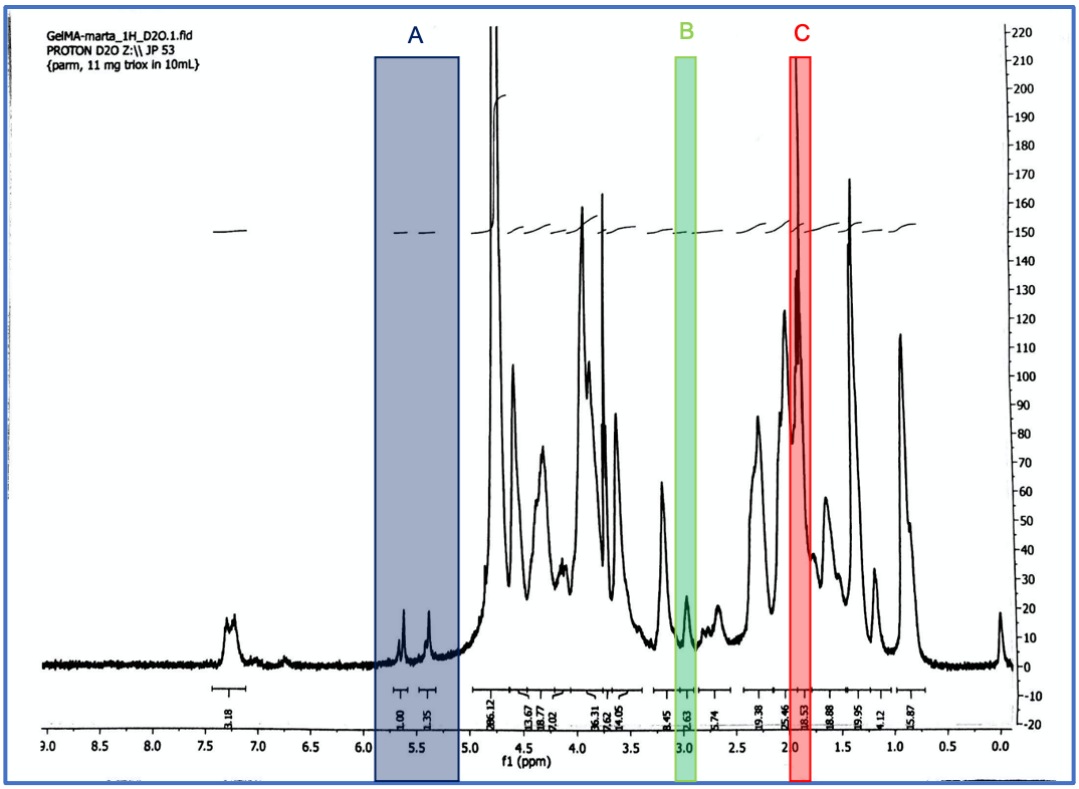

Figure 14. *Chemical structures of GelMA, and its respective 1H-NMR spectra. Red "C" and blue "A" represent the signals of the methyl group and acrylic protons of the grafted methacrylic group respectively, and green "B" indicates the signal of lysine methylene.*

4.2. Tri-culture hepatic spheroids characterization

Concurrent with the hydrogel characterization, a physiological-like multicellular hepatic spheroids model was established and characterized by incorporating key parenchymal and non-parenchymal human hepatic-derived cell lines. Specifically, the hepatic cancer cell line HepG2 was assembled with hepatic stellate cells, LX2, and endothelial cells, GFP-HUVEC, in a physiological-like ratio of 8:2:1, HepG2: GFP-HUVEC: LX2.

Firstly, two different triple co-culture media compositions were tested: *i*) HG-DMEM: EGM-2 in a 1:1 ratio; ii) HG-DMEM: EGM-2 in a 9:2 ratio, resembling the cell ratio. Their influence on hepatic spheroids were analyzed and compared in terms of spheroids growth, viability, HUVEC distribution and cytokine secretion.

4.2.1. Triple co-culture hepatic spheroids formation

4.2.1.1. Spheroid growth and viability

As shown in **Figure 15** the hepatic tri-culture spheroids successfully self-aggregated in the agarose microwell arrays in both media conditions within the first 24 hours of culture.

From an initial diameter of 120-130 µm (day 1), they both linearly increased in size, reaching average diameters of 150 µm and a more rounded shapes at days 3-4 of culture. In both culture conditions, spheroids reached a maximum average diameter (170-180 µm) after 5-6 days. Notably, spheroids cultured in the 9:2 medium ratio showed an average size decreasing trend at day 7 of culture.

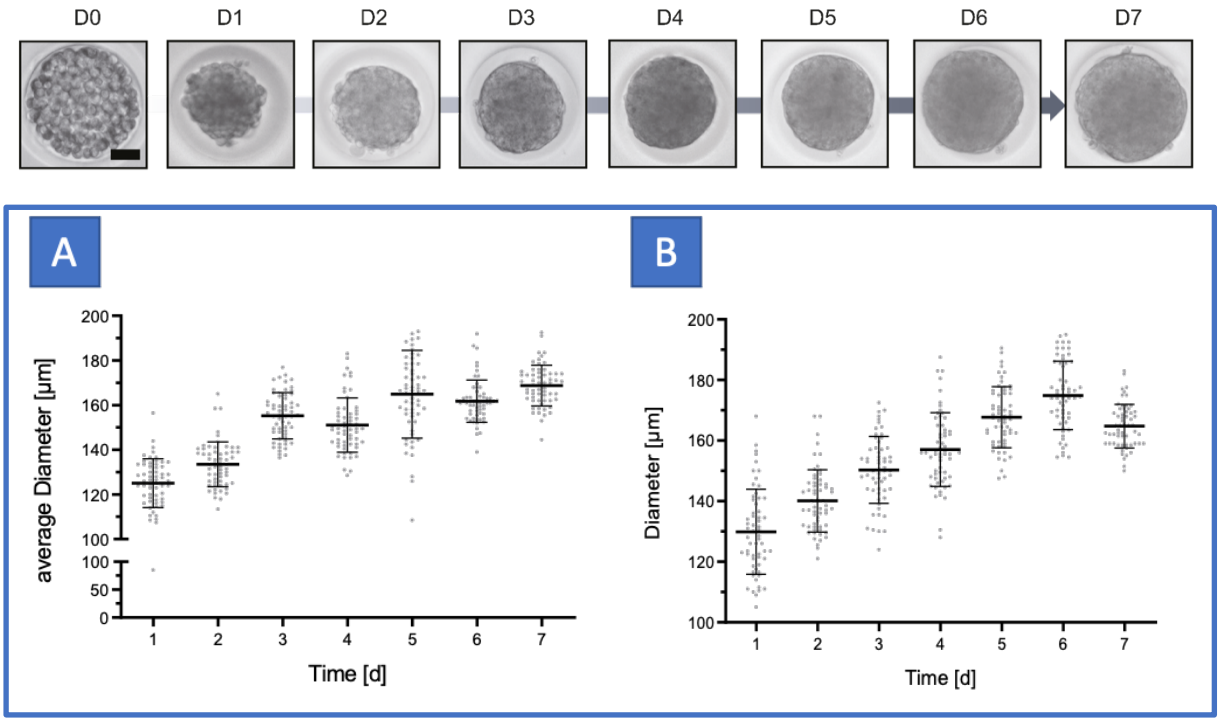

Figure 15. (Top) *Representative bright field pictures of spheroids cultivated for 7 days in the agarose microwell arrays. Magnification is 10x.* ***(Bottom)*** *Quantification of hepatic tri-culture spheroids size over the culture time in the agarose microwell arrays cultured in the 1:1 (A) and 9:2 (B) medium composition. Data are the mean value ± SD; n=60.*

In addition to the growth, spheroids viability in the two medium conditions was assessed by preforming Live/Dead assay over the same 7-day culture period. Cell viability, despite featured a slight decreasing trend over time in the 1:1 medium composition, remained overall above 98% in both culture conditions throughout the entire period of culture (**Figure 16**).

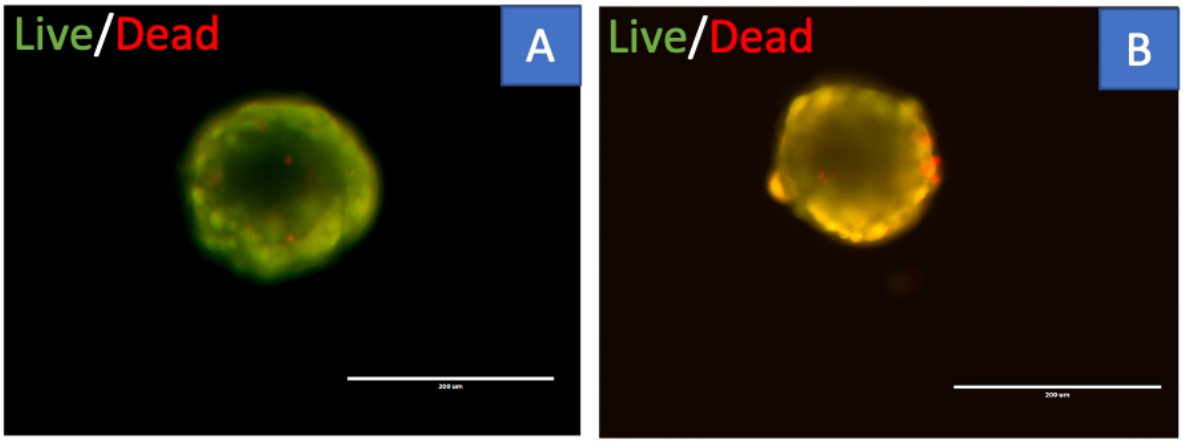

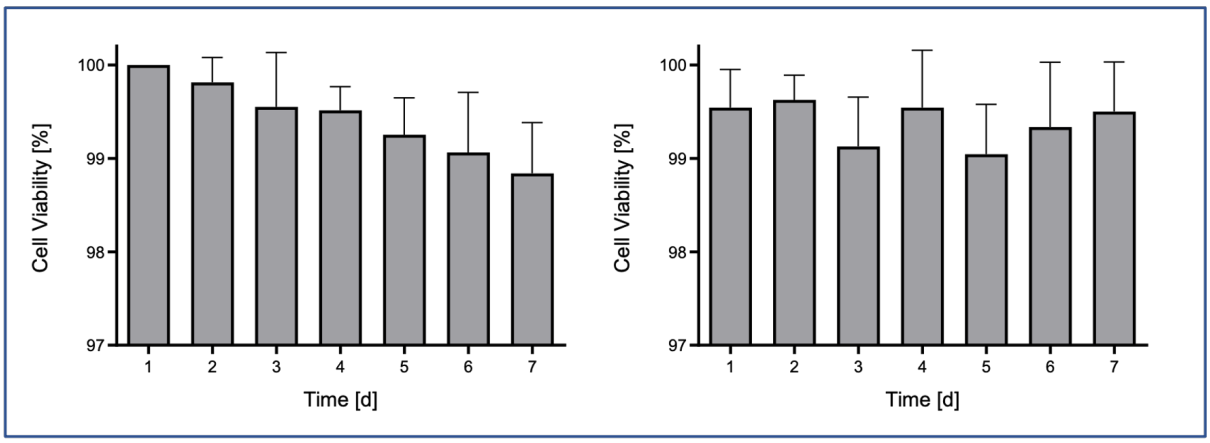

Figure 16. *Hepatic co-culture spheroids live-dead staining cell viability and characterization.* ***(Top)*** *Representative microscopic pictures of live-dead staining in hepatic co-culture spheroids inside agarose microwell arrays at day 7 of culture in 1:1 (A) and 9:2 (B) medium composition. Green (live, Calcein-AM)), red (dead, Propidium iodide).* ***(Bottom)*** *Proportion of cell viability (%) of hepatic co-culture spheroids over the culture time in the agarose microwell arrays cultured in the 1:1 (left) and 9:2 (right) medium composition. Data are the mean value ± SD of ten independent measurements per condition.*

Other than spheroid growth and morphology, GFP-HUVEC growth and distribution inside the hepatic spheroids was analyzed by fluorescence microscopy over the same period of culture. Notably, in both media conditions GFP-HUVEC tended to self-organize themselves in the inner cores as soon as the cell compaction starts (**Figure 17A, B**). Such GFP-HUVEC inner cores featured a constant decrease in size during the whole period of culture and tended to become null from day 6 in the 9:2 medium condition, probably due to the insufficient EGM-2 medium component in the co-culture medium (18%). (**Figure 17**)

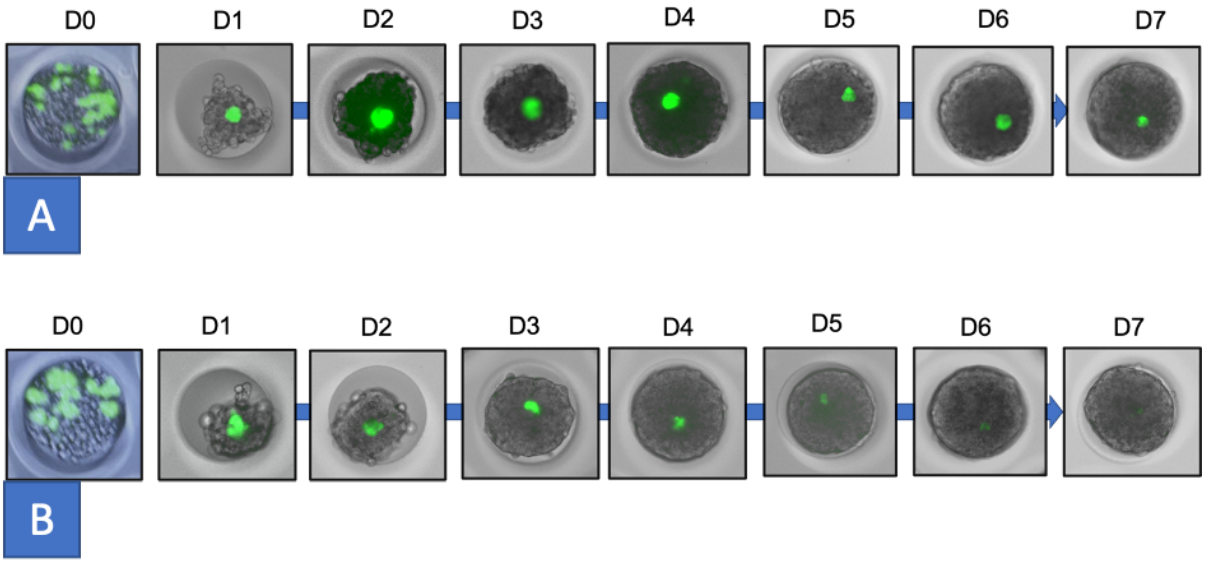

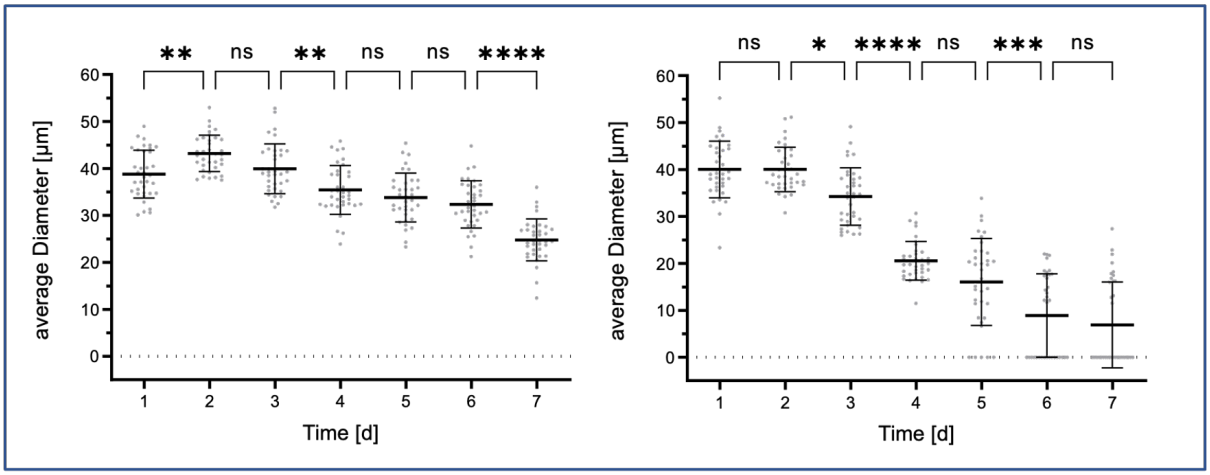

Figure 17. *GFP-HUVEC characterization inside tri-culture hepatic spheroids over 7 days of culture in agarose microwell arrays.* ***(Top)*** *Representative characterization of GFP signal distribution in 1:1 (A) and 9:2 (B) medium composition. Images are the overlay between bright field and GFP pictures. Magnification is 10x.* ***(Bottom)*** *Quantification of GFP signal core size cultured in the 1:1 (left) and 9:2 (right) medium composition. Data are the mean value ± SD, n=36. ****p<0.0001, ***p<0.001, **p<0.01, *p<0.05, ordinary one-way ANOVA.*

Finally, albumin and VEGF secretion in the two medium compositions, detected by ELISA, displayed an overall increasing trend over time (**Figure 18**). Spheroids cultured in the 9:2 medium showed slightly higher albumin secretion, but a marked lower VEGF secretion over time compared to the 1:1 medium, reinforcing the hypothesis that the latter medium composition better supports different cell types growth and crosstalk. Containing the EGM-2 medium about 0.5 ng/mL of VEGF already[1], VEGF secretion was also calculated normalizing the detected values to the normal – unconditioned – 1:1 and 9:2 media (**Figure S2**). interestingly, while VEGF levels in the 1:1 medium did not change significantly, the 9:2 medium composition showed a net decrease of about 63% in the average value.

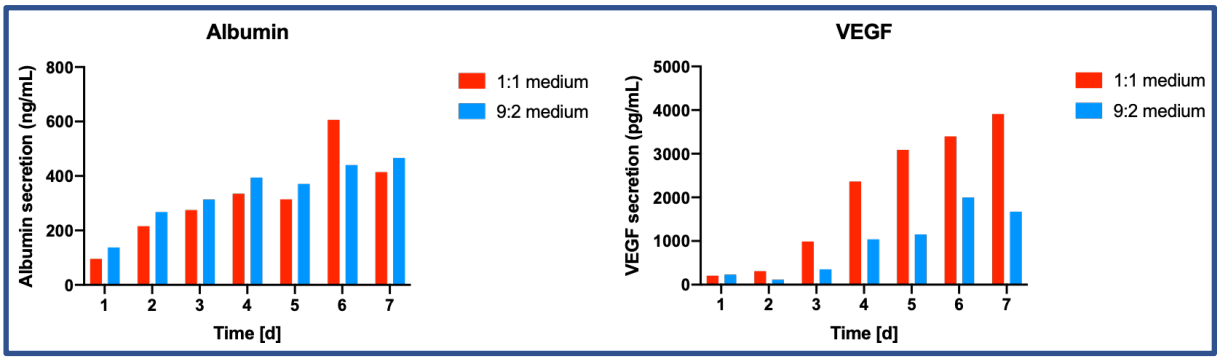

Figure 18. *Albumin and VEGF secretion measured through ELISA over the 7-day culture period in both medium conditions in agarose microwell arrays. Data are the mean value of one measurement per condition. Each measurement is the collected supernatant from one agarose well, containing 1500 independent spheroids.*

Considering all the above information, the HG-DMEM: EGM-2 1:1 ratio medium was selected as preferred medium over the 9:2 ratio for long term hepatic spheroid culture.

[1] https://promocell.com/wp-content/uploads/product-information/manual/C-22011.pdf

4.2.1.2. Cell type distribution

Subsequently to the HG-DMEM: EGM-2 1:1 ratio medium selection, the different cell types growth and distribution inside the tri-culture spheroids were investigated in order to gain more insight into the mechanisms cell localization and reorganization.

4.2.1.3. Cell cytometry

HepG2 were first stained with 705 Qtracker™ dye prior to spheroids formation with GFP-HUVEC and non-labeled LX2 cells. Cytometry data at day 0 of culture (Just before cell aggregation) revealed that the measured cell ratio was close to the theoretical one of 72% HepG2, 18% HUVEC and 9% LX2 (**Table 10**). Notably, from day 2 of culture HepG2 and GFP HUVEC detected signal displayed a dramatic decrease (**Figure 19**). In order to assess whether this trend was the cause of a sudden exponential LX2 number increase in the culture or it was due to a decrease in dye signal from HepG2, spheroids were stained with CellTracker™ probes and cell ratio and distribution was daily qualitatively studied by fluorescence microscopy.

Table 10. **Tri-culture hepatic spheroids cell ratio characterization through cytometry with Qtracker™ cell staining.** *Theoretical and measured HepG2, HUVEC and derived LX2 cell percentage at day 0 of hepatic spheroid tri-culture.*

Cell type	Ratio	Theoretical %	Measured %
HepG2	8	72.72	61.87
HUVEC	2	18.18	21.43
LX2	1	9.09	16.57

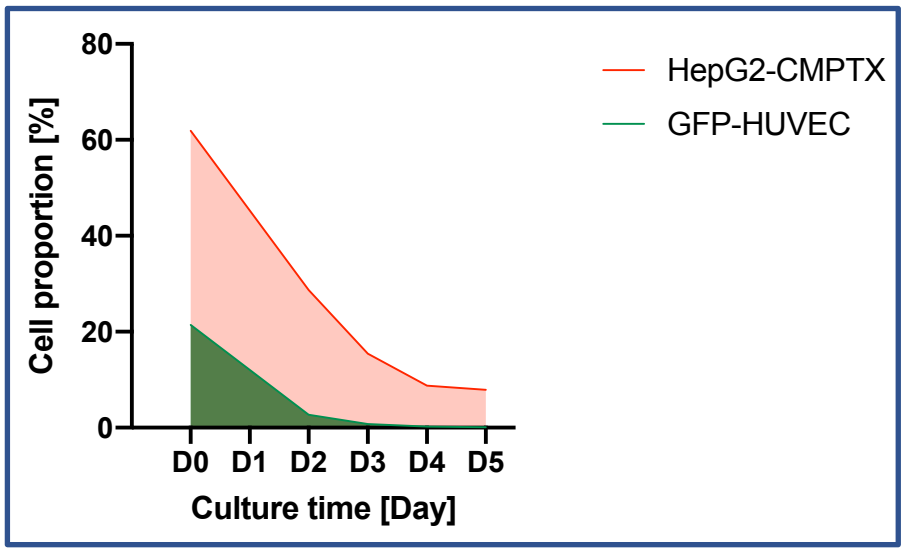

Figure 19. **Tri-culture hepatic spheroids cell ratio characterization through cytometry with Qtracker™ cell staining.** *Quantification of measured HepG2 and HUVEC percentage composition over the first 5 day of culture.*

Prior to qualitative the CellTracker™ staining, a second quantitative technique was adopted by labelling cells with immunofluorescence staining. Notably, only a small portion of the total initial cells (3,000 out of 270,000) did not get lost during the several washing steps required from the protocol, making the final estimation hard to interpret as reliable. Furthermore, strong cross-reactivity of the anti- α-SMA primary antibody with the other co-stained primary antibodies was detected, making the measurements unrealistic (**Table S2**).

4.2.1.4. Qualitative approach - CellTracker™ staining

Cells were fluorescently labelled with CellTracker™ probes prior to spheroids formation (HepG2 with red CMTPX and LX2 with blue CMAC) and their distribution in the agarose microwell arrays was analyzed over 6 days of culture.

The cytoplasmatic labelling, together with GFP signal, confirmed that within 24 hours of culture GFP-HUVEC tend to aggregate in the inner core, while LX2 formed an external capsule that surrounds the HepG2 (**Figure 20**). This micro-tissue complexity of hepatic stellate cells surrounding the tumor resembles a histopathological feature of hepatocellular carcinoma observed *in vivo* in patients [82, 83].

As shown in the microscopy pictures (**Figure 20**), daily evaluation of this aspect of tissue micro-complexity and cellular organization, despite displayed signal decrease of both CMAC and CMTPX, clearly confirmed the prevalence of HepG2 ratio, reinforcing the hypothesis that what observed during cytometry measurements for Qtracker™ staining was cause of intracellular dyes dilution due to cell proliferation.

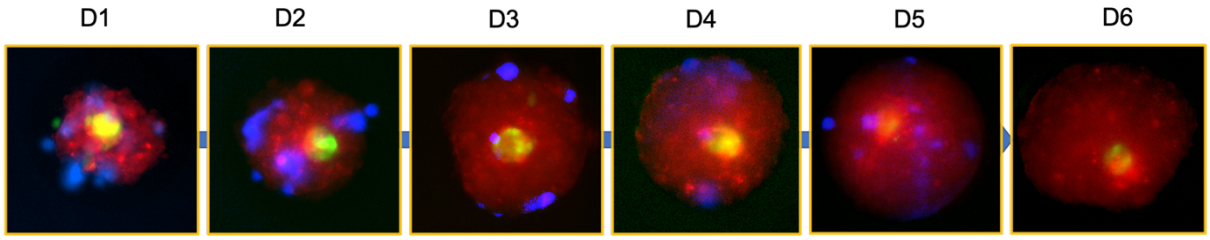

Figure 20. *CellTracker™ labelling characterization of hepatic tri-culture spheroids over 6 days of culture in agarose microwell arrays under a normal fluorescent microscope (EVOS). HepG2: red CMTPX, LX2: blue CMAC, GFP-HUVEC. Magnification is 10x.*

Overall, taking together the hepatic-spheroids characterization, day 4 of culture was considered as the best tradeoff between spheroid's viably (99.5%) and dimensions (150 µm) as well as cellular ratio maintenance (GFP-HUVEC core of 46 µm, LX2 outer capsule), together with significative metabolically activity (albumin and VEGF).

Therefore, day 4 of culture were chosen as starting day for spheroids GelMA encapsulation (**Figure 21**).

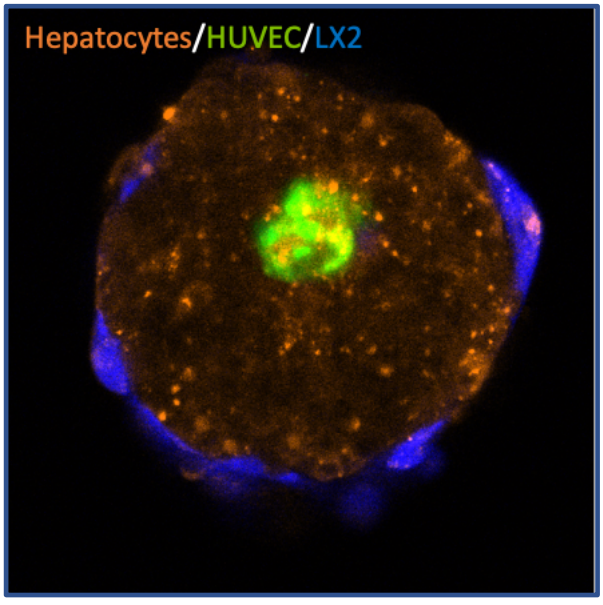

Figure 21. *Representative confocal picture of hepatic tri-culture spheroids at day 4 of incubation in 1:1 medium composition. Image indicates GFP HUVEC (green), HepG2 (red CMTPX) and LX2 (blue CMAC). Magnification is 20x.*

4.2.1.5. Spheroids characterization before GelMA encapsulation

In order to better characterize the cellular contribution before GelMA encapsulation, hepatic-spheroids at day 4 of culture were further studied.

Protein expression was characterized through immunostaining, followed by z-stack examination with confocal microscopy. The proteins of interest were related to cell-specific markers: albumin for HepG2, α-SMA for LX2, CD31 for HUVEC (**Figure S3**), and collagen I and III as specific ECM key component in healthy and pathological liver.

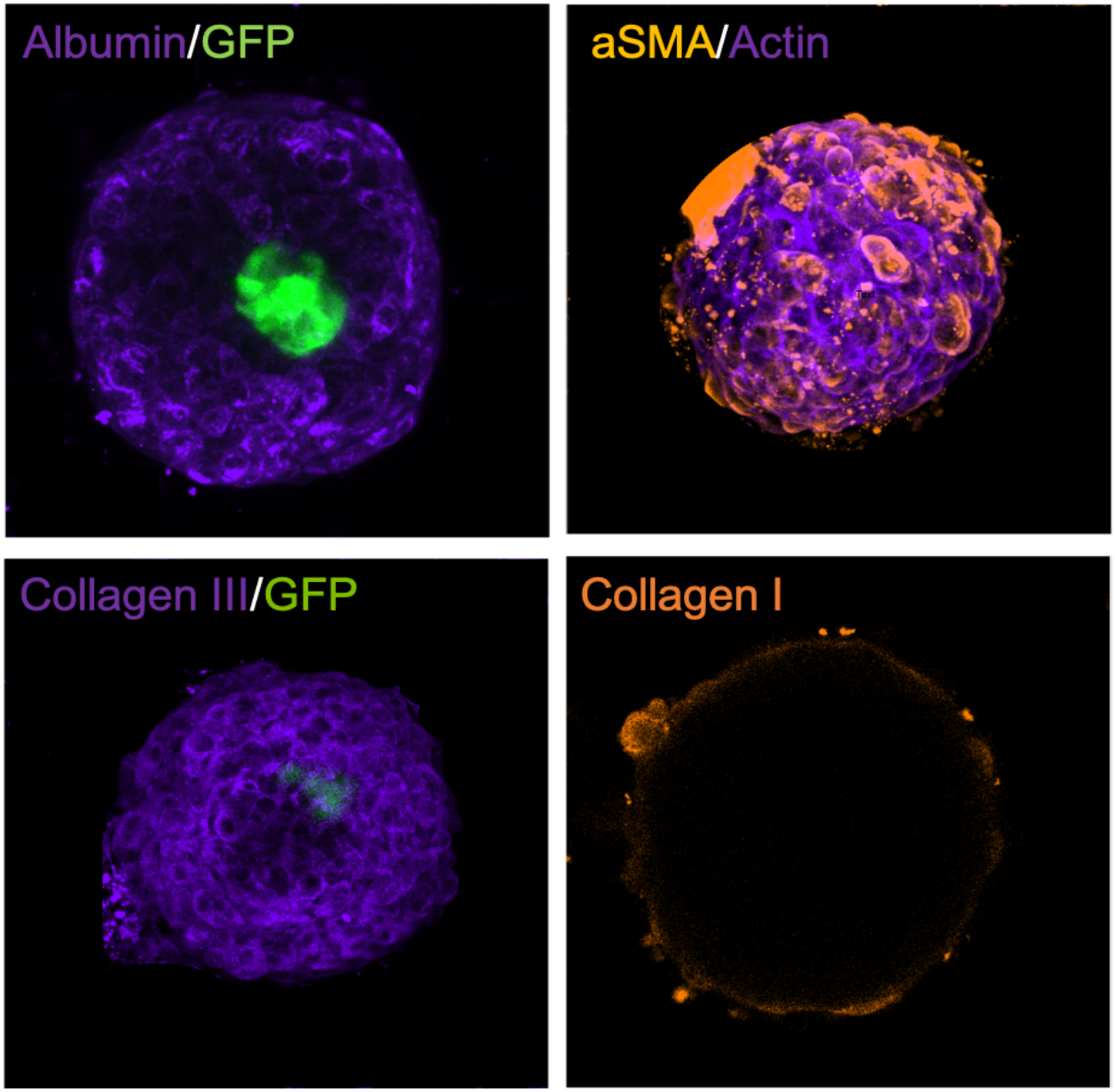

Figure 22. *Representative immunofluorescent analysis of hepatic tri-culture spheroids at day 4 of culture for albumin (violet), GFP-HUVEC (green), α-SMA (orange), actin (violet), collagen III (violet) and collagen I (orange), as indicated above. Images are maximum projections of confocal z-stacks (120 μm stack, 4 μm steps). Magnification is 20x.*

As reported in **Figure 22** the immunostaining of harvested spheroids at day 4 of culture in the 1:1 tri-culture medium confirmed the cell distribution observed with the CellTacker™ staining. Particularly, α-SMA expression confirmed the LX2 presence in the outer ring of the spheroids surrounding the hepatocytes spherical-like shell, suggesting once again the presence of different metabolic areas within the same spheroid. Collagen III immunostaining from the equatorial plane to the bottom of the spheroids allowed the visualization of the collagen fibers forming the capsule of the ECM. Notably, collagen type I staining resulted to be negative throughout the entire spheroids, suggesting a lower production of this type of collagen over type III.

4.3. Static multi-culture GelMA hydrogels

In light of the above, hepatic multi-culture GelMA hydrogels were established by encapsulating 500 hepatic tri-culture spheroids cultivated for 4 days in the 1:1 tri-culture medium in the three physiological-like GelMA concentrations (5%, 9%, 12% (w/v)) together with further single GFP-HUVEC and PMA-activated THP1 cells, in a 1:1 ratio. This in order to investigate at a microscopical and molecular level the mechanosensitive cellular behavior over such a range of stiffness.

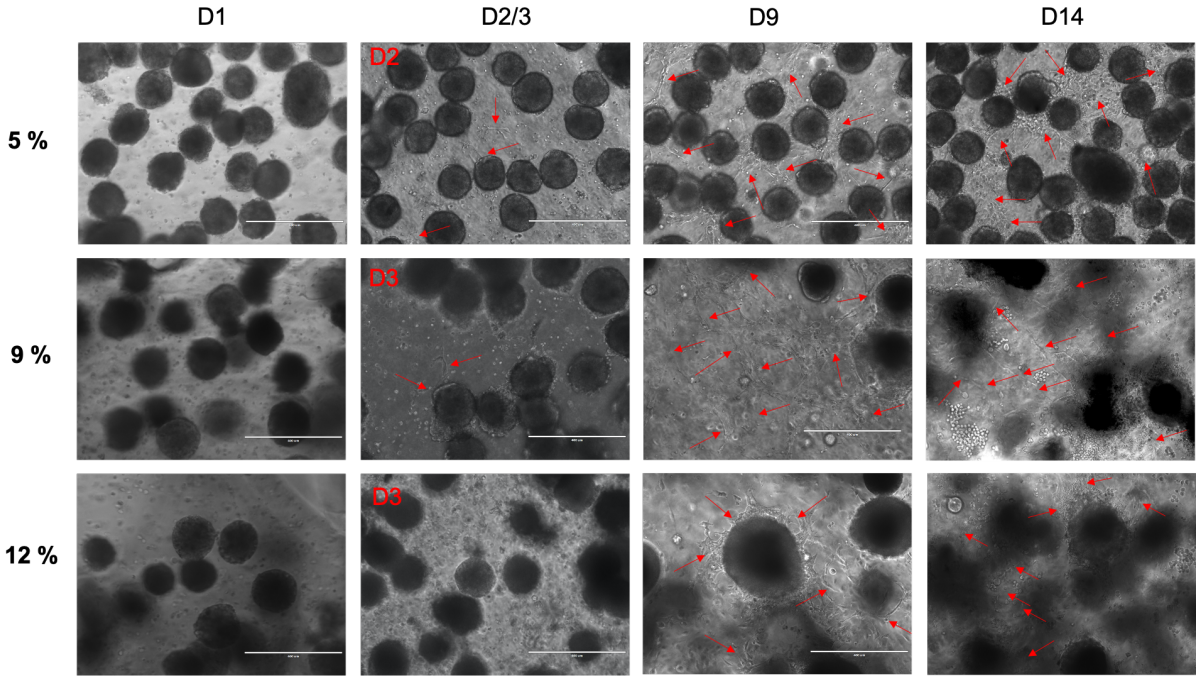

Figure 23. *Representative bright field microscopy images of static culture conditions made of 500 hepatic tri-culture spheroids, single GFP-HUVEC, THP1 cells embedded into 5%, 9% and 12% (w/v) GelMA hydrogels. Images show resulting morphology and cell migration at indicated days of incubation (D1 to D14) in the three GelMA hydrogel conditions. Arrows indicate cellular branching. Magnification is 10x.*

Preliminary analyses of cell growth and behavior under bright field microscopy, revealed that spheroids encapsulated in 5% GelMA hydrogels started featuring cell branches from their outer layer towards the ECM space within 48 hours from cell encapsulation. A similar behavior was observed after further 24 hours also in the 9% GelMA hydrogels (**Figure 23**). In 12% GelMA hydrogels, a peculiar behavior was observed only after 5-6 days from cell encapsulation (data not shown). Such behavior increased progressively over 14 days of culture, forming a dense network of migratory cells, connecting together the neighboring spheroids. (**Figure 23**)

Concurrent with this, from day 7 of culture the accumulation of "bubble-like" clusters with an average diameter of 10-15 µm both entrapped in the ECM among spheroids and released in the supernatant was observed, suggesting the production of extracellular vesicles from the hepatic-spheroids. (**Figure S4**)

4.3.1. **Protein localization**

As shown in **Figure 24** the α-SMA immunofluorescent staining of 5%, 9% and 12% GelMA hydrogels at day 14 of static culture, confirmed the hypothesis that LX2 expressed their migratory phenotype, proliferating and stretching along the matrix. HSCs in 5% GelMA stretched out in a more elongated aspect (**Figure 24A**), creating an interconnected network connecting the neighboring spheroids, as observed with bright field microscopy. On the contrary, LX2 encapsulated in 9% GelMA migrated out of the spheroids (**Figure 24B**), creating a denser mesh of single cells in the matrix, and surrounding the spheroids. In 12% GelMA hydrogels, it was observed that (**Figure 24C**) HSCs migration occurred only in proximity of hydrogels' surface and that inner spheroids remained well-compacted and with no signs of cell elongation and inter-spheroid communication, suggesting the presence of a caging conditions of hepatic-spheroids inside hydrogel's matrix. Notably, LX2-CMAC and GFP-HUVEC signal was weakly detected in the ECM mesh for all the three GelMA concentration hydrogels (**Figure 24**).

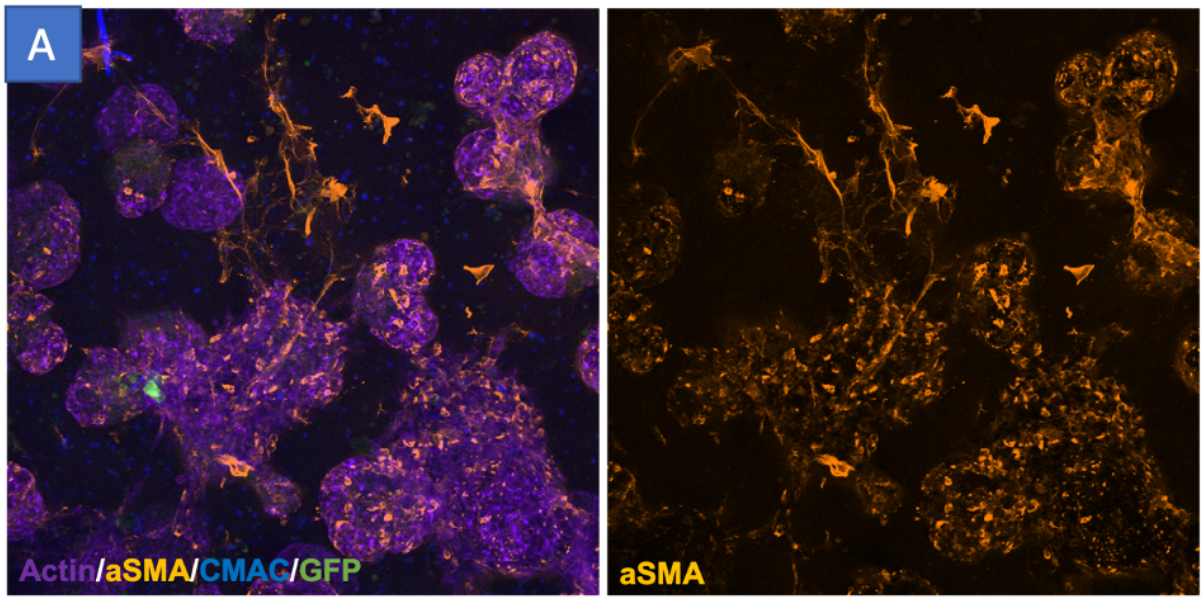

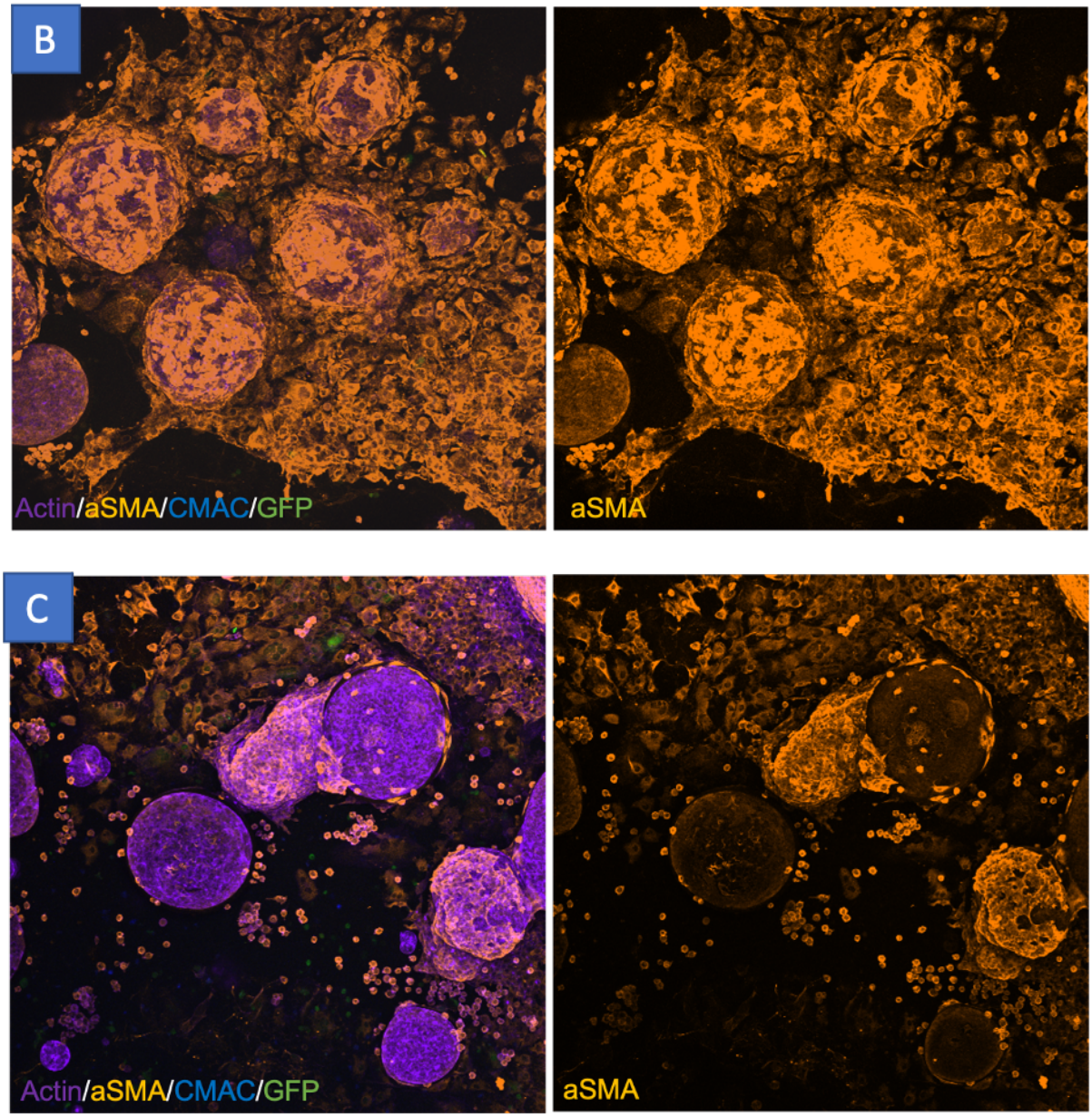

Figure 24. Representative immunofluorescent analysis of the static hepatic multi-culture in the three GelMA hydrogel conditions ((A)5%, (B) 9%, (C) 12% (w/v)) at day 14 of incubation. Images are maximum projection of confocal z-stacks and indicate actin (violet), THP1 (blue CMAC), HUVEC (GFP, green) and α-SMA (orange) localization within the hydrogels. Magnification is 10x.

4.3.2. **HUVEC growth and distribution**

Concurrent with spheroids analyses, single GFP-HUVEC growth and distribution inside the three GelMA hydrogel conditions was analyzed over the same period of culture. Notably, microscopical analyses revealed that (**Figure 25**) GFP-HUVEC did not spread in the GelMA network over time, maintaining a spheroidal shape. Further, such GFP signal drastically decreased overall overtime with an inversely proportional trends with respect to hydrogel concentrations.

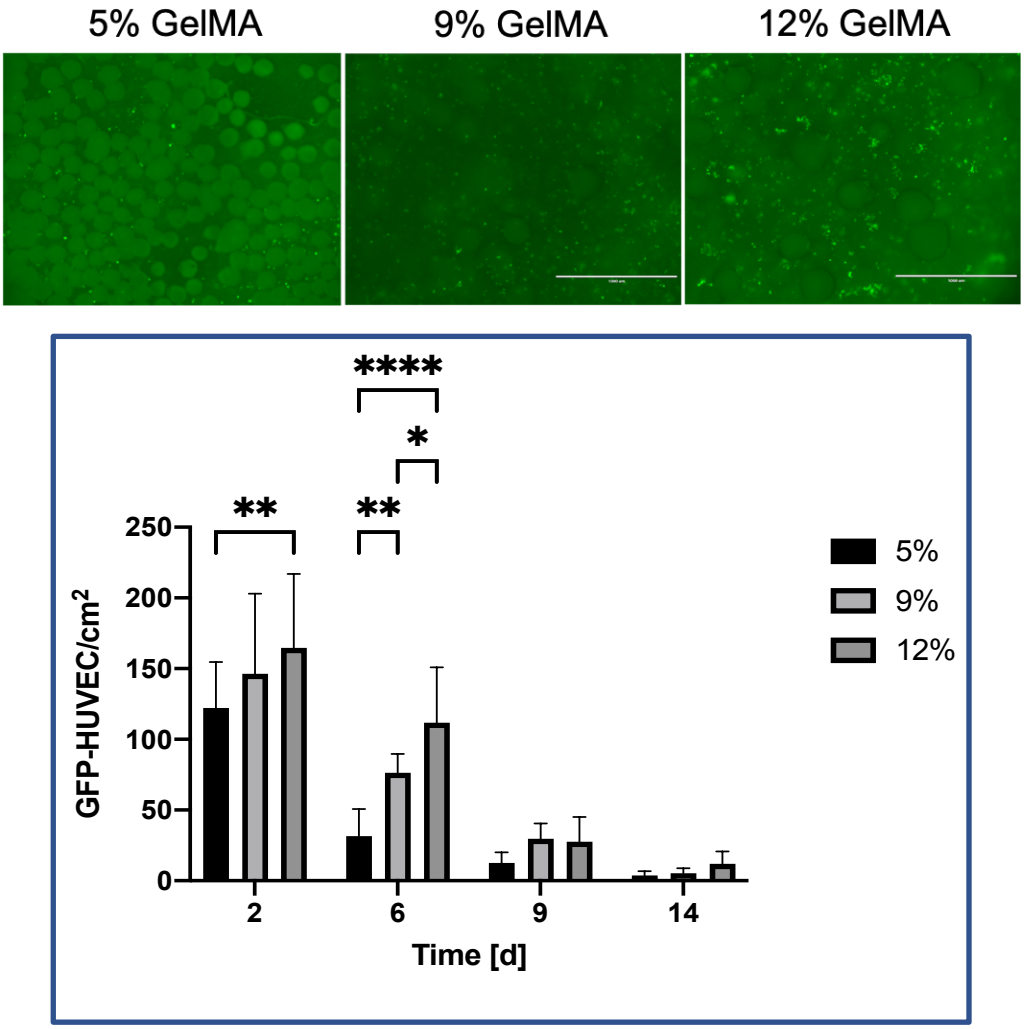

Figure 25. *GFP-HUVEC presence in GelMA hydrogels.* ***(Top)*** *Representative GFP-HUVEC distribution into 5%, 9%, 12% (w/v) hepatic multi-culture GelMA hydrogels at day 6 of culture. Magnification 4x.* ***(Bottom graph)*** *Determination of GFP-HUVEC density, defined as the number of GFP signal per given area. Overall, density drastically decreased over time, with a significant trend proportional to the hydrogel percentage (*p<0.05, **p<0.01, ****p<0.0001). Data are the mean value ± SD, n=9.*

4.3.3. **THP1 distribution**

From the microscopical analyses (**Figure S5**), no difference in THP1 distribution were observed in the three GelMA condition hydrogels. At Day 14, groups of THP1 seemed to invaded spheroids outer layers in some regions of the 5% and 9% (w/v) hydrogels (**Figure 26**). However, a more in-depth investigation over this behavior was not conducted due to weakness of blue CMAC signal.

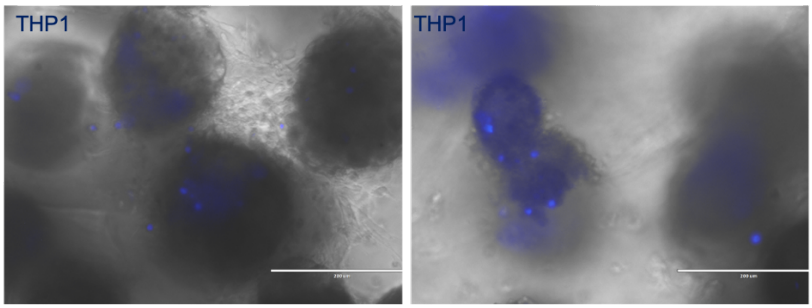

Figure 26. *Representative picture of THP1 cells (blue CMAC) embedded in 5% (left) and 9% (right) hepatic multi-culture GelMA hydrogel at day 14 of incubation. DAPI channel - Bright field picture overlay. Magnification 20x.*

4.3.4. **Viability**

At day 14 of culture the Live/Dead staining displayed (**Figure 27**) a high Calcein-AM signal and a lower Propidium Iodide one, suggesting the maintenance of a high cell viability in all the three GelMA concentrations over time.

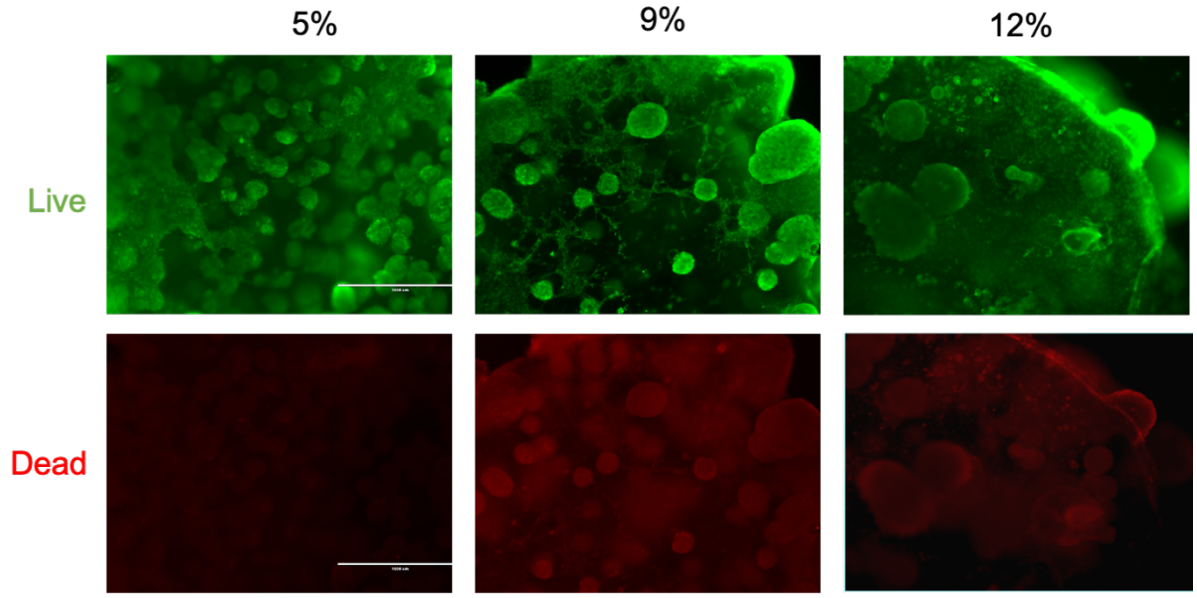

Figure 27. *Hepatic multi-culture GelMA hydrogels live-dead staining cell viability and characterization. Representative figure of live-dead staining of 5%, 9%, 12% (w/v) hepatic multi-culture GelMA hydrogels at day 14 of culture. Green (live, Calcein-AM)), red (dead, ethidium homodimer).*

4.3.5. **Molecular analysis**

Based on the previous observations, the effects of GelMA hydrogels on cells fate were further examined evaluating gene and protein expression using qPCR and ELISA approaches, respectively.

4.3.5.1. qPCR

In order to better quantify at molecular level, the expression of different pro fibrotic markers and the relative up- and downregulation in their culture environments, qPCR analyses were performed for all the three GelMA percentage conditions on 14 fibrosis-related genes at day 0 and 14 of culture and the obtained ratio (D14/D0) was studied.

Despite the existence of a rather high variance among repetitions and between the two different biological rounds, it was possible to identify the relative trends of the level of the transcript of each gene as a function of the three GelMA conditions (**Figure 28**).

Notably, 5% and 9% GelMA hydrogels showed overall higher level of transcripts of pro-fibrotic gene markers, such as *α-SMA*, *TGF-β* and *VEGF* suggesting that, in these two conditions, cells - especially HSCs - acquire an activated pathological phenotype, compared to the 12% GelMA culture condition. Additionally, 9 % GelMA hydrogels, although not significantly, displayed an overall higher level of the gene activity concerning additional key pro-fibrotic markers compared to 5% condition, such as the activated-MFs related genes (*PDGFβ, Col3*), hepatocytes activity (*albumin*) and pro-fibrotic crosstalk (*CXCL10*) and pro-inflammatory related genes (*TNF-α*, *CD64*). On the other hand, 5% GelMA hydrogels displayed a slightly higher, but not significant, upregulation of the transcription of the pro-inflammatory gene *CXCL8* compared to the 9% condition.

Notably, the transcription of two matrix-remodeling genes, *MMP9* and *Col1*, showed a strong downregulation in all the three GelMA conditions, more marked in 5% GelMA and less marked in 9% GelMA hydrogels. Additionally, the monocytes chemoattractant *CCL2* related gene displayed a notable downregulation in all the three concentration and proportional to GelMA concentration. Finally, the pro-inflammatory, M1 macrophage marker *CD319* related gene displayed an overall overexpression in all three GelMA hydrogel concentration. However, its high C_q cycle number (over 37) made its interpretation unreliable.

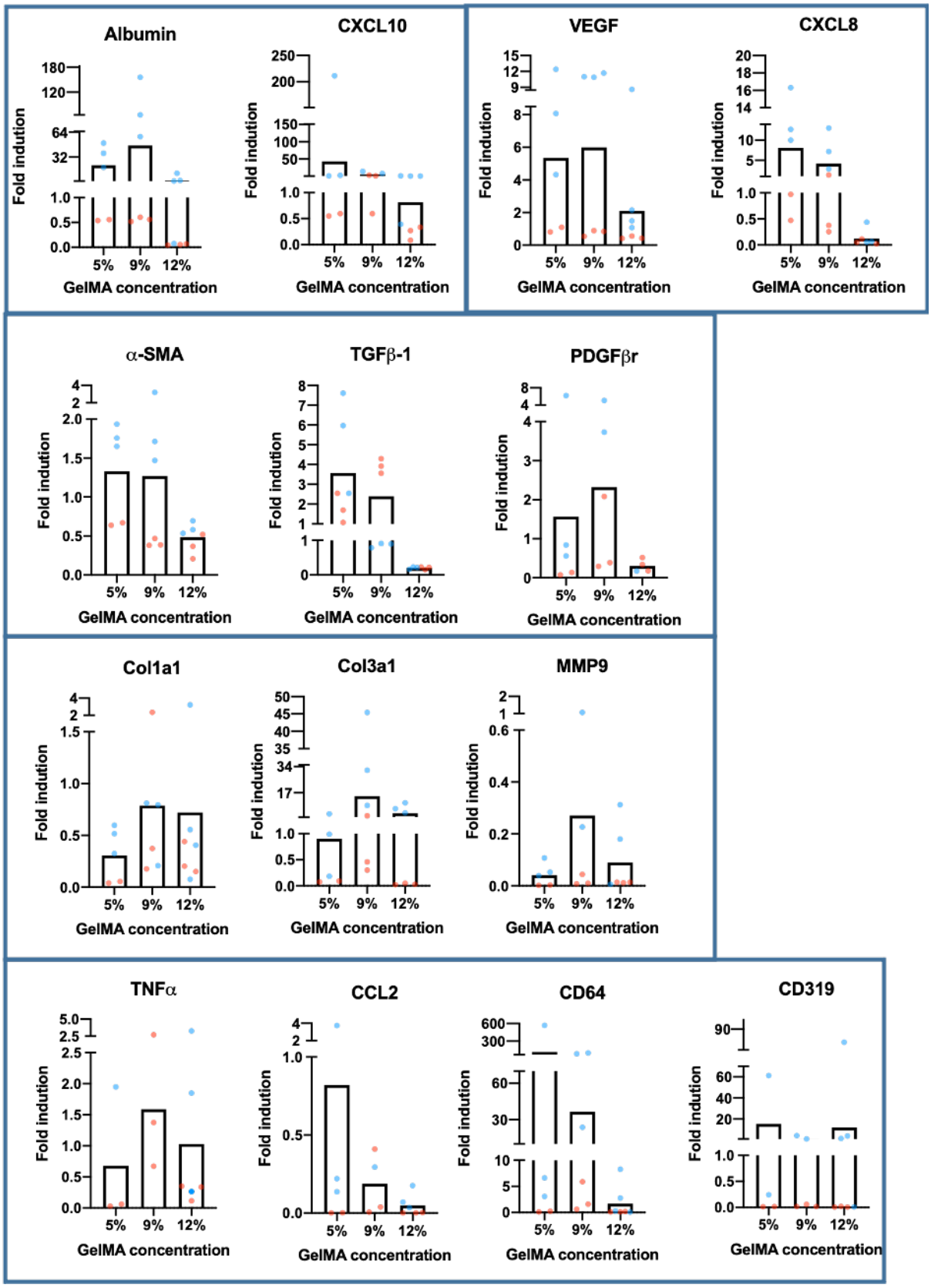

Figure 28. *Gene expression comparison between hepatic multi-culture 5%, 9%, 12% (w/v) GelMA hydrogel at day 14 of culture. Each value is the ratio between day 14-fold induction and day 0 average fold induction for the same condition, upon GAPDH normalization. Data are from two individual experiments (blue dots: I round, red dots: II round). NOTE: although not shown, a statistical significance was found between 5% and 12% GelMA hydrogels for TGF-β (*p<0.05).*

4.3.5.2. ELISA

In order to further characterize the pro-fibrotic profile of each hepatic multi-culture GelMA hydrogel over time, the regulation of four pro-fibrotic proteins and cytokines were analyzed by studying their secretion through ELISA assays.

Cells in the 3D static platforms showed an increase in albumin and VEGF secretion in all the three GelMA ratio between day 1 and day 9 of culture (**Figure 29, Table S3**) This suggests that the cells proliferated and grew over the period of culture without distinction among the three GelMA percentages. Between day 9 and day 14 of culture the trend stabilized, displaying a non-significant difference in albumin and VEGF secretion during the second period of culture. No statistical significance was detected (**Table S3**) among the three GelMA hydrogel concentration cultures at the same day of incubation (day 1, day 9, day 14).

The secretion of TNF-*α* and IL-6 showed a rapid increase between day 1 and 9 of culture in all the three GelMA percentages, with an average, but not statistically different, lower values proportional to GelMA percentages for TNF-*α*. However, during the second half of culture period, the amount of both markers secreted displayed a decreasing trend, except for TNF-*α* in 9% GelMA hydrogels. However, the notably high variance among repetitions for IL-6 made the evaluation of its trend hard to interpret. Notably, 9% GelMA showed to maintain a relative quite high values of both TNF-*α* and IL-6 in the second period of culture compared to the other two GelMA percentages, suggesting the potential presence of a more marked pro-inflammatory/fibrotic environment.

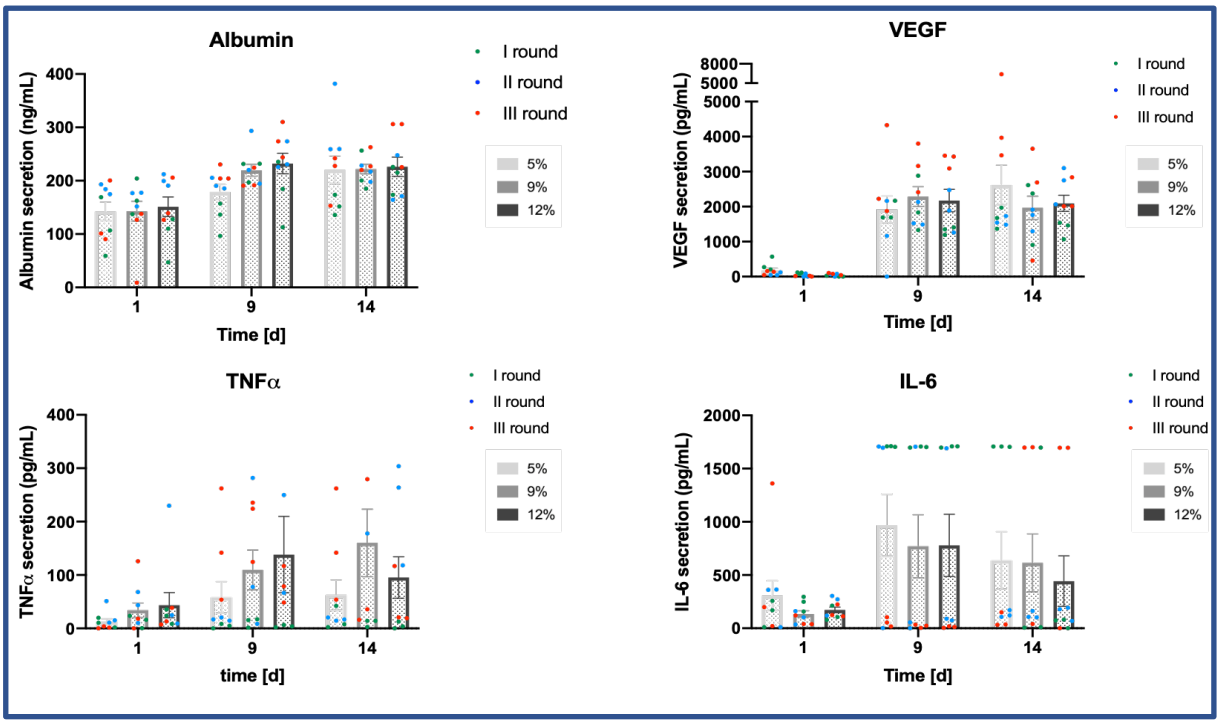

Figure 29. *Protein secretion detected by ELISA. Comparison between hepatic multi-culture 5%, 9%, 12% (w/v) GelMA hydrogel at day 1, 9, 14 of culture. Data are from three individual experiments, 3 measurements per experiment. (green dots: I round, blue dots: II round, red dots: III round). Data are the mean value ± SEM, n=9.*

4.3.5.3. NO release assay

Similar analyses were performed to assess the secretion of nitritic oxide (NO) from cells exposed to the three GelMA concentrations at the same days of culture. Results concerning the NO release assay

(**Figure 30**) showed null relative secretion values throughout the entire period of culture in all the three GelMA conditions.

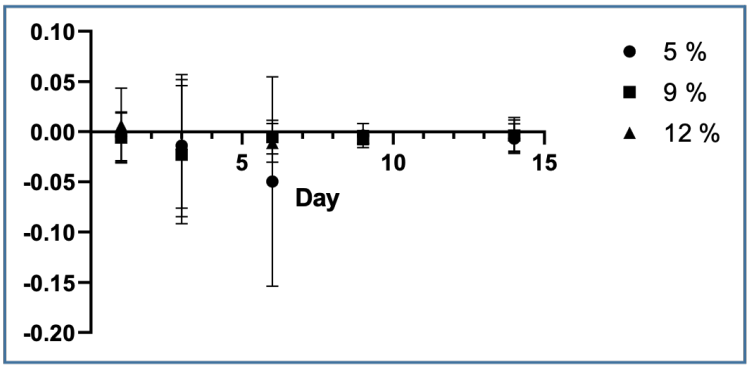

Figure 30. *Nitric oxide (NO) secretion determination in hepatic multi-culture 5%, 9%, 12% (w/v) GelMA hydrogels at day 1, 6, 9 and 14 of culture. Data are shown as the relative absorbance value (A.U., 450 nm) measured by normalizing each value with the cell culture medium's absorbance (blank) measured at the same time point. Data are the mean value ± SD, n=9.*

4.4. Microfluidic chip

The liver on a chip system (See *paragraph 2.6.4.*) were characterized in terms of interstitial fluid flow velocity and distribution and pressure profile within the device. Preliminarily, a computational approach was adopted in order to assess the theoretical above-mentioned parameters in the design and subsequently the obtained values were experimentally assessed. The possibility to obtain a confluent endothelial layer was also explored and optimized in the presence of immune cells.

4.4.1. **Initial chip design**

4.4.1.1. COMSOL simulations

The fluid dynamics of the chip was analyzed using the flow simulation software COMSOL Multiphysics, as previously described in the *Material and Methods* section. In the model, the applied inlet and outlet rates (12.7 µL/min and 12.3 µL/min (3x4.1 µL/min), respectively) exert a pressure difference between the central medium channels and the supernatant channels. This generated an average fluid flow volume through the hydrogel pockets of 0.4 µL/min, together with a physiological relevant shear stress value of 2.5 dyn/cm^2 at the walls of the central channels. According to the results of the simulation (**Figure 31**), the generated interstitial fluid flow velocity profile in the hydrogel pockets has a symmetrical distribution, displaying higher values at the narrow fenestrations between the pillars and at the external lateral part of the pockets (about 4.0 µL/min). The fluid distribution at the supernatant channels displays higher values in the segments interfacing the hydrogel pocket (about 4.0 µL/min), while lower-to-null velocity in the loop-like structure.

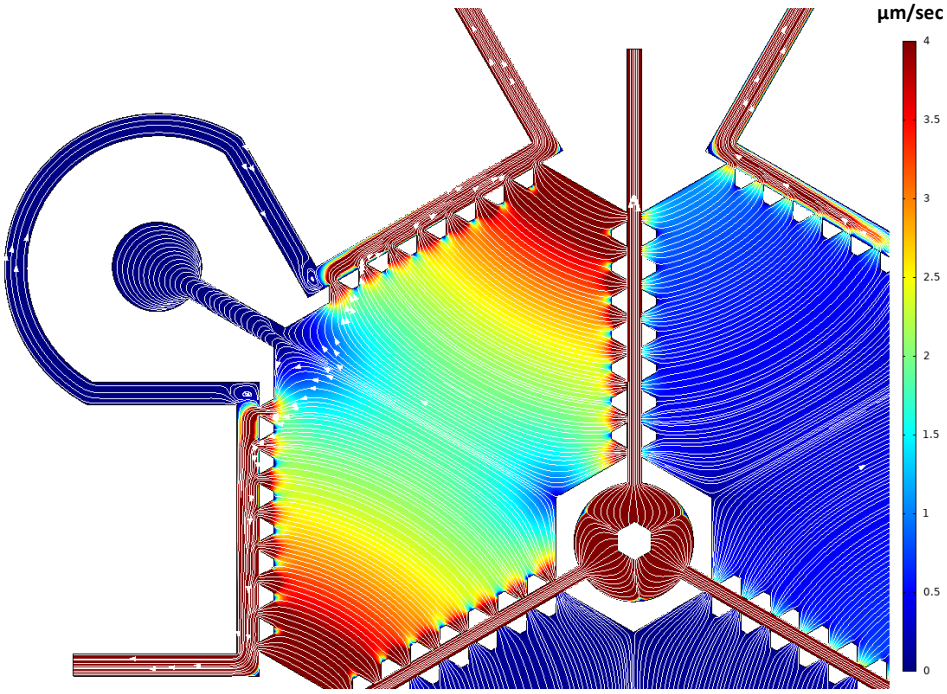

Figure 31. *Representative COMSOL topographical fluid flow velocity distribution in the first liver lobule on a chip design for 5% (w/v) GelMA chamber, medium and supernatant channels when an interstitial fluid flow of 0.4 µL/min is applied.*

4.4.1.2. Experimental assessment

Based on these theoretical results, several chip runs were experimentally tested to assess the best interstitial fluid pressure to apply in such device in order to obtain a physiological relevant interstitial fluid flow with supernatant accumulation at the outlets of the supernatant channel in all the three hydrogel pockets. Interstitial flow velocities ranging from 0.4 µL/min to 4.0 µL/min, obtained by changing the outlet fluid rates, were tested for 20 hours of run. The chips were qualitatively assessed in term of GelMA swelling and supernatant collection. As reported **Table S4**, for interstitial flow velocities in the range 0.4- 2.0 µL/min, after 20 h no supernatant was collected in any of the three channels. For values above 2.3 µL/min supernatant was collected in all the three channels, but with notably high variance between each repetition. Microscopical assessments of the chips after 20 h of perfusion revealed a significative GelMA swelling in every hydrogel pocket and proportional to GelMA concentration, as previously reported [84]. The swelling caused hydrogel extravasation in the medium and supernatant channels through the fenestrations between the pillars (**Figure 32**). This significantly reduced the working diameters of the channels and changed resistance of the flow between inlet and outlet and central and supernatant channel. Further, interstitial flow velocities above 3.0 µL/min caused 5% GelMA disruptions and detachment from the PDMS walls of the pockets (**Figure 32**).
Furthermore, when endothelialized, the supernatant channels showed the formation of significant necrotic areas at the interface with GelMA hydrogels and in the loop-like structures (**Figure 33**), in accordance with COMSOL simulations.

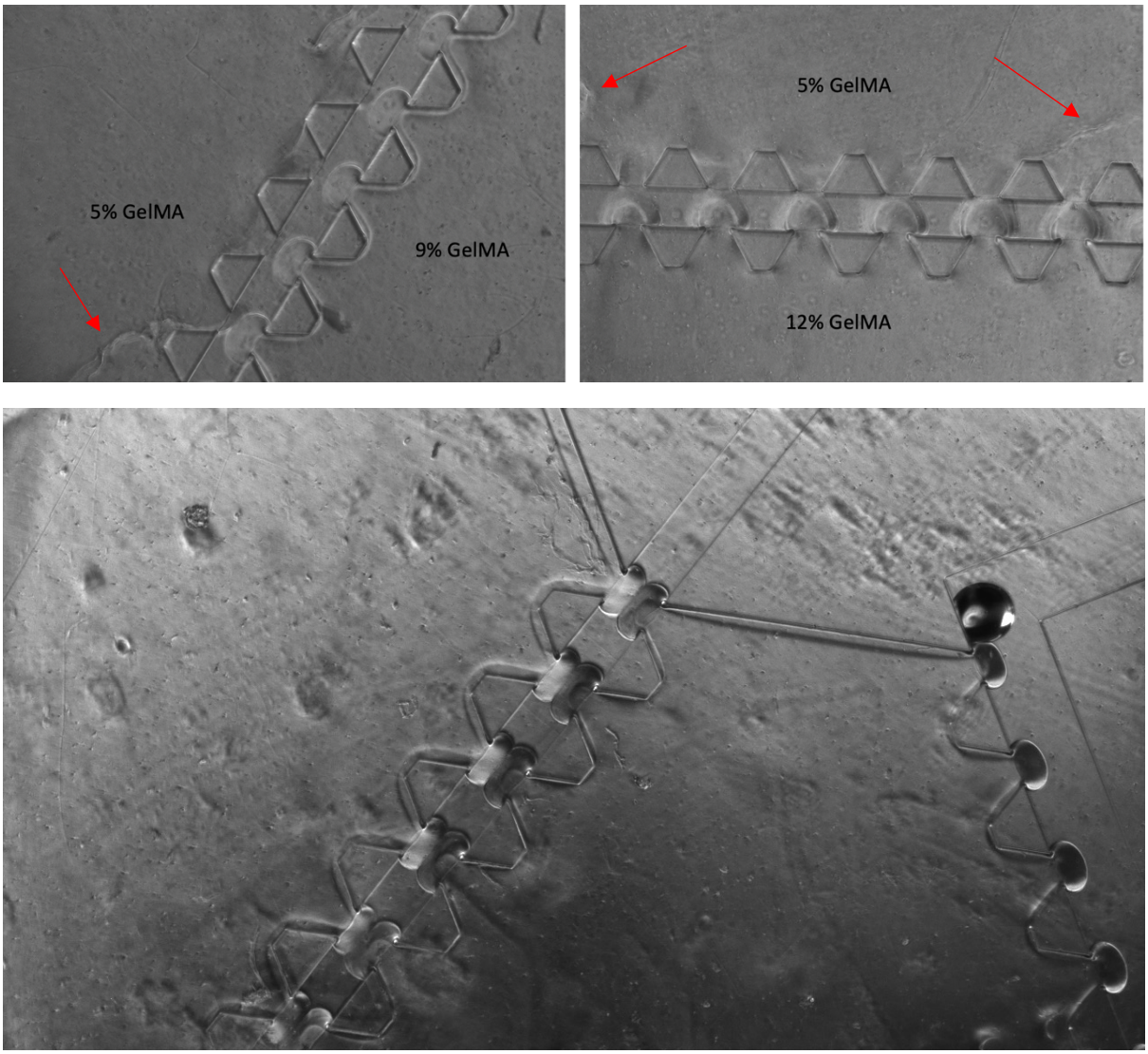

Figure 32. *Representative pictures of GelMA hydrogels aspects in the first liver lobule on a chip design after 20 hours of perfusion.* ***(Top pictures)*** *Medium channel obstruction due to 9% and 12% (w/v) GelMA hydrogels extravasation and 5% GelMA detachment (arrows). Magnification is 4x.* ***(Bottom picture)*** *central medium channel complete clogging, Magnification is 2x.*

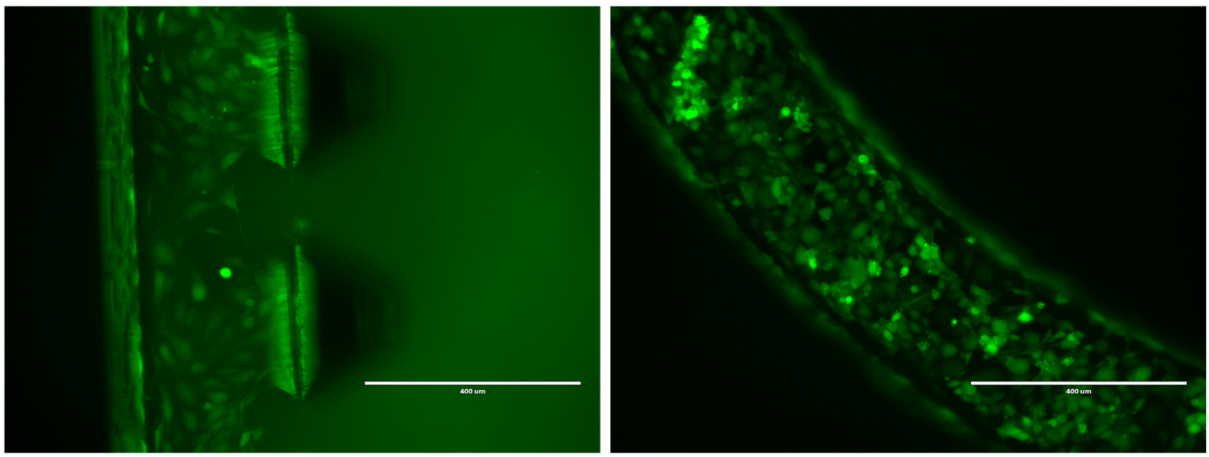

Figure 33. *GFP-HUVEC endothelialization of supernatant channels in the first liver lobule on a chip design at the hydrogel's interface (left) and in the loop-like structure (right) after 24 hours of incubation. Magnification is 10x.*

4.4.2. **Second chip design**

In light of these limitations, a second liver lobule on a chip was designed with the aim of reducing the number of variables that come into play during chip runs, in favor of a greater control over fluid flow distribution.

Specifically, the channel diameters were increased from 200 µm and 300 µm for the medium and supernatant channels, respectively, to 600 µm in order to limit the influence of GelMA swelling on channels clogging. Together with this, the distances of the inlet and outlet channels from the GelMA pockets were increased to limit the potential risks of disturbing the GelMA hydrogels creating additional hydrostatic pressure and further GelMA dislocation during needles or pipettes insertion.

The loop-like structure in the supernatant channels were removed and hydrogel inlets moved to one side of the pockets, in order to reduce as much as possible the formation of potential necrotic areas due to drops in interstitial fluid flow velocity.

Moreover, in order to further reduce the number of variables that come into play during microfluidic chip runs (*i.e.*, syringe pumps hydraulic resistance, uncontrollable pressure drops) the withdrawing pressure exerted by the three outlet syringe pumps were set at 0, by blocking the medium outlet, and the theoretical interstitial fluid velocity value was directly injected in the medium inlet, creating a more controllable interstitial fluid flow.

4.4.2.1. COMSOL simulations

The pressure distribution profile obtained by applying an inlet fluid rate of 0.3321 µL/min resulted independent from the hydrogels permeability, displaying an equal profile in all the three hydrogel pockets (**Figure 34**). Specifically, it linearly decreased from a maximum of about 90 Pa at the interface with the central channels, to a minimum of about 30 Pa at the interface with the supernatant channels.

As also shown in the previous design, the topographical interstitial fluid flow velocity distributions obtained with COMSOL simulation displayed a similar profile among the different pockets, but with significant difference of values and supernatant collection, directly dependent and proportional to hydrogel permeability (**Figure 35, Table 11**).

Furthermore, as a proof of concept, a COMSOL simulation was performed also under the condition of open (positive withdrawing) channel outlets, showing the generation of a wall shear stress at the central channel of 0.34 dyn/cm^2 when the same interstitial fluid flow of 0.3321 µL/min was generated (**Figure S6, Table S5**).

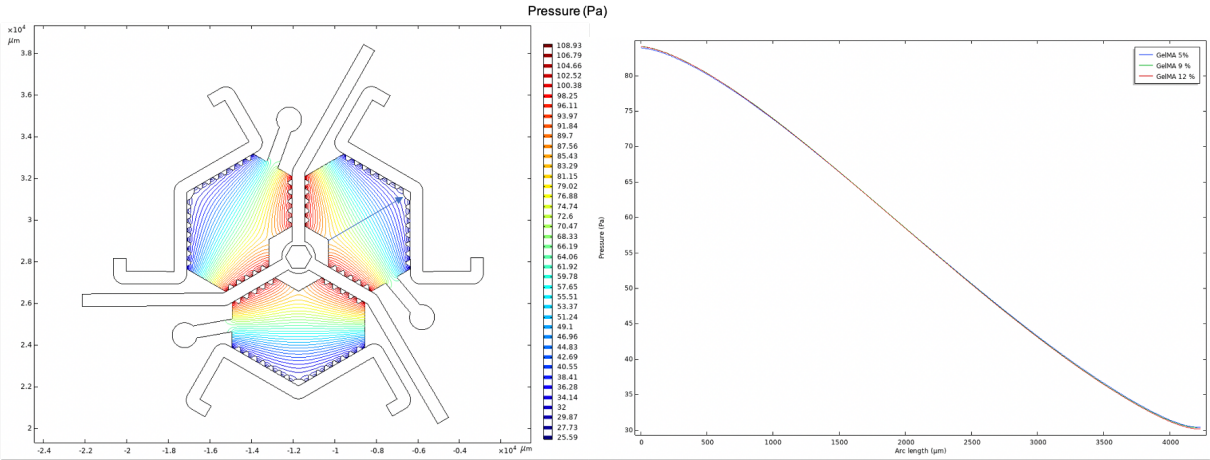

Figure 34. *COMSOL topographical pressure distribution in the second liver lobule on a chip design hydrogel chambers when 5%, 9%, 12% (w/v) GelMA hydrogel are loaded (left). The graph (right) represents the pressure values measured throughout the entire pockets' length in the blue arrow direction.*

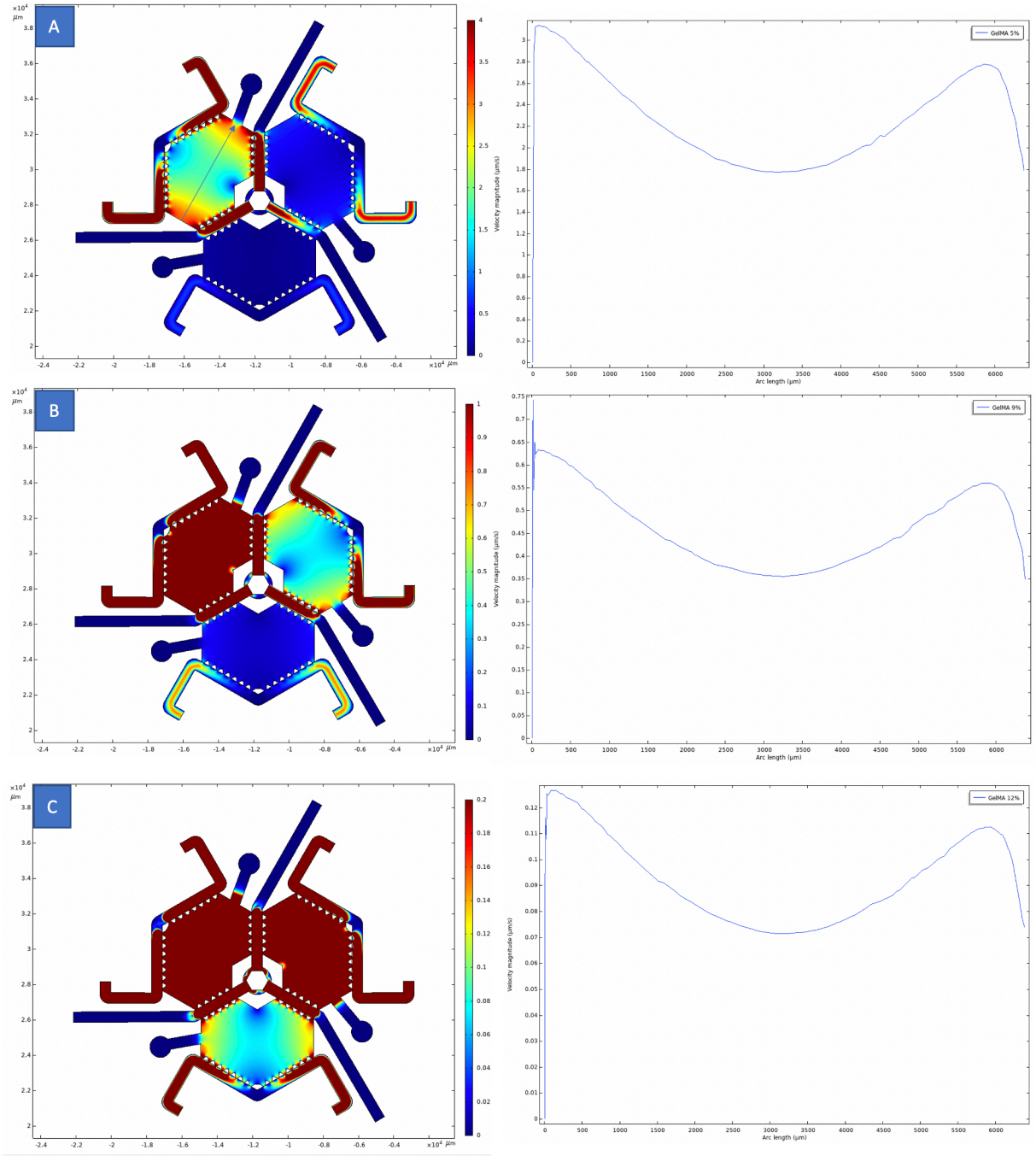

Figure 35. *COMSOL topographical fluid flow velocity distribution in in the second liver lobule on a chip design for 5% (A), 9% (B), 12% (C) (w/v) GelMA hydrogel chamber, medium and supernatant channels when an interstitial fluid flow of 0.3321 µL/min is applied (data are in µL/min). The graphs (right) represent the fluid flow velocity values measured throughout the entire pockets' length in the blue arrow's direction.*

Table 11. *COMSOL calculation of supernatant collection in µL/min and mL/day at the three supernatant channels when an interstitial fluid flow of 0.3321 µL/min is applied in the second liver lobule on a chip design.*

	µL/min	mL/day
Medium Inlet Total	0.3321	0.4782
Supernatant Outlet - 1 (GelMA 5%)	0.2635	0.3794
Supernatant Outlet - 2 (GelMA 9%)	0.0576	0.0829
Supernatant Outlet - 3 (GelMA 12%)	0.0111	0.159

4.4.2.2. Experimental assessment

4.4.2.2.1. Endothelialization

Following the endothelialization protocol, as shown in **Figure 36A**, a confluent HUVEC coverage of the supernatant channels within one day of dynamic (gravity-driven flow) culture was obtained. Cells readily adhered to the walls of the supernatant channel, created a confluent monolayer, and elongated along the shear stress direction, without evidencing the presence of necrotic areas**.** Furthermore, as shown in the 3D confocal reconstruction (**Figure 36C**) cells covered the entire circumference of the channels. Pretreated PMA-THP1 cells seeded after 24 hours of culture on both sides of the supernatant channels successfully attached to the HUVEC monolayer (**Figure 36B**) forming clusters of monocytes, as previously reported [58]. No further changes in endothelial morphology were observed after four days of cultivation.

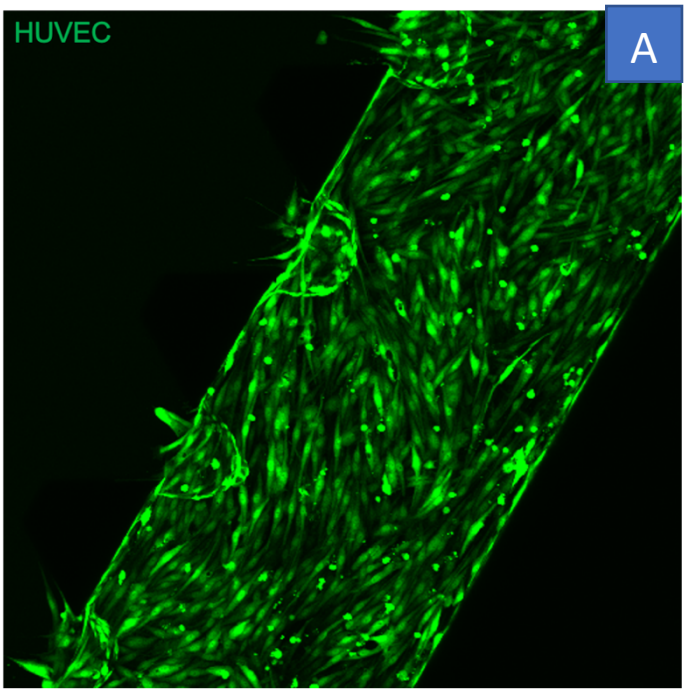

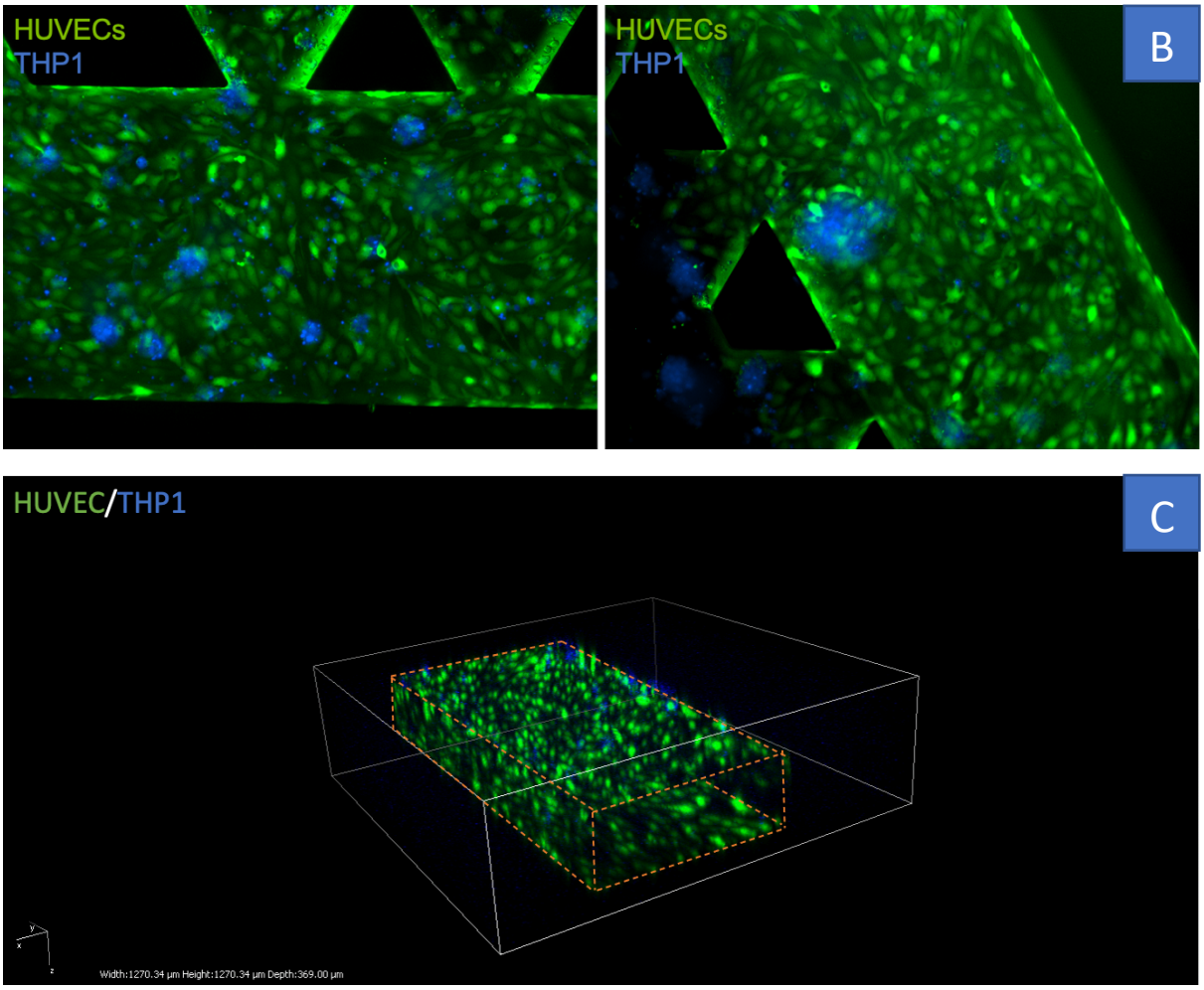

Figure 36. *Liver lobule on a chip endothelialization in the second liver lobule on a chip design. (A) Representative confocal picture of supernatant channel endothelialization at day 3 of culture.Magnification is 10x. (B) Representative EVOS pictures of endothelialized supernatant channels after 24 hours of THP1 cells seeding. Magnification is 10x. (C) Volumetric confocal reconstruction using z-stacks of endothelialized supernatant channels in the presence of THP1 cells at day 4 of incubation. Magnification is 10x.*

4.4.2.2.2. Experiential trails

Microfluidic experiments under 0.3221 µL/min inlet rate (closed outlets condition) and in the presence of the three GelMA concentrations, after 20 hours of run, displayed overall significant lower channel obstructions due to GelMA swelling (**Figure 37**). However, although no GelMA disruptions occurred, the supernatant levels measured in the three channels differed, ranging from over 1 mL at the 5% GelMA compartment to 0 µL at the 12% GelMA compartment (data not shown).

In light of this, in order to further reduce the functional complexity of the system, the microfluidic platform was tested by encapsulating the same GelMA concentration in each hydrogel pocket (5%-5%-5% GelMa, 9%-9%-9% GelMA, 12%-12%-12% GelMA). This in order to promote an equal distribution of interstitial fluid flow by equalizing pockets' resistance to it.

With such setup, by applying an inlet rate of 0.3321 µL/min, an equal distribution of about 40 µL supernatant was collected after 20 h in all the three supernatant channels when 5% GelMA hydrogels were encapsulated (four replicates) (**Figure 38A**). Similar results were obtained under the same conditions by encapsulating 9% GelMA hydrogels (between 10 and 18 µL/supernatant channels, four replicates) (**Figure 38B**). By applying the same inlet pressure to the same setup encapsulating 12%

GelMA hydrogel, it was possible to measure an average of 5 µL/supernatant channels, but the values among four independent chip runs differed significantly (data not shown).

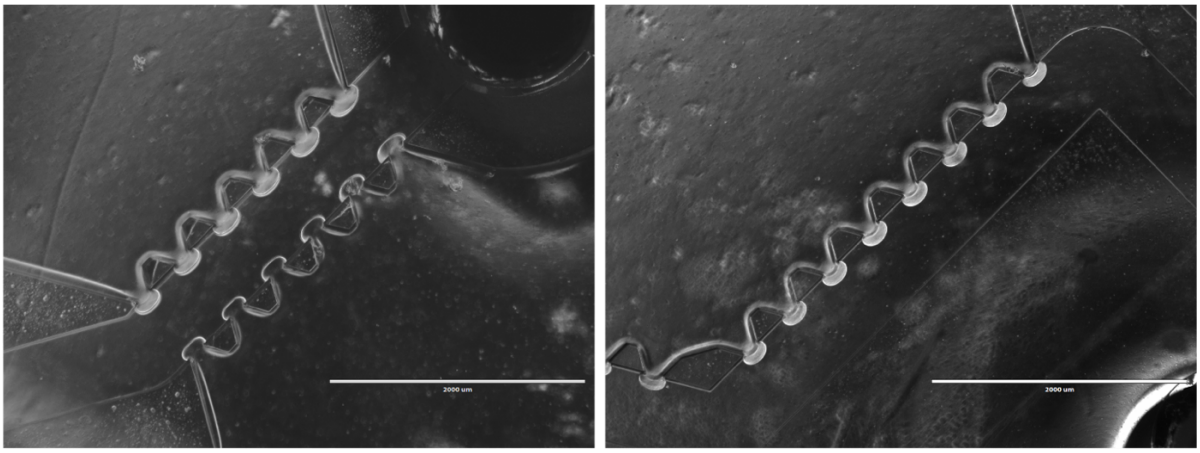

Figure 37. *Representative picture of GelMA hydrogel aspect at the interface between central (left) and supernatant (right) channels after 24 hours of chip run in the second liver lobule on a chip design. Magnification is 2x.*

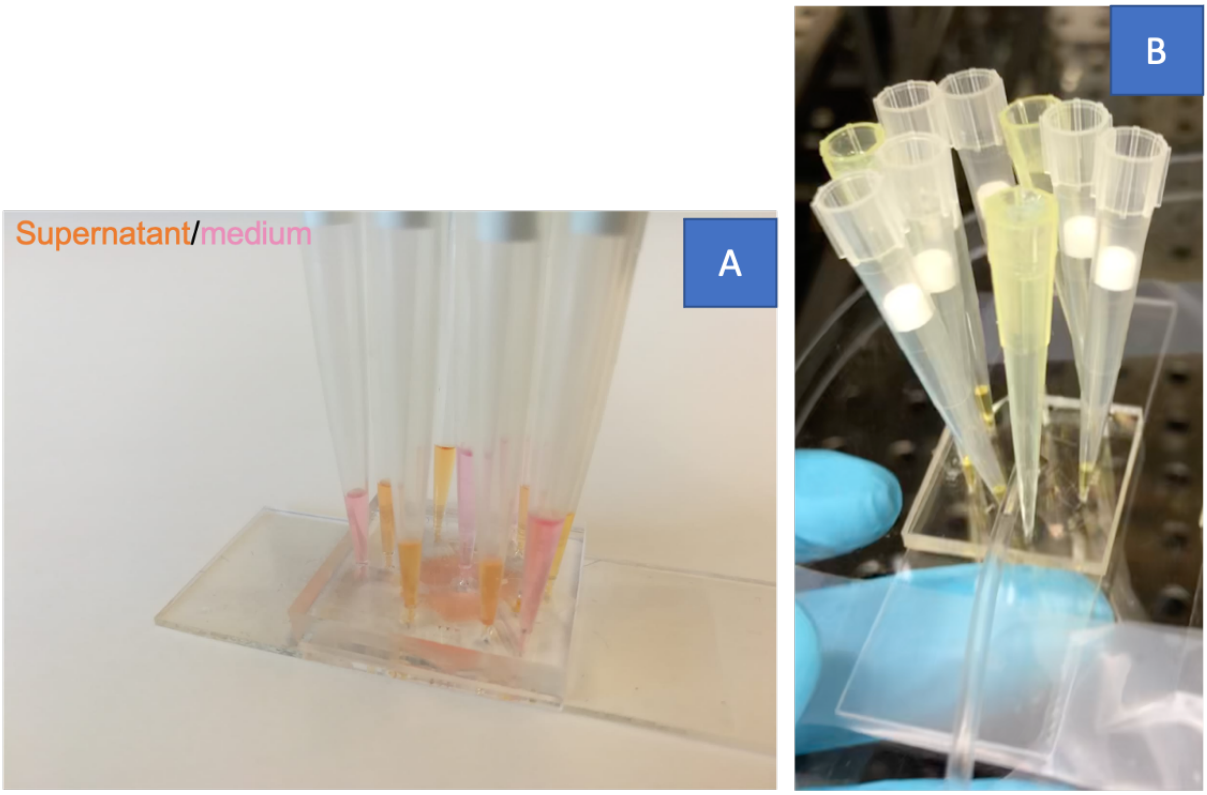

Figure 38. *Representative pictures of the second Liver Lobule on a chip design aspect after 20 hours of perfusion with a 0.3221 µL/min inlet flow rate. (A) Supernatant (orange) collected in the corresponding tips in a 5%-5%-5% GelMA hydrogel chip and (B) in a 9%-9%-9% GelMA hydrogel chips. Yellow pipettes in (B) are PDMS-filled, blocking the central channel outlets.*

4.4.3. **Fibrin loading and endothelialization**

As a proof of concept, in order to better elucidate the role that GelMA hydrogels play in the microfluidic devices under dynamic perfusion as well as in sustain endothelial cells proliferation and

micro-vasculature formation, single GF-HUVEC and hMSC were co-culture over 9 days in 3mg/mL fibrin hydrogels in the second liver lobule on a chip design pockets.

4.4.3.1. COMSOL simulations

By applying an inlet flow rate of 0.363 µL/min under the same fluidic conditions as the experiments conducted with GelMA hydrogels in the second liver lobule on a chip design (positive inlet rate; 0 µL/min outlets rate), the obtained COMSOL pressure distribution profile resulted similarly distributed to the one obtained for GelMA hydrogels, but with significant lower absolute values: from a maximum of about 10.5 Pa to a minimum of 1 Pa (**Figure 39**).

Furthermore, the interstitial flow velocity distribution retains a similar range of values as in 5% GelMA hydrogels, from a maximum of 3 µL/min at the external borders to a minimum of about 1.7 µL/min in the central part (**Figure 40, Table 12**).

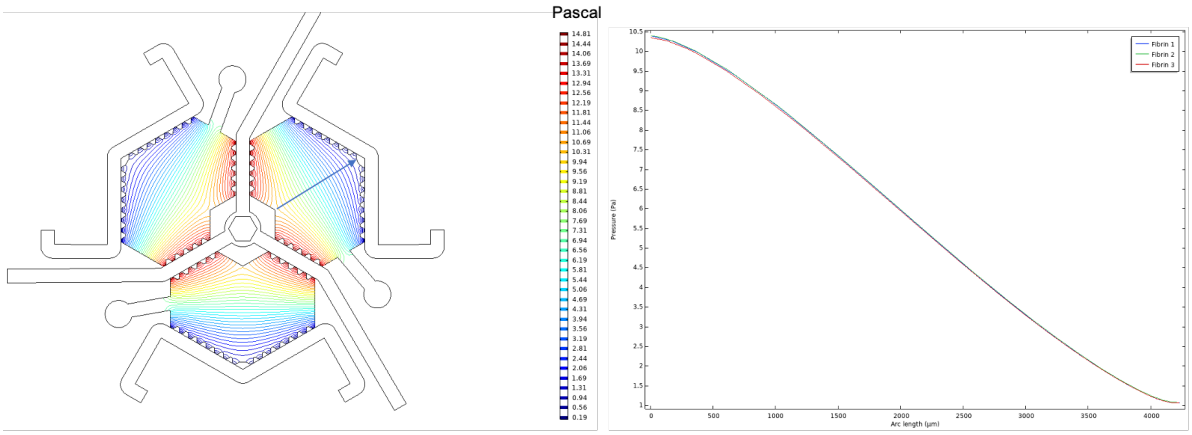

Figure 39. *COMSOL topographical pressure distribution in the second liver lobule on a chip design hydrogel chambers when 3mg/mL fibrin hydrogel are loaded (left). The graph (right) represents the pressure values measured throughout the entire pockets' length in the blue arrow direction.*

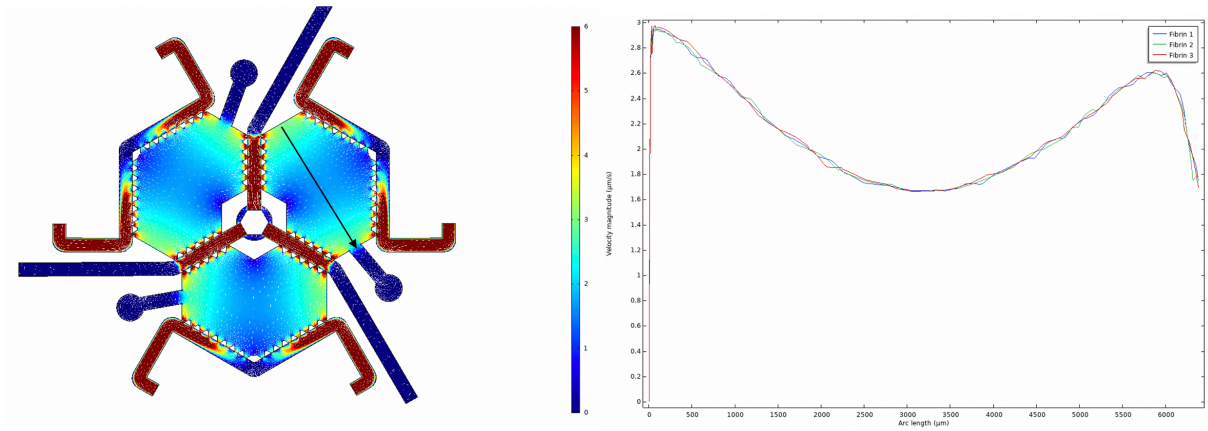

Figure 40. *COMSOL topographical fluid flow velocity distribution in in the second liver lobule on a chip design for 3mg/mL fibrin hydrogels, medium and supernatant channels when an interstitial fluid flow of 0.63 µL/min is applied (data are in µL/min). The graphs (right) represent the fluid flow velocity values measured throughout the entire pockets' length in the black arrows' direction.*

Table 12. *COMSOL calculation of supernatant collection in µL/min and mL/day at the three supernatant channels when an interstitial fluid flow of 0.63 µL/min is applied in the second liver lobule on a chip design in the presence of fibrin hydrogels.*

	µL/min	mL/day
Medium Inlet Total Fibrin	0.63	0.907
Supernatant Outlet - 1 (3mg/mL Fibrin)	0.21	0.302
Supernatant Outlet - 2 (3mg/mL Fibrin)	0.21	0.302
Supernatant Outlet - 3 (3mg/mL Fibrin)	0.21	0.302

4.4.3.2. Microfluidic runs

Microfluidic experiments under 0.63 µL/min inlet rate (closed outlets condition) and in the presence of the three fibrin hydrogels at the same concentration of 3mg/mL, displayed overall no channel obstruction due to hydrogel swelling and an equal daily distribution of supernatant at the corresponding channels.

Furthermore, the encapsulation of GFP-HUVEC and hMSCs in such setup showed the formation of vessel-like sprouting within 48 of perfusion, with subsequent confluent vascular-like network formation for over 9 days of continuous perfusion (**Figure 41**). Further, the pictures taken at day 9 of culture might also suggest the formation of luminal structures within the dense network. The addition of single THP-1 and tri-culture hepatic spheroids in this system showed the formation of potential endothelial sprouting from day 2 of culture (**Figure 42**). However, no further investigations over the long-term culture maintenance and daily cell variability were conducted.

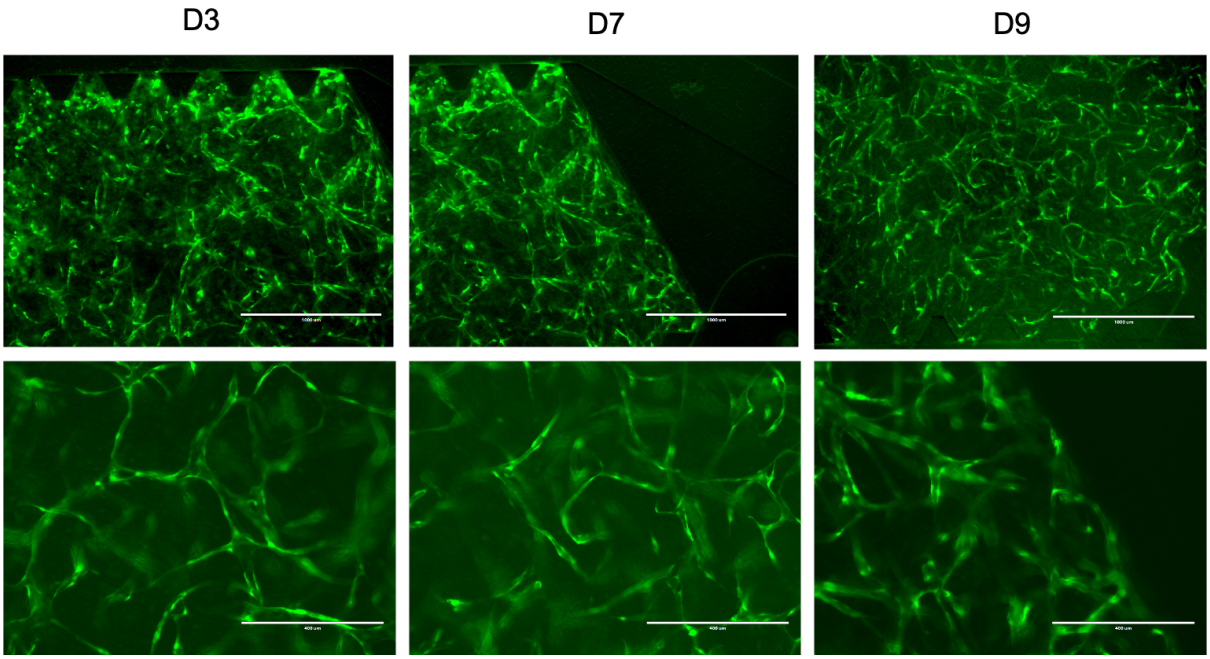

Figure 41. *Representative pictures of fibrin hydrogel endothelialization in the liver lobule on chip hydrogel pocket at day 3, 7 and 9 of culture. Magnification is 4x (top pictures) and 10x (bottom pictures).*

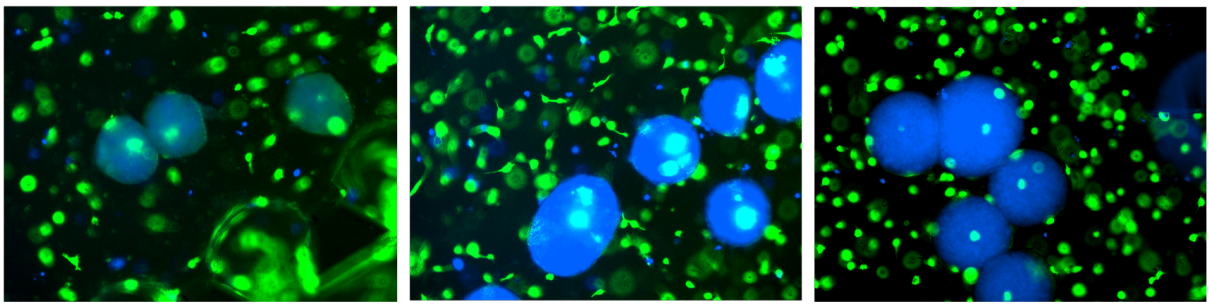

Figure 42. *Representative pictures of HUVEC (green), PMA-THP1 (blue single cells) and tri-culture hepatic spheroids embedded in fibrin hydrogel in the liver lobule on chip hydrogel pocket at day 2 of incubation. Magnification is 10x.*

5. Discussion

5.1. Spheroid growth and metabolic activity

In this research a multicellular hepatic spheroid model was successfully developed and characterized, by integrating key parenchymal (HepG2) and non-parenchymal (LX2, HUVEC) cells in a physiological-like ratio.

These hepatic tri-culture models were maintained in culture and characterized for over 7 days, showing an average size of 150-160 µm and high viability and functionality throughout the entire period. Specifically, detected increasing trend in albumin and VEGF secretion levels in these cultures (**Figure 18**) can be considered strong indicators of cells, and specifically, hepatocytes proliferation and functionality *in vitro* [85, 86]. Nevertheless, due to the difficulty of precisely quantifying spheroid's cell number over the culture time, it is not possible to conclude with certainty to what extent the detected levels of albumin and VEGF secretion was cause of the increasing cell number rather than an actual increase in cellular metabolic activity. Despite this, the similar spheroid size trend between the two medium conditions, together with the different levels in albumin and VEGF secretion between the two (**Figure 15,18**) can suggest the existence of a difference in cell metabolisms. Interestingly, the relative decrease in the levels of VEGF secretion in the culture condition incubated with lower EGM-2 ratio (18%) when the values were normalized to their unconditioned medium (**Figure S2**) can suggest that in this condition a nutrient deficiency stress occurred, negatively impacting the total VEGF secretion [87].
Such conclusion is also supported by the stronger reduction in GFP-HUVEC signal overtime in the 9:2 medium condition compared to the 1:1 (**Figure 17**) and this reinforces again the hypothesis of insufficient EGM-2 medium component in the former condition (18%).

Together with these observations, the choice of opting for an equally distributed ratio of media (1:1 ratio) is also supported by the impossibility of accurately quantify the exact growth rate, as well as the ratio change of the different cell types in the culture (*Paragraph 4.2.1.3.*).
In this research, a strategy aimed at quantifying both cell type number and ratio was adopted with cytometry (**Figure 19**). A way to potentially overcome the loss of signal seen during these kinds of measurements would have been the use of GMO cell lines (GFP, RFP, BFP). However, it is possible that a second factor that played a determinant role during the process of spheroids dissociation was the presence of an ECM-collagenous mesh within the hepatic tri-culture model that complicated the process of dissociation and laser gating. This hypothesis can be supported from the immunofluorescence staining of spheroids at day 4 of culture, where a dense mesh of collagen III was detected (**Figure 22**).

5.2. Cellular organization

In accordance with similar spheroids studies using HSCs with hepatic cancer cells [82, 83], it has been observed that HepG2 cells co-cultured with LX2 formed a compact and uniform-size sphere, characterized by the formation of an external capsule of HSCs at the periphery of the tissue, resulting in a dense capsule of ECM, rich in collagen type III (**Figure 20, 21, 22**).Together with that, the self-organization of HUVEC in the inner core of the spheroids might suggest a spontaneous organization of the tri-culture spheroids into different metabolic areas. It has been indeed reported that difference in

oxygen and nutrients demand from the cell types tend to create a self-organization into different metabolic zones, characterized by different roles during tumor growth, progression, and metastasis [88]. In particular, the rapid self-organization of HUVEC in the inner – potentially necrotic – core, can indeed be considered as the results of a lower metabolic activity compared to the other two cell types. This behavior might be either the result of a lower nutrient intake compared to its actual demand, probably due to insufficient EGM-2 medium compositions, or a result of cellular crosstalk with the other two liver-specific cell types (HepG2 and LX2). HUVEC were indeed chosen to fulfill the purpose of tissue pre-vascularization, despite are not a liver organ specific cell line. The accessibility of such cell type, broad applicability and standardized culture protocol makes them an easily accessible and attractive source for many applications. In this sense, it would be interesting to evaluate in the future if the incorporation of organ specific endothelial cell lines (*i.e.,* LSEC) instead of HUVEC would help in recapitalizing tumor phenotype, overcoming the endothelial zonation in the inner core. Concurrent with this, another complementary way to adopt in order to potentially overcome spheroid uncontrollable growth with consequent formation of necrotic cores, might be the use of primary cell lines over immortalized hepatic cell lines. Indeed, the stability of primary hepatic spheroid size over the duration of the culture period may allow for the sufficient diffusion of oxygen and key nutrients throughout the entirety of the microtissue, arresting the formation of potential necrosis, resulting in a more representative *in vivo* like hepatic model [89].

5.3. GelMA hydrogels

GelMA hydrogels offers a simple, robust, and highly mechanical tunable systems to develop consistent controllable system platforms over different pathophysiological ranges in the presence of cells through simple modifications to GelMA percentage in the hydrogel [73]. In this project, the mechanical characterization of such hydrogels for the identification of three pathophysiological relevant GelMA hydrogel concentration has been successfully conducted through rheology and compared with *ex vivo* rheological measurements and *in vivo* MRE data from literature (**Table 9**).

Although rheological measurements are the most suitable for the analysis of the collective mechanical properties of 3D bulk matrices through the determination of shear modulus as well as viscous properties [90], it must be considered that soft tissues behave as nonlinear, anisotropic, and non-uniform viscoelastic materials [91]. Consequently, their mechanical properties depend on deformation and deformation rate. In case of soft material as the here characterized GelMA hydrogels, this might imply problems in reproducibility and reliability of measurements and interpretation of results. Particularly, the intrinsic tissue characteristics, such as internal inhomogeneity and anisotropy, can deeply influence the measurements' reliability of both synthetic materials, such as hydrogel matrices, and tissues, such as *ex vivo* organs [92]. Furthermore, it must be taken into consideration that local hydrogel mechanical properties can differ significantly when cells – and particularly spheroids - are encapsulated or when subjected to local stresses, such as external hydrostatic pressures or water retention [93, 94].

Decellularized tissues matrices can be an alternative to the exploitation of synthetic hydrogels. These biologically derived scaffolds can retain unique, individual ECM protein composition and internal structure of their native organ, reflecting its physio pathological microenvironment [95]. However, based on the different decellularization protocols, such matrices differ significantly, reducing the reproducibility of the platform. Furthermore, the decellularization procedure can cause ECM

components loss, altering the native matrix stiffness and the biochemical microenvironments sensed by cells [96].

In this project, the choice towards a more reproducible and controllable platform at the expense of a more biomimetic – but less consistent – matrix was preferred.

5.4. Microfluidic chip

A hexagonal-shape microfluidic platform that provide simultaneous perfusion of three separated hydrogel pockets resembling three different pathophysiological stages of tissue fibrosis was successfully developed and characterized.

After extensive experimental tests, the original design was modified in order to reduce the number of variables that come into play during chip runs, improving device reproducibility and outcomes consistency. Firstly, the influence of GelMA hydrogel swelling on channel clogging was limited (**Figure 37**). Second, the formation of potential necrotic areas due to drops in interstitial fluid flow values and distributions was reduced (**Figure 34,35**). And third, higher control over fluid flow distribution inside hydrogel chambers was obtained (**Figure 35, Table 11**). Nevertheless, the latter modification, despite significantly improved the system reproducibility, did not allow the generation of wall shear stress in those channels, due to the blockage of medium outlets, limiting the possibility to endothelialize these regions of the chip. However, although this could limit the potential formation of an interconnected vascular network at the channels-pocket interface, the presence of important – although notably reduced – GelMA swelling at these interfaces could have anyway complicated the process of endothelialization.
In addition, the decision of further simplify the system by adding same percentage hydrogels in all the three pockets further improved device performance. By equalizing the resistance exerted by the hydrogel pockets, it was indeed possible to obtain consistent results in terms of supernatant collection and hydrogel integrity when 5% and 9% (w/v) GelMA hydrogels were encapsulated and when the same fluid flow inlet suggested by COMSOL simulations was applied (**Figure 38**). However, despite an equal accumulation of supernatant was measured in all the three channels, the measured amount after 20 hours of run resulted significantly different from that expected by COMSOL simulation (**Table 11**). Surely, a small part could have been the result of fluid evaporation; however, the biggest part of that might be due to the generation of an opposite pressure exerted from the liquid accumulated in the central channels to the syringe pump (opposite to the pressure inlet direction). This explanation is reinforced by the experimental observation about the tendency of the inlet needle to be pushed out of the central reservoir during the microfluidic runs. While this tendency resulted to be almost neglectable for the 5% and 9% GelMA conditions, it might have been the cause of the experimental inconsistency of 12% GelMA chip run outcomes. The lower permeability of 12% GelMA hydrogel, indeed, can further increase the resistance exerted from the system over the desired fluid flow partition.

5.4.1. **Endothelialization**

Furthermore, with such setup, a consistent viable endothelialized supernatant channels were obtained, together with the presence of clusters of PMA-activated monocytes attached to the endothelial layer (**Figure 36**). Despite the experiments were only conducted under static culture

condition, the organization observed recapitulated a physiological-like cellular organization found in the vessel lumen, prior to potential cellular extravasation [97, 98].

5.4.2. **Fibrin hydrogel**

As a proof of concept, the same microfluidic setup tested with GelMA hydrogels was tested by incorporating fibrin hydrogels at the concentration of 3mg/mL. Fibrin hydrogel has previously proven its feasibility as stable and perusable material during extensive microfluidic experiments [99], providing also good cellular growth and viability and microvascular formation [100].

The microfluidic perfusion experiments here conducted confirmed these observations, allowing the perfusion and creation of an interstitial flow that could be detected by cells, that, in this platform, showed to form vessels-like networks together with potential formations of luminal – perfusable – structures.

5.4.2.1. Vascular formation in fibrin

The presence in this microfluidics system of a co-culture of HUVEC and hMSCs embedded in fibrin hydrogels can have boosted the microvasculature-like structure formation compared to single cultures of HUVEC in GelMA hydrogels (**Figure 41**). Despite this, to our best knowledge, there are no studies that reported a possible reason of HUVEC decrease viability when embedded in GelMA hydrogels. However, it is worthy to note that in this research HUVEC-hMSCs in fibrin were cultured in 100% EGM-2 medium, contrary to the 33% of the tri-culture medium composition used for the multi-cellular hepatic GelMA hydrogels. Together with that, the long-term co-culture of HUVEC with liver specific cells, such as HepG2 and LX2, could have promoted a cascade of molecular events leading to chemical or mechanosensation-HUVEC inhibition or apoptosis.

The inner nature of GelMA to swell till the 150 % of its original volume [101] when subject to perfusion or – external – hydrostatic pressures , make this material a weak candidate in those application where a higher control over every physicochemical parameter is required, as microfluidics. However, on the other side, fibrin hydrogels showed less mechanical tunability over broad ranges of pathophysiological stiffness, with an overall lower elastic modulus [102], limiting its exploitation in those experiments that require a significant degree of mechanical properties versatility.
Despite this, it can be possible to speculate that the herewith developed microfluidic system showed to be a promising platform for long-term, dynamic culture when a more stable material is exploited. However, it is important to consider that not extensive experiments have been conducted by long-term incorporating the tri-culture hepatic spheroids in such device, and therefore it is not possible to speculate over the feasibility of our system in providing a sufficient physiological-relevant environment for the culture of such complex dynamic *in vitro* microenvironment.

5.5. Static multi-culture GelMA hydrogels

A 3D *in vitro* static models were here established in order to study and screen the pro-fibrotic mechanosensitive response of hepatic cells when cultured in a static microenvironment subjected to physio-pathological matrix stiffnesses. These multicellular hepatic models showed overall long-term culture viability (over 14 days), regardless GelMA hydrogel concentration.
Taking a closer look at the molecular analysis, protein secretion levels detected with ELISA at day 1, 6 and 14 of culture suggests the presence of an initial (day 1- day 9) proliferative (albumin and VEGF

increase) and pro-inflammatory (IL-6 and TNF-*α*) phase, followed by a proliferative stabilization and inflammation attenuation in all three culture conditions (**Figure 29**). However, even if not statistically significant, the multi-culture 9% GelMA hydrogel conditions seemed to maintain higher TNF-*α* and IL-6 secretion also in the second period of culture (day 9 – day 14), suggesting the potential presence of a more marked pro-inflammatory environment. However, it must be reported that also for this analysis it was not possible to standardize the protein secretion to the actual number of cells present in the hydrogel. Therefore, the absolute variation in protein secretion might be also attributable to a variation in cell proliferation in that culture condition (i.e., 9% GelMA hydrogels). However, although genetic material loss and degradation during the isolation process could have occurred, no significant difference were detected in the nucleic acid concentration among the three GelMA conditions during the nanodrop measurement performed after RNA isolation (**Figure S7**).

Taking a look at the relative genetic fold expression of specific pro-fibrotic genes at day 14 of culture (**Figure 28**) it is possible to have a more in-depth insight into the fibrotic state of each GelMA hydrogel culture condition. In particular, the *Albumin* overall relative upregulation in 5% and 9% GelMA and down regulation in 12% GelMA hydrogels seems to be consistent with what observed by *Zhao et al.*, that attributed its genetic downregulation to the influence of the microenvironment when hepatocytes are culture in relative stiffer matrices than their physiological one [103]. Complementary with that, when embedded in matrices characterized by high mechanical compliance, *albumin* levels featured a significant increase [104]. This hepatocytes tendency towards a higher genetic activity in 5% and 9% GelMA is reinforced by *CXCL10* expression at day 14 of culture. This gene has shown to be upregulated in hepatocytes associated with pro-inflammatory liver infiltrate and positive correlated with the degree of lobular inflammation, playing as a chemoattractant agent for immune cells [105]. Concurrent with this, the overall upregulation of *VEGF* from all the three GelMA conditions further reinforce the hypothesis about the hepatocyte's contribution in the pro-fibrotic environment and further expand it to the action and interplay with other key hepatic cells present in the platform. *VEGF,* indeed, not only has been proven to promote and perpetuate fibrosis progression and monocytes infiltration when released by hepatocytes, but, mostly, when produced by HSCs [12], the main effectors of the fibrotic microenvironment. The presence of such pro-fibrotic environment progression can also be supported by the upregulation of *α-SMA* and *TGF-β* gene expression in 5% and 9% GelMA hydrogel conditions, while are downregulated in 12% GelMA hydrogels. This result seems to confirm what observed with the immunofluorescence analysis at day 14 of culture (**Figure 24**). From microscopic analyses, indeed, the cellular pro-fibrotic action can be seen in the elongated and migratory-like phenotype showed by HSCs when stained with *α-SMA* in the 5% and 9% GelMA hydrogels. The migratory-like phenotype observed is in accordance with what reported in several studies [106-108], where the invasion of stromal cells, like HSCs, into the ECM has been proven to be a clear hallmark of aberrant ECM deposition and remodeling. HSCs have shown to invade the ECM in a stellate pattern to form a dendritic network of extrusions upon spheroids cultures [107]. Together with that, *TGF-β* and *α-SMA* downregulation and secretion inhibition has been observed to occur when cell ability to deform the surrounding matrix is impaired, resulting in a cellular volume expansion limitation, with no possibility of morphological adaptation and migration [109]. The predominant epithelial-like behavior of embedded LX2 cells in 12% GelMA hydrogels confirmed by confocal pictures (**Figure 24**), together with the genetic *α-SMA* and *TGF-β* downregulation, reinforced the evidence of a caging condition of the hepatic tri-culture spheroids inside GelMA hydrogel matrix.

Furthermore, the marked upregulation of *PDGFβ* in the first two GelMA conditions, and particularly in 9%, together with the down regulation in 12%, reinforced the previous hypothesis and can contribute to distinguish the presence of two different fibrotic stages between 5% and 9% GelMA hydrogels. This gene, indeed, has been proven to be particularly overexpressed during the end stages of liver fibrosis (cirrhosis), even without significant simultaneous upregulation of *TGF-β*-related pathways [110]. Furthermore, and potentially in line with what observed in the experiments here reported, *PDGFβ* has also shown to down-regulate *collagen type I* expression in mice wound healing models, in favor of *collagen type III* deposition [111]. This latter gene, here particularly upregulated in 9% GelMA hydrogels, has been indeed found to be clearly related to cirrhotic liver fibrosis [112].
The overall downregulation of *MMP9* observed (**Figure 28**) seems to be another marker of fibrosis perpetuation, not participating in the aberrant ECM degradation, probably partly due to HSCs inhibitory action [113]. MMP9 activity has shown to be modulated by matrix stiffness, where increased fibrotic ECM downregulates *MMP9* expression, secretion and activity during fibrosis [114]. However, the role of MMP9 during tissue fibrosis is still ambiguous and has shown to both play a role in reducing and promoting fibrosis, based on which cells are mainly induced in its production [115].
The hypothesis of a more marked pro-inflammatory state in 5% GelMA condition can also potentially find confirmation in the apparent upregulation of M1 macrophage-like marker *CD64* [116] , as well as *IL-8,* hallmark cytokine of acute inflammation [117]. Together with that, the presence of monocytes activity and potentially differentiation towards the M1 phenotype particularly in 5% and 9% GelMA hydrogel conditions can be further supported by the presence of bubble-like clusters qualitatively detected in the second period of culture (day 9- day 14) through bright field microscopy analysis (**Figure S4**).
According to their relatively big size (10-15 μm) compared to most extracellular vesicles, which usually range in the *nm* orders [118], they could be classified as large oncosomes [119]. Such large extracellular vesicles are a class of tumor-derive vesicles that originates directly from the plasma membrane budding of tumor-like cells. Their formation is particularly evident in highly migratory, aggressive tumors and several studied indicate that can form a bioproduct used by migratory cells as propulsive force to migrate [120]. Further, these large vesicles generally carry oncogenic cargos (such as lipids, protein, DNA, mRNA and non-coding RNAs) which modulate the microenvironment by promoting cellular proliferation and differentiation [121]. However, to date their specific functions and roles in physiological and pathological conditions remains unanswered [122]. Furthermore, the only qualitative observation of such vesicle's formations in this project, without any quantitative, molecular analysis, do not allow to further speculate about their origin and function during the culture period.

Our data on *TNF-α* down regulation for 5% GelMA hydrogels, together with the overall down regulation of *CCL2* in all three GelMA conditions are in apparent disagreement with the above results and previous literature studies [123, 124], where have been proven to play a pivotal role in immune-mediated fibrotic progression. However, the stiffness-proportional downregulation of *CCL2* detected in this study seems to be in line with some studies where the tendency of *CCL2* to be highly downregulated as matrix stiffness increase was proved [125].

Further, no M2-like phenotype macrophages presence was here studied through the expression of specific gens (i.*e., CD163*). Therefore, no speculations about the presence of an anti-inflammatory state for any of the GelMA hydrogels conditions can be done.

Overall, the more marked relative upregulation of acute inflammatory-involved genes (*CXCL8, TGF-β*, *α-SMA, CD64*) in 5% GelMA hydrogels, together with the prevalence of a marker upregulation of end stages fibrotic genes (*PDGFβ, Collagen type III, CXCL10*) in 9% GelMA can sustain and confirm the hypothesis that our multi-culture hepatic models is able to mimic an early fibrotic stages in 5% bulk GelMA hydrogels (about 2 kPa), while a more late fibrotic stage in 9% GelMA hydrogels (about 5 kPa), under static culture conditions. As for the 12% GelMA hydrogel condition, all the above relative downregulated genes after 14 day of culture (*PDGFβ, CXCL8, CXCL10*, *TGF-β 1, α-SMA, albumin*) suggest the presence in this condition of a strong intra-spheroid compressive stress, probably mainly caused by hydrogel crosslinking density, that limited proper cell migration and invasion into hydrogel matrix, promoting the formation of a physical-solid like jammed phase among hepatic spheroids [126].

Beyond all the above considerations and speculations, the notably high variance among qPCR measurements between the experimental repetitions make the molecular analysis difficult to interpret unequivocally. The non-statical significance intercurrent between each condition make the relative analysis to be considered only as *semi-quantitative.* The inclusion of single measurements in each graph, together with the color distinction between the two different rounds of experiments, each of which characterized by three biological replicates, want to offer an interpretation as objective as possible to the reader.

6. Conclusions

In this research a physiological relevant 3D *in vitro* model to study the effects of the mechanical properties of the matrix on liver tissue fibrosis development and functioning was established, by i) developing a liver microtissue model in form of a multicellular hepatic spheroid model and ii) providing it with a physio pathological relevant tissue microenvironment by mimicking key mechanical and biological features.
In detail,

- A multicellular hepatic spheroids 3D model was established by successfully integrating key stromal with liver parenchymal cell lines in a physiological-relevant ratio and their growth, morphology, cell organization and metabolic activity were fully characterized over 7 days of culture.

- concurrent with this, the mechanical and structural properties of three different concentration GelMA hydrogels that resemble the typical pathophysiological ECM properties were identified and fully characterized and their suitably in promoting and sustaining 3D pro-fibrotic mechanosensitive cellular behavior was proved.
    - Specifically, by incorporating the hepatic multicellular spheroids, 3D *in vitro* static models were successfully established, and the pro-fibrotic mechanosensitive response screened in such platforms identified the onset of different fibrotic stages depended on matrix stiffness.

- Finally, a microfluidic platform capable of hosting a multiplex of different hydrogels in a dynamic and biomimetic environment was developed and optimized. Such platform showed its feasibility as long-term dynamic culture system, allowing the simultaneous perfusion of three different hydrogel pockets and providing the generation of physiological relevant interstitial fluid flow and wall shear stress, promoting the formation of a vascular-like network in the perfused chambers.

Altogether, this research opens up to the possibility of developing new advanced 3D *in vitro* tissue models for efficiently recapitulating the mechanosensitive pathways underpinning tissue fibrosis pathogenesis and progression and providing a step towards the development new promising reliable tools for the screening of new therapeutic targets.

7. Future work

Regarding the multicellular hepatic spheroids 3D model, future work should be direct towards the establishment of a more reliable *in-vivo* like hepatic model in terms of cellular growth, self-organization and vasculature formation.

In order to obtain that, a method can be the use of multi-cellular organoids models instead of spheroids. These structures, characterized by more complex and self-assembling liver-specific cell types, have proved to follow sequential tissue developmental paradigms similar to what observed *in vivo* [50, 52]. Compared to spheroids models, they have shown to better replicate tissue shape and organization, featuring physiologically-like distributions of the different cell types. In particular, iPSCs organoids have been extensively proven to follow typically developmental processes of *in vivo* tissues and can be therefore used to for studying tissue disease development [127]. In this sense, it would be possible to develop multi-cellular hepatic iPSCs organoids that retain quiescent phenotype when maintained in their native culture and become potentially activated in response to matrix biomechanical stimuli, allowing therefore the study and comparison of healthy and fibrotic states in one single platform.

On the other hand, adult stem cell (ASCs) derived organoids showed to recapitulate adult tissue repair, instead of early development [128]. Therefore, their application in a highly regenerative organ as liver can provide a reliable and stable platform to study the difference pro-reparatory process that occur in fibrotic liver models triggered by the different ECM rigidities our system would provide them. Furthermore, these systems have also proven to sustain and promote vasculature development and progression when mechanically stimulated in microfluidic systems [129]. Based on this method, the integration of endothelial progenitor cells in these hepatic multicellular organoids systems could indeed promote the formation and maturation of vascular network *in situ* under physiological relevant interstitial fluid flow in our microfluidic systems. This, in turn, could further promote spheroids-ECM vessels integration and enhance the internal organoids tissue maturation.

Regarding the integration of the system in the microfluidic platform, the exploration of biomaterials that ensure a good performance with limited-to-controllable swelling behavior during extensive microfluidic experiments is strongly suggested.

As previously discussed, decellularized liver matrices could be good candidates for restoring the native matrix structure and composition. However, based on the specific research aim, the use of more reproducible and controllable platforms can also be taken into consideration. Among these, together with fibrin – whose compatibility with our system has been preliminary proven in this research– collagen and, in particular, reinforced collagen hydrogels can be good alternatives when both improved microfluidic compatibility and mechanical tunability are required. In detail, a possible option could be the characterization of collagen type I hydrogels reinforced with ribose as extra-crosslinker. Preliminary studies have shown that such a system, upon ribose crosslinking, can reach elastic moduli in the range of 10-15 kPa, while maintain high internal porosity (90%) [130].

8. Supplemetary:

Table S1. *qPCR forward and reverse primers.*

Primer	Forward (F) sequence 5'-3'	Reverse (R) sequence 3'-5'
Albumin	CCGTGGTCCTGAACCAGTTA	TCGCCTGTTCACCAAGGATT
αSMA	CCCCATCTATGAGGGCTATG	CAGTGGCCATCTCATTTTCA
TGFβ-1	GCGTGCTAATGGTGGAAACC	GAGCAACACGGGTTCAGGTA
VEGFa	GCTCAGAGCGGAGAAAGCAT	GCAACGCGAGTCTGTGTTTT
Col1α1	GTACTGGATTGACCCCAACC	CGCCATACTCGAACTGGAAT
Col3α1	AGTCAAGCCTAGCCTGATAATCC	ACATATGCACCCACTCACCTT
TNFα	CTTCTGCCTGCTGCACTTTG	GTCACTCGGGGTTCGAGAAG
CCL2	GATCTCAGTGCAGAGGCTCG	TTTGCTTGTCCAGGTGGTCC
CXCL10	GGACTTTCCGCTAGACCCAC	GTCCTCATGGTTAAGGCCCC
CXCL8	CACTGCGCCAACACAGAAAT	ATTCTCAGCCCTCTTCAAAAACT
PDGFβr	CATGGGGGTATGGTTTTGTC	GTAAGGTGCCAACCTGCAAT
MMP9	TCTTCCCTGGAGACCTGAGA	TTTCGACTCTCCACGCATCT
CD64	AGTCAAGCCTAGCCTGATAATCC	ACATATGCACCCACTCACCTT
CD319	CACAACCCCTCTTGTCACCA	GGAGTAGCCTCCATCTGGGA
CD163	GACAGCGGCTTGCAGTTTC	TGTGGCTCAGAATGGCCTC

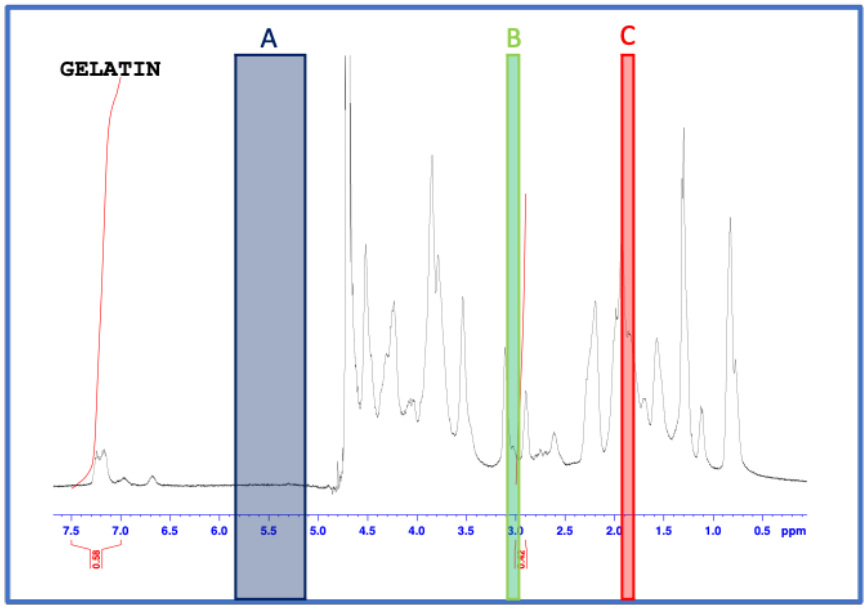

Figure S1. *Chemical structures of* gelatin, and its *respective 1H-NMR spectra.* Red *"C"* and blue *"A" represent the signals of the methyl group and acrylic protons of the grafted methacrylic group respectively,* and green *"B" indicates the signal of lysine methylene.*

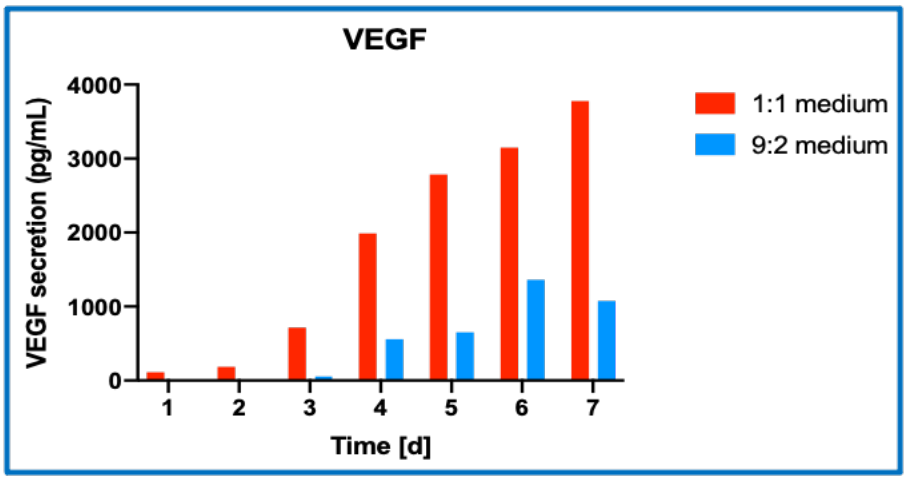

Figure S2. *Standardized VEGF secretion to culture medium measured through ELISA over the 7-day culture period in both medium conditions in agarose microwell arrays. Data are the mean value of one measurement per condition. Each measurement is the collected supernatant from one agarose well, containing 1500 independent spheroids.*

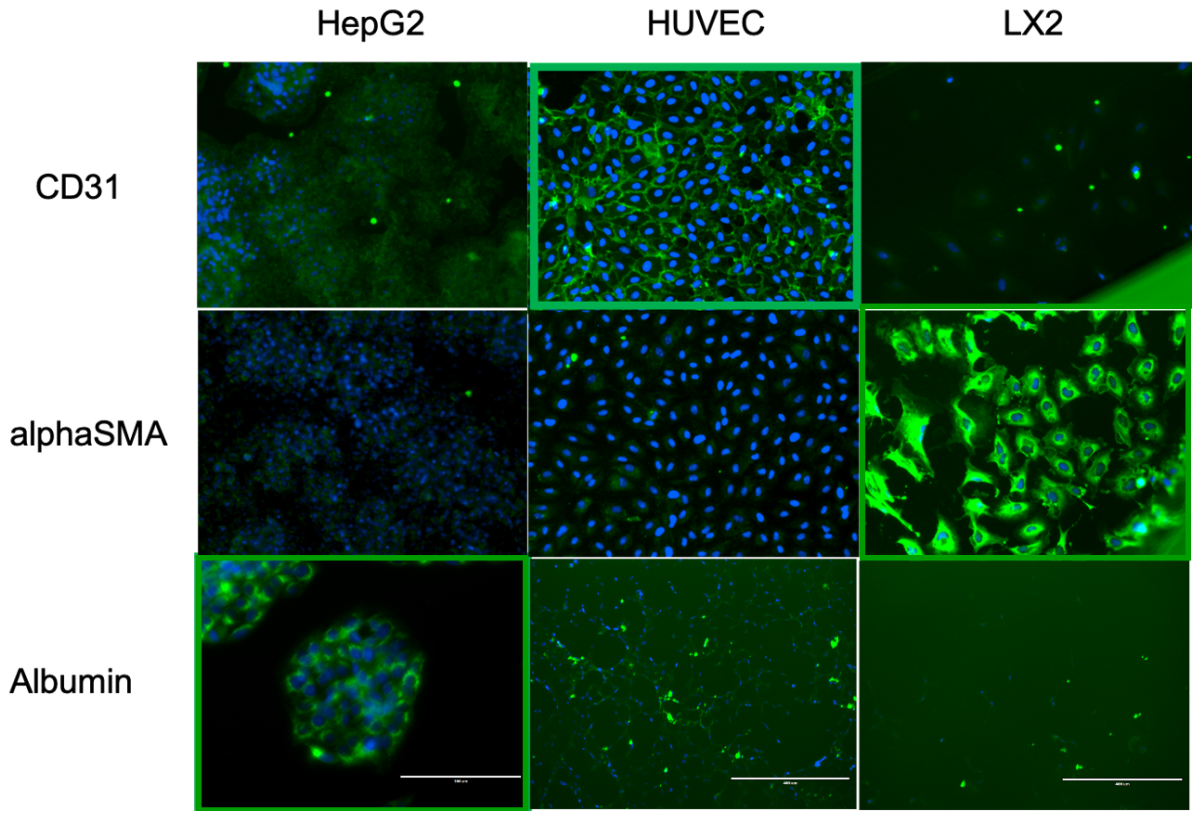

Figure S3. *Representative immunofluorescent pictures for cell specificity assessment of CD31, α-SMA albumin primary antibody (green, AF 488 secondary antibody) for 2D HepG2, HUVEC and LX2 monoculture. From the analysis, CD31 shows specificity of HUVEC monoculture, while α-SMA for LX2 and albumin for HepG2. Cellular nuclei are identified with Hoechst 33342 staining (blue). Magnification is 20x, except for the albumin-HUVEC and LX2condition (bottom left) picture where is 10x.*

Table S2. *Cytometry measurement of HepG2, HUVEC and LX2 cell percentage at day 0 of hepatic spheroid tri-culture with three different immunofluorescence staining conditions. I AB: I antibody; II AB: II antibody; vWR: von Willebrand factor.*

Cell type	IF staining (I AB; II AB)	Measured %

HepG2	Non stained	-
HUVEC	GFP + vWR; AF 488	99.47%
LX2	α-SMA; AF 647	99.91%

Cell type	**staining (I AB; II AB)**	**Measured %**
HepG2	Albumin; AF 647	86.05%
HUVEC	GFP	-
LX2	α-SMA; AF 594	86.05%

Cell type	**IF staining (I AB; II AB)**	**Measured %**
HepG2	Albumin; AF 647	99.2%
HUVEC	Non stained	-
LX2	α-SMA; AF 488	99.91%

Table S3. Statistical significance of protein secretion detected by ELISA between different GelMA hydrogel conditions and days of culture. Data are from three individual experiments, 3 measurements per experiment. Ordinary two-way ANOVA, *p<0.05, **p<0.01, ***p<0.001, ****p<0.0001.

ALBUMIN	**Condition**	**Statistical significance**
	5% D1 Vs. D9	*
	9% D1 Vs. D9	*
	9% D1 Vs. D14	*
	12% D1 Vs. D9	**
	Overall D1 Vs. D9	***
	Overall D1 Vs. D14	***

VEGF	**Condition**	**Statistical significance**
	5% D1 Vs. D9	***
	5% D1 Vs. D14	****
	9% D1 Vs. D9	****
	9% D1 Vs. D14	****
	12% D1 Vs. D9	****

	12% D1 Vs. D14	****
	Overall D1 Vs. D9	****
	Overall D1 Vs. D14	****

TNF-alpha	Condition	Statistical significance
	All	NS

IL-6	Condition	Statistical significance
	Overall D1 Vs. D9	**

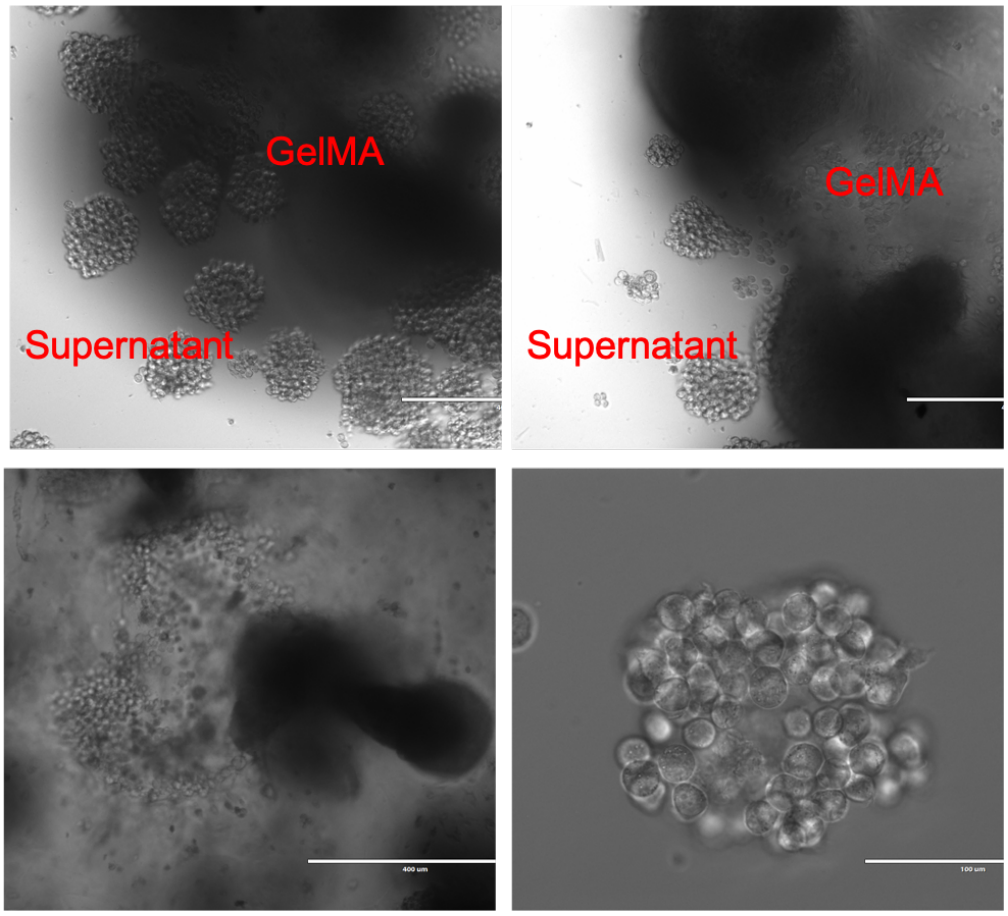

Figure S4. *Representative pictures of "bubble-like" clusters accumulation released in the supernatant (top and bottom right pictures) and entrapped in the ECM between hepatic tri-culture spheroids (bottom left). Magnification is 10x for all the picture, apart form the bottom right, where is 40x.*

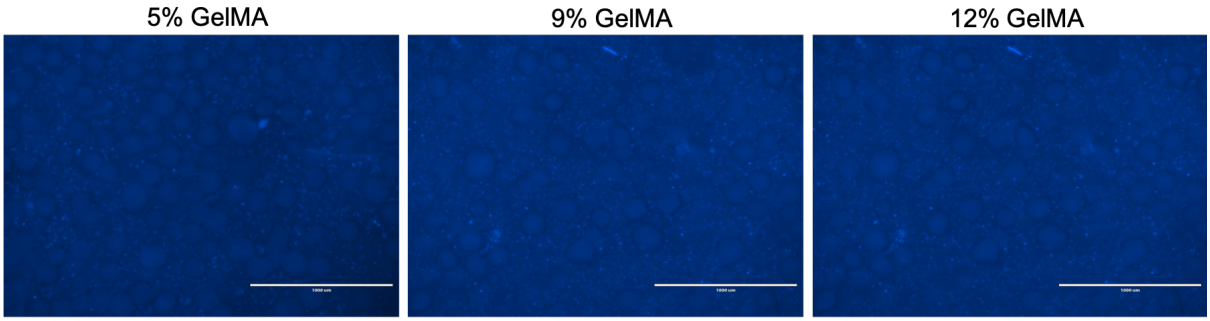

Figure S5. *Representative THP1 distribution into 5%, 9%, 12% (w/v) hepatic multi-culture GelMA hydrogels at day 3 of culture. Magnification 4x.*

Table S4. *Semi-quantitative report about supernatant outcome after 20 hours of microfluidic run of the first liver lobule on a chip design in correspondence of 5%, 9% and 12% (w/v) GelMA chamber, with increasing applied interstitial fluid flow (0.4 – 4.0 µL/min).*

Interstitial flow velocity (µL/min)	Supernatant outcome description after 20 hrs of chip run
0.43	No supernatant collected; supernatant channels dried
1.21	No supernatant collected; supernatant channels dried
2.0	No supernatant collected; supernatant channels perfused
2.3	5% GelMA pocket: 700 µL; 9% GelMA pocket: 0 µL; 12% GelMA pocket: 12 µL
2.5	1st) 5% GelMA pocket: supernatant overflow; 9% GelMA pocket: 40 µL; 12% GelMA pocket: 0 µL 2nd) 5% GelMA pocket: 300 µL; 9% GelMA pocket: 0 µL; 12% GelMA pocket: 0 µL 3rd) 5% GelMA pocket: 300 µL; 9% GelMA pocket: 0 µL; 12% GelMA pocket: 20 µL
3.0	1st) 5% GelMA pocket: supernatant overflow; 9% GelMA pocket: 10 µL; 12% GelMA pocket: 10 µL 2nd) 5% GelMA pocket: supernatant overflow; 9% GelMA pocket: 0 µL; 12% GelMA pocket: 0 µL 3rd) 5% GelMA pocket: supernatant overflow; 9% GelMA pocket: 0 µL; 12% GelMA pocket: 2 µL
4.0	Overall supernatant overflow

Table S5. *COMSOL calculation of supernatant collection in µL/min and mL/day at the three supernatant channels when an interstitial fluid flow of 0.3321 µL/min is generated in the second liver lobule on a chip design.*

	µL/min	mL/day
Medium Inlet Total	17.0000	24.4800
Medium Outlet Total	16.7084	24.0602
Supernatant Outlet – 1 (GelMA 5%)	0.1793	0.2582
Supernatant Outlet – 2 (GelMA 9 %)	0.0387	0.0558

Supernatant Outlet – 3 (GelMA 12 %)	0.0007	0.0011

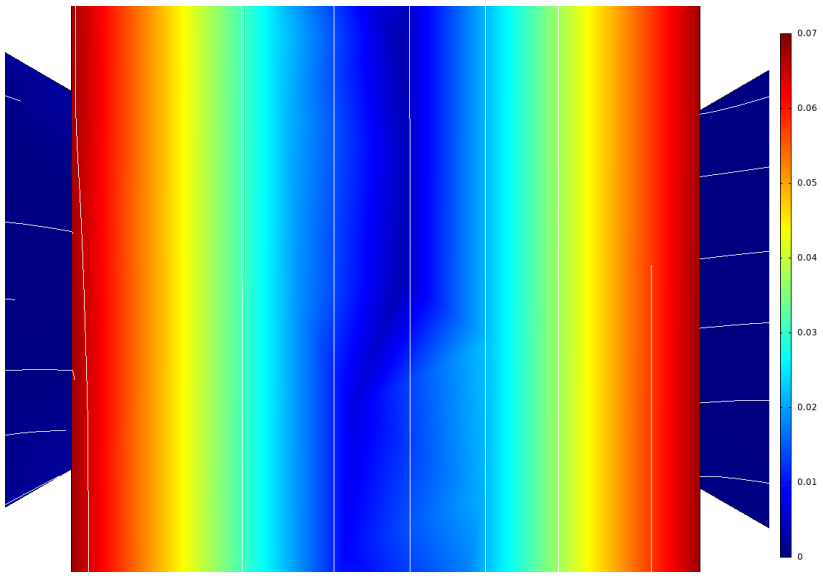

Figure S6. *COMSOL topographical shear stress distribution in the second liver lobule on a chip design at the central channels when a fluid flow difference of 0.3321 µL/min is applied, by injecting 17 µL/min in the central inlet and withdrawing a total of 16,7084 µL/min from the channel outlets. Shear stress values are expressed in Pa.*

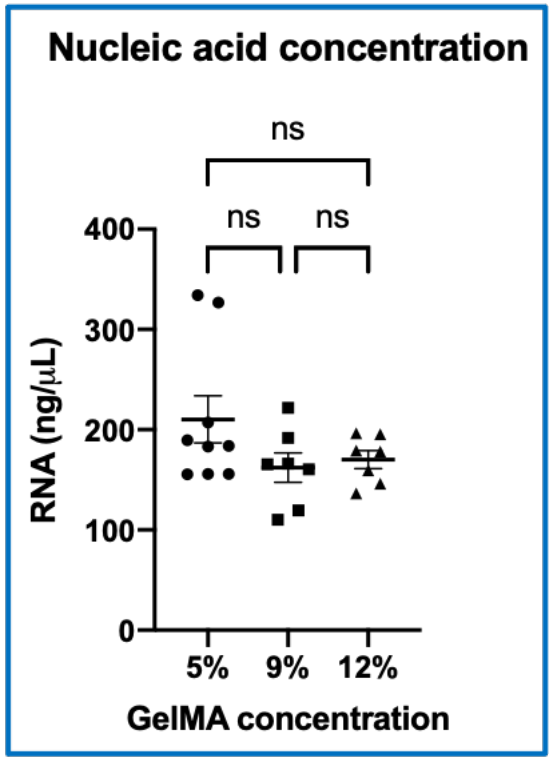

Figure S7. *RNA Nucleic acid concentration values measured using NanoDrop. Data are the mean value ± SD, n=9. One-way ANOVA, ns = no significance.*

9. REFERENCES

1. Monga, S.P. and S.P. Monga, *Molecular pathology of liver diseases*. Vol. 5. 2011: Springer.
2. Tortora, G.J. and B. Derrickson, *Essentials of anatomy and physiology*. 2013: Wiley Hoboken.
3. Kiernan, F. and J.H. Green, *XXIX. The anatomy and physiology of the liver.* Philosophical Transactions of the Royal Society of London, 1833. **123**: p. 711-770.
4. Michalopoulos, G.K., *Liver regeneration.* Journal of cellular physiology, 2007. **213**(2): p. 286-300.
5. Vollmar, B. and M.D. Menger, *The Hepatic Microcirculation: Mechanistic Contributions and Therapeutic Targets in Liver Injury and Repair.* Physiological Reviews, 2009. **89**(4): p. 1269-1339.
6. van Grunsven, L.A., *3D in vitro models of liver fibrosis.* Advanced drug delivery reviews, 2017. **121**: p. 133-146.
7. Camps, J., et al., *Chronic Hepatitis and Cirrhosis*, in *Hepatobiliary Diseases*. 1992, Springer. p. 281-415.
8. Deng, J., et al., *Engineered Liver-On-A-Chip Platform to Mimic Liver Functions and Its Biomedical Applications: A Review.* Micromachines, 2019. **10**(10): p. 676.
9. Marra, F. and M. Parola, *Cells in the liver—functions in health and disease*, in *Chronic Liver Failure*. 2011, Springer. p. 3-32.
10. Wisse, E., et al., *The liver sieve: Considerations concerning the structure and function of endothelial fenestrae, the sinusoidal wall and the space of disse.* Hepatology, 1985. **5**(4): p. 683-692.
11. Geraud, C., et al., *Unique cell type-specific junctional complexes in vascular endothelium of human and rat liver sinusoids.* PloS one, 2012. **7**(4): p. e34206.
12. Marrone, G., V.H. Shah, and J. Gracia-Sancho, *Sinusoidal communication in liver fibrosis and regeneration.* Journal of Hepatology, 2016. **65**(3): p. 608-617.
13. Jenne, C.N. and P. Kubes, *Immune surveillance by the liver.* Nature immunology, 2013. **14**(10): p. 996-1006.
14. Senoo, H., *Structure and function of hepatic stellate cells.* Medical Electron Microscopy, 2004. **37**(1): p. 3-15.
15. Böhm, F., et al., *Regulation of liver regeneration by growth factors and cytokines.* EMBO molecular medicine, 2010. **2**(8): p. 294-305.
16. Friedman, S.L., *Hepatic stellate cells: protean, multifunctional, and enigmatic cells of the liver.* Physiological reviews, 2008. **88**(1): p. 125-172.
17. Kawaratani, H., et al., *The Effect of Inflammatory Cytokines in Alcoholic Liver Disease.* Mediators of Inflammation, 2013. **2013**: p. 495156.
18. Tacke, F., T. Luedde, and C. Trautwein, *Inflammatory pathways in liver homeostasis and liver injury.* Clinical reviews in allergy & immunology, 2009. **36**(1): p. 4-12.
19. Nguyen-Lefebvre, A.T. and A. Horuzsko, *Kupffer Cell Metabolism and Function.* Journal of enzymology and metabolism, 2015. **1**(1): p. 101.

20. Li, P., et al., *The role of Kupffer cells in hepatic diseases.* Molecular immunology, 2017. **85**: p. 222-229.
21. Yazdani, S., R. Bansal, and J. Prakash, *Drug targeting to myofibroblasts: Implications for fibrosis and cancer.* Advanced Drug Delivery Reviews, 2017. **121**: p. 101-116.
22. Lee, Y.A., M.C. Wallace, and S.L. Friedman, *Pathobiology of liver fibrosis: a translational success story.* Gut, 2015. **64**(5): p. 830-841.
23. Hinz, B., et al., *Recent developments in myofibroblast biology: paradigms for connective tissue remodeling.* The American journal of pathology, 2012. **180**(4): p. 1340-1355.
24. Lepreux, S. and A. Desmoulière, *Human liver myofibroblasts during development and diseases with a focus on portal (myo)fibroblasts.* Frontiers in physiology, 2015. **6**: p. 173-173.
25. Zeisberg, M. and R. Kalluri, *Cellular mechanisms of tissue fibrosis. 1. Common and organ-specific mechanisms associated with tissue fibrosis.* American Journal of Physiology-Cell Physiology, 2013. **304**(3): p. C216-C225.
26. Mann, D.A. and F. Oakley, *Serotonin paracrine signaling in tissue fibrosis.* Biochimica et Biophysica Acta (BBA)-Molecular Basis of Disease, 2013. **1832**(7): p. 905-910.
27. Sonnylal, S., et al., *Selective expression of connective tissue growth factor in fibroblasts in vivo promotes systemic tissue fibrosis.* Arthritis & Rheumatism, 2010. **62**(5): p. 1523-1532.
28. Wells, R.G., *Tissue mechanics and fibrosis.* Biochimica et biophysica acta, 2013. **1832**(7): p. 884-890.
29. Sacchi, M., R. Bansal, and J. Rouwkema, *Bioengineered 3d models to recapitulate tissue fibrosis.* Trends in biotechnology, 2020. **38**(6): p. 623-636.
30. Wells, R.G., *Tissue mechanics and fibrosis.* Biochimica et Biophysica Acta (BBA)-Molecular Basis of Disease, 2013. **1832**(7): p. 884-890.
31. Sandbo, N., et al., *Control of myofibroblast differentiation by microtubule dynamics through a regulated localization of mDia2.* Journal of Biological Chemistry, 2013. **288**(22): p. 15466-15473.
32. Sakata, R., et al., *Mechanical stretch induces TGF-β synthesis in hepatic stellate cells.* European journal of clinical investigation, 2004. **34**(2): p. 129-136.
33. Wipff, P.-J., et al., *Myofibroblast contraction activates latent TGF-β1 from the extracellular matrix.* The Journal of cell biology, 2007. **179**(6): p. 1311-1323.
34. Meyer-ter-Vehn, T., et al., *Contractility as a prerequisite for TGF-β–induced myofibroblast transdifferentiation in human tenon fibroblasts.* Investigative ophthalmology & visual science, 2006. **47**(11): p. 4895-4904.
35. Chen, C.S., *Mechanotransduction–a field pulling together?* Journal of cell science, 2008. **121**(20): p. 3285-3292.
36. Georges, P.C., et al., *Increased stiffness of the rat liver precedes matrix deposition: implications for fibrosis.* American Journal of Physiology-Gastrointestinal and Liver Physiology, 2007. **293**(6): p. G1147-G1154.
37. Ziol, M., et al., *Relationships between fibrosis amounts assessed by morphometry and liver stiffness measurements in chronic hepatitis or steatohepatitis.* European journal of gastroenterology & hepatology, 2009. **21**(11): p. 1261-1268.
38. Vader, D., et al., *Strain-induced alignment in collagen gels.* PloS one, 2009. **4**(6): p. e5902.

39. Winer, J.P., S. Oake, and P.A. Janmey, *Non-linear elasticity of extracellular matrices enables contractile cells to communicate local position and orientation.* PloS one, 2009. **4**(7): p. e6382.
40. Kim, M.Y., S.K. Baik, and S.S. Lee, *Hemodynamic alterations in cirrhosis and portal hypertension.* The Korean journal of hepatology, 2010. **16**(4): p. 347.
41. Davies, P.F., *Hemodynamic shear stress and the endothelium in cardiovascular pathophysiology.* Nature clinical practice Cardiovascular medicine, 2009. **6**(1): p. 16-26.
42. Elpek, G.Ö., *Angiogenesis and liver fibrosis.* World journal of hepatology, 2015. **7**(3): p. 377.
43. Kniazeva, E. and A.J. Putnam, *Endothelial cell traction and ECM density influence both capillary morphogenesis and maintenance in 3-D.* American Journal of Physiology-Cell Physiology, 2009. **297**(1): p. C179-C187.
44. Sieminski, A., R. Hebbel, and K. Gooch, *The relative magnitudes of endothelial force generation and matrix stiffness modulate capillary morphogenesis in vitro.* Experimental cell research, 2004. **297**(2): p. 574-584.
45. Mammoto, A., et al., *A mechanosensitive transcriptional mechanism that controls angiogenesis.* Nature, 2009. **457**(7233): p. 1103-1108.
46. De Minicis, S., et al., *Gene expression profiles during hepatic stellate cell activation in culture and in vivo.* Gastroenterology, 2007. **132**(5): p. 1937-1946.
47. Seki, E., et al., *TLR4 enhances TGF-β signaling and hepatic fibrosis.* Nature Medicine, 2007. **13**(11): p. 1324-1332.
48. Sawitza, I., et al., *The Niche of Stellate Cells Within Rat Liver.* Hepatology (Baltimore, Md.), 2009. **50**: p. 1617-24.
49. Fennema, E., et al., *Spheroid culture as a tool for creating 3D complex tissues.* Trends in biotechnology, 2013. **31**(2): p. 108-115.
50. Clevers, H., *Modeling Development and Disease with Organoids.* Cell, 2016. **165**(7): p. 1586-1597.
51. Brassard, J.A. and M.P. Lutolf, *Engineering Stem Cell Self-organization to Build Better Organoids.* Cell Stem Cell, 2019. **24**(6): p. 860-876.
52. Drost, J. and H. Clevers, *Organoids in cancer research.* Nature Reviews Cancer, 2018. **18**.
53. Ahadian, S., et al., *Organ-On-A-Chip Platforms: A Convergence of Advanced Materials, Cells, and Microscale Technologies.* Advanced Healthcare Materials, 2017. **7**: p. 1700506.
54. Bhatia, S.N. and D.E. Ingber, *Microfluidic organs-on-chips.* Nature Biotechnology, 2014. **32**(8): p. 760-772.
55. Rouwkema, J. and A. Khademhosseini, *Vascularization and Angiogenesis in Tissue Engineering: Beyond Creating Static Networks.* Trends in Biotechnology, 2016. **34**(9): p. 733-745.
56. Lee, J.B., et al., *Implantable Vascularized Liver Chip for Cross-Validation of Disease Treatment with Animal Model.* Advanced Functional Materials, 2019. **29**(23): p. 1900075.
57. Jang, K.-J., et al., *Liver-Chip: Reproducing Human and Cross-Species Toxicities.* bioRxiv, 2019: p. 631002.

58. Li, X., et al., *A glass-based, continuously zonated and vascularized human liver acinus microphysiological system (vLAMPS) designed for experimental modeling of diseases and ADME/TOX.* Lab on a Chip, 2018. **18**(17): p. 2614-2631.
59. Cho, H.-J., et al., *Bioengineered Multicellular Liver Microtissues for Modeling Advanced Hepatic Fibrosis Driven Through Non-Alcoholic Fatty Liver Disease.* Small, 2021. **17**(14): p. 2007425.
60. Lasli, S., et al., *A Human Liver-on-a-Chip Platform for Modeling Nonalcoholic Fatty Liver Disease.* Advanced Biosystems, 2019. **3**(8): p. 1900104.
61. Suurmond, C.-A.E., et al., *In Vitro Human Liver Model of Nonalcoholic Steatohepatitis by Coculturing Hepatocytes, Endothelial Cells, and Kupffer Cells.* Advanced Healthcare Materials, 2019. **8**(24): p. 1901379.
62. Lee, S.W.L., et al., *Characterizing the Role of Monocytes in T Cell Cancer Immunotherapy Using a 3D Microfluidic Model.* Frontiers in Immunology, 2018. **9**(416).
63. Pavesi, A., et al., *A 3D microfluidic model for preclinical evaluation of TCR-engineered T cells against solid tumors.* JCI insight, 2017. **2**(12).
64. Emulate, I., *Liver-Chip Quad-Culture Protocol.* Emulate, Inc., 2019.
65. Cui, J., et al., *Multicellular Co-Culture in Three-Dimensional Gelatin Methacryloyl Hydrogels for Liver Tissue Engineering.* Molecules, 2019. **24**: p. 1762.
66. Mansi, K. and J. Patel, *Effect of gel porosity and stiffness on culture of HepG2 cells encapsulated in gelatin methacrylate hydrogels.* Bioscience Biotechnology Research Communications, 2016. **9**: p. 463-470.
67. Miri, A.K., et al., *Permeability Mapping of Gelatin Methacryloyl Hydrogels.* Acta Biomaterialia, 2018. **77**.
68. Rouviere, O., et al., *MR elastography of the liver: preliminary results.* Radiology, 2006. **240**(2): p. 440-448.
69. Mueller, S. and L. Sandrin, *Liver stiffness: a novel parameter for the diagnosis of liver disease.* Hepatic medicine: evidence and research, 2010. **2**: p. 49.
70. Rejniak, K., *Systems Biology of Tumor Microenvironment: Quantitative Modeling and Simulations*. Vol. 936. 2016.
71. Shah, A.D., M.J. Bouchard, and A.C. Shieh, *Interstitial Fluid Flow Increases Hepatocellular Carcinoma Cell Invasion through CXCR4/CXCL12 and MEK/ERK Signaling.* PloS one, 2015. **10**(11): p. e0142337-e0142337.
72. Xiao, Y., et al., *Ex vivo Dynamics of Human Glioblastoma Cells in a Microvasculature-on-a-Chip System Correlates with Tumor Heterogeneity and Subtypes.* Advanced Science, 2019. **6**(8): p. 1801531.
73. Nichol, J.W., et al., *Cell-laden microengineered gelatin methacrylate hydrogels.* Biomaterials, 2010. **31**(21): p. 5536-5544.
74. Zhou, M., B.H. Lee, and L.P. Tan, *A dual crosslinking strategy to tailor rheological properties of gelatin methacryloyl.* International Journal of Bioprinting, 2017. **3**.
75. Mironov, V., V. Kasyanov, and R.R. Markwald, *Organ printing: from bioprinter to organ biofabrication line.* Current Opinion in Biotechnology, 2011. **22**(5): p. 667-673.
76. Fröhlich, E., et al., *Comparison of two in vitro systems to assess cellular effects of nanoparticles-containing aerosols.* Toxicology in vitro, 2013. **27**(1): p. 409-417.
77. Miri, A.K., et al., *Permeability mapping of gelatin methacryloyl hydrogels.* Acta biomaterialia, 2018. **77**: p. 38-47.

78. Tan, G., et al., *Biomimetically-mineralized composite coatings on titanium functionalized with gelatin methacrylate hydrogels.* Applied Surface Science, 2013. **279**: p. 293-299.
79. Saito, H., et al., *Efficacy of non-invasive elastometry on staging of hepatic fibrosis.* Hepatology Research, 2004. **29**(2): p. 97-103.
80. Klatt, D., et al., *Viscoelastic properties of liver measured by oscillatory rheometry and multifrequency magnetic resonance elastography.* Biorheology, 2010. **47**(2): p. 133-141.
81. Sandrin, L., et al., *Transient elastography: a new noninvasive method for assessment of hepatic fibrosis.* Ultrasound in medicine & biology, 2003. **29**(12): p. 1705-1713.
82. Grazioli, L., et al., *The pseudocapsule in hepatocellular carcinoma: correlation between dynamic MR imaging and pathology.* European radiology, 1999. **9**(1): p. 62-67.
83. Kim, B., et al., *The capsule appearance of hepatocellular carcinoma in gadoxetic acid-enhanced MR imaging: Correlation with pathology and dynamic CT.* Medicine, 2018. **97**(25): p. e11142-e11142.
84. Jung, J. and J. Oh, *Swelling characterization of photo-cross-linked gelatin methacrylate spherical microgels for bioencapsulation.* e-Polymers, 2014. **14**(3): p. 161-168.
85. Peng, S., et al., *Autocrine vascular endothelial growth factor signaling promotes cell proliferation and modulates sorafenib treatment efficacy in hepatocellular carcinoma.* Hepatology, 2014. **60**(4): p. 1264-1277.
86. Taguchi, T., et al., *Induced albumin secretion from HepG2 spheroids prepared using poly(ethylene glycol) derivative with oleyl groups.* Journal of Materials Science: Materials in Medicine, 2011. **22**(10): p. 2357.
87. Sarkar, S., C.-C. Peng, and Y.-C. Tung, *Comparison of VEGF-A secretion from tumor cells under cellular stresses in conventional monolayer culture and microfluidic three-dimensional spheroid models.* Plos one, 2020. **15**(11): p. e0240833.
88. Roy, M. and S.D. Finley, *Metabolic reprogramming dynamics in tumor spheroids: Insights from a multicellular, multiscale model.* PLoS computational biology, 2019. **15**(6): p. e1007053-e1007053.
89. Kyffin, J.A., et al., *Characterisation of a functional rat hepatocyte spheroid model.* Toxicology in vitro : an international journal published in association with BIBRA, 2019. **55**: p. 160-172.
90. Picout, D. and S. Ross-Murphy, *Rheology of Biopolymer Solutions and Gels.* TheScientificWorldJournal, 2003. **3**: p. 105-21.
91. Fung, Y.-c., *Biomechanics: mechanical properties of living tissues*. 2013: Springer Science & Business Media.
92. Baruffaldi, D., et al., *3D Cell Culture: Recent Development in Materials with Tunable Stiffness.* ACS Applied Bio Materials, 2021. **4**(3): p. 2233-2250.
93. Krishnamoorthy, S., B. Noorani, and C. Xu, *Effects of Encapsulated Cells on the Physical-Mechanical Properties and Microstructure of Gelatin Methacrylate Hydrogels.* International journal of molecular sciences, 2019. **20**(20): p. 5061.
94. Nazempour, A., et al., *Combined effects of oscillating hydrostatic pressure, perfusion and encapsulation in a novel bioreactor for enhancing extracellular matrix synthesis by bovine chondrocytes.* Cell and tissue research, 2017. **370**(1): p. 179-193.

95. Sun, H., et al., *Netrin-1 Regulates Fibrocyte Accumulation in the Decellularized Fibrotic Sclerodermatous Lung Microenvironment and in Bleomycin-Induced Pulmonary Fibrosis.* Arthritis & rheumatology (Hoboken, N.J.), 2016. **68**(5): p. 1251-1261.
96. Booth, A.J., et al., *Acellular normal and fibrotic human lung matrices as a culture system for in vitro investigation.* American journal of respiratory and critical care medicine, 2012. **186**(9): p. 866-876.
97. Bradfield, P., et al., *JAM-C regulates unidirectional monocyte transendothelial migration in inflammation.* Blood, 2007. **110**: p. 2545-55.
98. Čejková, S., I. Králová-Lesná, and R. Poledne, *Monocyte adhesion to the endothelium is an initial stage of atherosclerosis development.* Cor et Vasa, 2016. **58**(4): p. e419-e425.
99. Sosa-Hernández, J.E., et al., *Organs-on-a-Chip Module: A Review from the Development and Applications Perspective.* Micromachines, 2018. **9**(10): p. 536.
100. Rohringer, S., et al., *Mechanisms of vasculogenesis in 3D fibrin matrices mediated by the interaction of adipose-derived stem cells and endothelial cells.* Angiogenesis, 2014. **17**(4): p. 921-933.
101. Han, L., et al., *Mussel-inspired cryogels for promoting wound regeneration through photobiostimulation, modulating inflammatory response and suppressing bacterial invasion.* Nanoscale, 2019. **11**.
102. Lee, J., et al., *Effect of chain flexibility on cell adhesion: Semi-flexible model-based analysis of cell adhesion to hydrogels.* Scientific Reports, 2019. **9**.
103. Xia, T., et al., *The Effect of Matrix Stiffness on Human Hepatocyte Migration and Function—An In Vitro Research.* Polymers, 2020. **12**(9): p. 1903.
104. Semler, E.J., C.S. Ranucci, and P.V. Moghe, *Mechanochemical manipulation of hepatocyte aggregation can selectively induce or repress liver-specific function.* Biotechnology and bioengineering, 2000. **69**(4): p. 359-369.
105. Hintermann, E., et al., *CXCL10 promotes liver fibrosis by prevention of NK cell mediated hepatic stellate cell inactivation.* Journal of autoimmunity, 2010. **35**(4): p. 424-435.
106. Khawar, I.A., et al., *Three Dimensional Mixed-Cell Spheroids Mimic Stroma-Mediated Chemoresistance and Invasive Migration in hepatocellular carcinoma.* Neoplasia, 2018. **20**(8): p. 800-812.
107. De Wever, O., et al., *Critical role of N-cadherin in myofibroblast invasion and migration in vitro stimulated by colon-cancer-cell-derived TGF-β or wounding.* Journal of Cell Science, 2004. **117**(20): p. 4691-4703.
108. Nousi, A., M. Søgaard, and L. Jauffred, *Single-cell tracking reveals super-spreading cells with high persistence in invasive brain cancer*. 2020.
109. Lee, H.-p., R. Stowers, and O. Chaudhuri, *Volume expansion and TRPV4 activation regulate stem cell fate in three-dimensional microenvironments.* Nature Communications, 2019. **10**(1): p. 529.
110. Czochra, P., et al., *Liver fibrosis induced by hepatic overexpression of PDGF-B in transgenic mice.* Journal of hepatology, 2006. **45**(3): p. 419-428.
111. Lepistö, J., et al., *Selective modulation of collagen gene expression by different isoforms of platelet-derived growth factor in experimental wound healing.* Cell and tissue research, 1996. **286**(3): p. 449-455.

112. Karsdal, M.A., et al., *Collagen biology and non-invasive biomarkers of liver fibrosis.* Liver International, 2020. **40**(4): p. 736-750.
113. Geervliet, E., et al., *Matrix metalloproteinase-1 decorated polymersomes, a surface-active extracellular matrix therapeutic, potentiates collagen degradation and attenuates early liver fibrosis.* Journal of Controlled Release, 2021. **332**: p. 594-607.
114. Lachowski, D., et al., *Matrix stiffness modulates the activity of MMP-9 and TIMP-1 in hepatic stellate cells to perpetuate fibrosis.* Scientific Reports, 2019. **9**(1): p. 7299.
115. Dancer, R., A. Wood, and D. Thickett, *Metalloproteinases in idiopathic pulmonary fibrosis.* European Respiratory Journal, 2011. **38**(6): p. 1461-1467.
116. Sun, Y.Y., et al., *Macrophage phenotype in liver injury and repair.* Scandinavian journal of immunology, 2017. **85**(3): p. 166-174.
117. Zimmermann, H.W., et al., *Interleukin-8 is activated in patients with chronic liver diseases and associated with hepatic macrophage accumulation in human liver fibrosis.* PloS one, 2011. **6**(6): p. e21381-e21381.
118. Wang, Y., et al., *Macrophage-derived extracellular vesicles: diverse mediators of pathology and therapeutics in multiple diseases.* Cell Death & Disease, 2020. **11**(10): p. 924.
119. Jeppesen, D.K., et al., *Reassessment of exosome composition.* Cell, 2019. **177**(2): p. 428-445. e18.
120. Fackler, O.T. and R. Grosse, *Cell motility through plasma membrane blebbing.* The Journal of cell biology, 2008. **181**(6): p. 879-884.
121. Wendler, F., G.W. Stamp, and G. Giamas, *Tumor–Stromal Cell Communication: Small Vesicles Signal Big Changes.* Trends in Cancer, 2016. **2**(7): p. 326-329.
122. Morán, L. and F.J. Cubero, *Extracellular vesicles in liver disease and beyond.* World journal of gastroenterology, 2018. **24**(40): p. 4519.
123. Yang, Y.M. and E. Seki, *TNFα in liver fibrosis.* Current pathobiology reports, 2015. **3**(4): p. 253-261.
124. Affò, S. and P. Sancho-Bru, *CCL2: a link between hepatic inflammation, fibrosis and angiogenesis?* Gut, 2014. **63**(12): p. 1834-1835.
125. Wong, S.W., et al., *Soft extracellular matrix enhances inflammatory activation of mesenchymal stromal cells to induce monocyte production and trafficking.* Science advances, 2020. **6**(15): p. eaaw0158.
126. Kang, W., et al., *Tumor invasion as non-equilibrium phase separation*. 2020.
127. Coll, M., et al., *Generation of hepatic stellate cells from human pluripotent stem cells enables in vitro modeling of liver fibrosis.* Cell stem cell, 2018. **23**(1): p. 101-113. e7.
128. Wilkinson, D.C., et al., *Development of a three-dimensional bioengineering technology to generate lung tissue for personalized disease modeling.* Stem cells translational medicine, 2017. **6**(2): p. 622-633.
129. Homan, K.A., et al., *Flow-enhanced vascularization and maturation of kidney organoids in vitro.* Nature Methods, 2019. **16**(3): p. 255-262.
130. Gostynska, N., et al., *3D porous collagen scaffolds reinforced by glycation with ribose for tissue engineering application.* Biomedical Materials, 2017. **12**.

UNIVERSITY OF TWENTE.